

國立臺灣大學理學院物理學系

博士論文

Department of Physics

College of Science

National Taiwan University

Doctoral Dissertation



用於量子計算的堅固量子邏輯閘

Robust Quantum Gates for Quantum Computation

黃嘉賢

Chia-Hsien Huang

指導教授：管希聖 博士

Advisor: Hsi-Sheng Goan, Ph.D.

中華民國 106 年 7 月

July, 2017

國立臺灣大學博士學位論文
口試委員會審定書

用於量子計算的堅固量子邏輯閘
Robust quantum gates for quantum computation

本論文係黃嘉賢君 (d01222002) 在國立臺灣大學物理學系、所
完成之博士學位論文，於民國 106 年 6 月 26 日承下列考試委員審查
通過及口試及格，特此證明

口試委員：

官希聖

(簽名)

(指導教授)

陳岳男

李瑞光

林俊遠

蔡政達

謝辭



首先，我要感謝在成大讀書時教導我的林水田老師、李湘楠老師、和閔振發老師幫我寫推薦信，才讓我有機會可以進入台大讀博士。

接著，我要感謝我的指導教授管希聖老師的提拔，老師給予我很大的自由進行研究工作，並指引我正確的方向，讓我有參與國際合作的機會，還讓我可以國際會議發表演講，並且還幫助我申請工作。同時我也要感謝黃上瑜學長，在我研究起步時提供我相當多的協助，還要感謝陳建彰學長、賴彥佑學長、張晏瑞學長、簡崇欽學長和林冠廷同學，提供我許多技術上、學術上和生活中的建議在我整個博士求學過程中。還要感謝所有在 501 研究室相處過的學長、同學和學弟學妹們(陳柏文、洪常力、戴榮身、楊存毅、周宜、劉伊修、薛逸峰、楊智偉、葉宗剛、李彥賢、梁哲亮、郝鴻、廖允執、許景喻、邱博煌、方之珊、張佑誠、陳則言...)給予我的協助與腦力激盪。我要感謝澳洲的合作夥伴 Henry Yang 博士與 Andrew Dzurak 教授，提供我許多實驗上的觀點，讓我的理論成為可以在實驗上實踐的方法。我要感謝物理系辦公室季力偉先生，還有管希聖老師的秘書劉家綺女士，協助我解決處理許多非學術性的事情。我要感謝林俊達老師、蔡政達老師、李瑞光老師、和陳岳男老師，百忙中撥空來擔任我的論文口試委員。我要感謝台灣大學豐富的圖書與期刊資源，還有 Google 的搜尋引擎，讓我可以很有效率地進行研究工作。我要感謝 QQbit 伺服器不辭辛勞不舍晝夜地努力計算，讓我可以很快地蒐集數據。我要感謝 501 研究室 4 號座位，讓我可以很專心地做研究。我要感謝 X，X 屬於我要感謝但沒有寫出來的所有一切。

最後，我要感謝我最堅強後盾，也就是我的家人，謝謝您們支持我陪伴我完成博士學位。



摘要

要實現量子計算(quantum computation)，我們需要一組高保真(high-fidelity)而且堅固(robust)的量子邏輯閘(quantum gate)，來對抗量子位元(qubit)系統中的噪音(noise)並容許系統參數(system parameter)的不準確性(uncertainty)。堅固控制方法(robust control method)可以提供控制脈波(control pulse)來操控並實現高保真而且堅固的量子邏輯閘。可是大部分的堅固控制方法都假設在量子位元系統中的噪音強度並不隨時間而改變，然而這個假設並不總是對的。因此我們提供一套有系統的堅固控制方法，可以有效地處理隨機(stochastic)並且可隨時間改變(time-varying)的噪音。我們的方法可以同時處理多個不同的噪音來源(multiple sources of noise)，可以運用到不同的量子位元系統與不同的噪音模型，並提供連續性(smooth)的控制脈波來操作高保真而且堅固的量子邏輯閘以實現容錯量子計算(fault-tolerant quantum computation)。

接著，我們將此堅固控制方法運用到一個實際的量子位元系統：半導體量子點電子自旋(quantum-dot electron spin)量子位元。最近，澳洲實驗團隊將此量子位元系統建構在純化的同位素矽(isotopically purified silicon)半導體上來改善來自量子位元環境的噪音，並實現二位元(two-qubit)量子邏輯閘。然而，操控二位元量子邏輯閘會伴隨著電的噪音(electrical noise)，而這個噪音使得二位元量子邏輯閘誤差(gate error)無法達到實現容錯量子計算的門檻(threshold)。我們的堅固控制方法可提供最佳化控制脈波(optimal control pulse)，來操控可以抵抗電的噪音之二位元量子邏輯閘，使得邏輯閘誤差遠低於此門檻，並且堅固於來自於系統參數的不準確性。此外我們的最佳化控制脈波也考慮到實驗上對於控制脈波的限制，像是最強脈波強度(maximum pulse strength)限制，還有由波形產生器(waveform generator)的有限頻寬(finite-bandwidth)所造成的濾波效應(filtering effect)。更進一步，我們在同一個控制架構下提供實驗上可實現的最佳化控制脈波，來操控高保

真而且堅固的二位元量子邏輯閘與單一位元量子邏輯閘(single-qubit quantum gate)，為實現大尺度(large-scale)容錯量子計算提供重要的一步。

關鍵字：量子計算、最佳化控制、堅固、高保真、隨時變噪音、量子邏輯閘、量子點量子位元





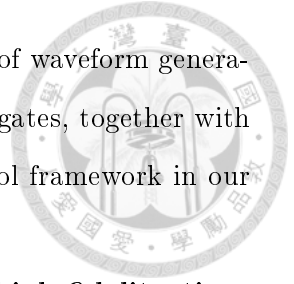
Abstract

To realize practical quantum computation, a set of high-fidelity universal quantum gates robust against noise and uncertainty in the qubit system is prerequisite. Constructing control pulses to operate quantum gates which meet this requirement is an important and timely issue. In most robust control methods, noise is assumed to be quasi-static, i.e., is time-independent within the gate operation time but can vary between different gates. But this quasi-static-noise assumption is not always valid. Here we develop a systematic method to find pulses for quantum gate operations robust against both low- and high-frequency (comparable to the qubit transition frequency) stochastic time-varying noise. Our approach, taking into account the noise properties of quantum computing systems, can output single smooth pulses in the presence of multisources of noise. Furthermore, our method can be applied to different system models and noise models, and will make essential steps toward constructing high-fidelity and robust quantum gates for fault-tolerant quantum computation (FTQC). We also discuss and compare the gate operation performance by our method with that by the filter-transfer-function method.

Then we apply our robust control method for a realistic system of electron spin qubits in semiconductor (silicon) quantum dots, a promising solid-state system compatible with existing manufacturing technologies for practical quantum computation. A two-qubit controlled-NOT (CNOT) gate, realized by a controlled-phase (C-phase) gate together with some single-qubit gates, has been experimentally implemented recently for quantum-dot electron spin qubits in isotopically purified silicon. But the infidelity of the two-qubit C-phase gate is, primarily due to the electrical control noise, still higher than the required error threshold for FTQC. Here we apply our robust control method to construct high-fidelity CNOT gates with single smooth control pulses robust against the electrical noise and the system parameter uncertainty. The experimental constraints on the maximum pulse strength due to the power limitation of the on-chip electron spin resonance (ESR)

line and the filtering effects on the pulses due to the finite bandwidth of waveform generators are also accounted for. The robust and high-fidelity single-qubit gates, together with the two-qubit CNOT gates, can be performed within the same control framework in our scheme, paving the way for large-scale FTQC.

Keywords: quantum computation, optimal control, robust, high-fidelity, time-varying noise, quantum gate, quantum dot qubit





Contents

Acknowledgements	I
Chinese abstract	II
Abstract	IV
1. Introduction	1
2. Robust quantum gates for stochastic time-varying noise	5
2.1. Ensemble average infidelity	5
2.2. Optimization method and noise suppression	8
2.3. Demonstration of our optimal control method	10
2.3.1. Comparison with the quasi-static-noise method	11
2.3.1.1. Single-qubit gates	11
2.3.1.2. Two-qubit gates	16
2.3.2. Comparison with the filter-transfer-function method	19
2.4. Generalization to open quantum system	21
3. Applications to quantum-dot electron spin qubits in isotopically purified silicon	28
3.1. Quantum-dot electron spin qubits	28
3.2. Ideal system	31
3.3. Realistic system	38
3.4. Demonstration of our control scheme	44
3.4.1. CNOT gates	47
3.4.2. Single-qubit gates	52
4. Conclusion	56

A. : Derivation of Eqs. (2.12)-(2.14)

B. : Estimation of higher-order contributions

Bibliography



58

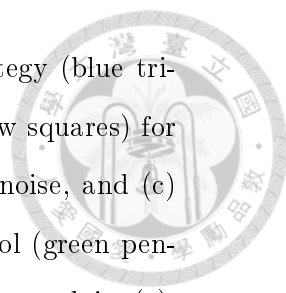
61

62



List of Figures

- 2.1. $J_1 + \langle J_2 \rangle$ versus (a) γ_{ZZ} for Z -noise ($\sigma_{ZZ} = 10^{-3}$, $\sigma_{XX} = 0$) and (b) γ_{XX} for X -noise ($\sigma_{XX} = 10^{-3}$, $\sigma_{ZZ} = 0$). The $J_1 + \langle J_2 \rangle$ values are obtained using the optimal control parameter sets of the Hadamard gate from the IDG strategy (blue triangles), QSN strategy (red circles), and TVN strategy (yellow squares). Ten realizations of OU noise $\beta_{OU}(t)$ with $\sigma_{OU} = 10^{-3}$ for γ_{OU}/ω_0 equal to (c) 10^{-7} , (d) 10^{-3} , and (e) 10^{-1} 12
- 2.2. $J_1 + \langle J_2 \rangle$ values versus γ_{ZZ} for Z -noise ($\sigma_{ZZ} = 10^{-3}$, $\sigma_{XX} = 0$) and versus γ_{XX} for X -noise ($\sigma_{XX} = 10^{-3}$, $\sigma_{ZZ} = 0$) obtained from the IDG strategy (blue triangles), QSN strategy (red circles), and TVN strategy (yellow squares) for the phase gate shown in (a) and (b), respectively, and for the $\pi/8$ gate in (c) and (d), respectively. 12
- 2.3. Robust performance of the Hadamard gate of the IDG strategy (blue triangles), QSN strategy (red circles), and TVN strategy (yellow squares) for low-frequency ($\gamma_{ZZ} = \gamma_{XX} = 10^{-7}\omega_0$) (a) Z -noise, (b) X -noise, and (c) Z -&- X -noise. The corresponding optimal control pulses of the TVN strategy for Z -noise, X -noise, and Z -&- X -noise are shown in (d), (e), and (f), respectively. The number of control parameters $k_{\max}=10$ for $\Omega_X(t)$ in (d)-(f). 14



2.4. Robust performance of the Hadamard gate of the IDG strategy (blue triangles), QSN strategy (red circles), and TVN strategy (yellow squares) for high-frequency ($\gamma_{ZZ} = \gamma_{XX} = 10^{-1}\omega_0$) (a) Z -noise, (b) X -noise, and (c) Z -& X -noise. For TVN strategy with an additional Y control (green pentagrams) in (b), $\gamma_{YY} = \gamma_{XX} = 10^{-1}\omega_0$ and $\sigma_{YY} = \sigma_{XX}$, and in (c), $\gamma_{YY} = \gamma_{ZZ} = \gamma_{XX} = 10^{-1}\omega_0$ and $\sigma_{YY} = \sigma_{XX} = \sigma_{ZZ}$. Optimal control pulses of the TVN strategy (d) for Z -noise and of the TVN strategy with an additional Y control and accompanying Y -noise (e) for X -noise and (f) for Z -& X -noise. The number of control parameters $k_{\max}=10$ for $\Omega_X(t)$ in (d) and $k_{\max}=20$ for both $\Omega_X(t)$ and $\Omega_Y(t)$ in (e) and (f). 15

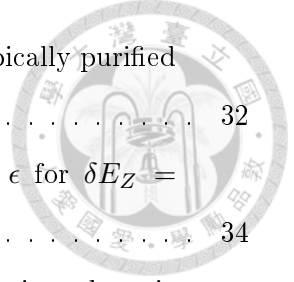
2.5. Robust performance of CNOT gates of the IDG strategy ($\omega_0 t_f = 100$, blue triangles), QSN strategy ($\omega_0 t_f = 100$, red circles), TVN strategy ($\omega_0 t_f = 100$, yellow squares; and $\omega_0 t_f = 20$, purple pentagrams) for high-frequency ($\gamma_{ZZ1} = \gamma_{ZZ2} = \gamma_{XX1} = \gamma_{XX2} = \gamma_{JJ} = 10^{-1}\omega_0$) (a) Z -noise, (b) X -& J -noise, and (c) Z -& X -& J -noise. The optimal control pulses of the TVN strategy ($\omega_0 t_f = 100$) for the Z -noise, X -& J -noise, and Z -& X -& J -noise are shown in (d), (e), and (f), respectively. The numbers of control parameters $k_{\max}=16$, 16, and 8 for $\Omega_{X_1}(t)$, $\Omega_{X_2}(t)$, and $J(t)$, respectively, in (d) and (f); $k_{\max}=12$, 12, and 6 for $\Omega_{X_1}(t)$, $\Omega_{X_2}(t)$, and $J(t)$, respectively, in (e). 18

2.6. The behavior of $[F_z(\omega)/(2\pi\omega^2)]$ obtained using the optimal control parameter sets from the IDG strategy (thick dotted blue line), FTF strategy (thin dash-dotted red line), and TVN strategy (thick solid yellow line) for the noise PSD $S(\omega)$ with (a) $\gamma = 0.1\omega_0$, (b) $\gamma = 0.3\omega_0$, and (c) $\gamma = 0.5\omega_0$ is shown in (d), (e), and (f), respectively. (g) The corresponding $\langle J_2 \rangle$ values. 19

3.1. Loss-and-DiVincenzo's model for quantum dot spin qubit (courtesy of Daniel Loss and David P. DiVincenzo, 1998). 29

3.2. The architecture of single-spin qubit (left panel) and singlet-triplet qubit (right panel) in GaAs semiconductor quantum dots. 30

3.3. Quantum dots in silicon (courtesy of W. H. Lim et al., 2009). 31



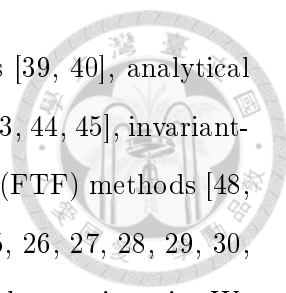
3.4. Architecture of the quantum-dot electron spin qubits in isotopically purified silicon (courtesy of M. Veldhorst et al., 2015).	32
3.5. The effective detuning frequencies $\nu_{\downarrow\downarrow}$ and $\nu_{\downarrow\uparrow}$ versus $U - \epsilon$ for $\delta E_Z = -40\text{MHz}$ and $t_0 = 900\text{MHz}$	34
3.6. Ensemble average probability $\langle P(\uparrow\downarrow\rangle) \rangle$ simulation for stochastic and static electrical noise $\beta_{U-\epsilon}$ with mean value $\mu_{U-\epsilon} = 0$ and with standard deviation $\sigma_{U-\epsilon} = 0, 3, 10\text{GHz}$	40
3.7. The experimentally measured $\langle P(\uparrow\downarrow\rangle) \rangle$ (courtesy of Veldhorst et al., 2015).	40
3.8. J_{2,t_0} versus $\langle J_{2,U-\epsilon} \rangle$ with $\sigma_{U-\epsilon} = 3\text{GHz}$ for $\alpha_{t_0} = 9\text{MHz}$ and 4.5MHz	41
3.9. $\Omega_X(\omega)$ and $\Omega_Y(\omega)$ of the optimal CNOT gate with $t_f = 500\text{ns}$	44
3.10. The filtered pulse $\Omega_X^{\text{filt}}(t)$ and $\Omega_Y^{\text{filt}}(t)$ of the optimal CNOT gate by the transfer function with the response function of the filter $F(\omega) = \exp(-\omega^2/\omega_0^2)$	45
3.11. J_1 and $\langle J_{2,U-\epsilon} \rangle$ degradation from the filtering effects.	45
3.12. The optimized J_1 values versus optimization iterations after the J_1 optimization for the CNOT gate.	49
3.13. The distribution of the maximum pulse strength Ω_X^{Max} and Ω_Y^{Max} after the J_1 optimization for the CNOT gate.	49
3.14. The $\langle J_{2,U-\epsilon} \rangle$ topography of the CNOT gate with $\sigma_{U-\epsilon} = 3\text{GHz}$ versus maximum pulse strength Ω_X^{Max} and Ω_Y^{Max} for the J_1 optimized ensemble (1100 samples).	50
3.15. $\langle \mathcal{I} \rangle$ of the CNOT gate versus α_{t_0} after the two-step optimization and after the fine-tuning optimization.	51
3.16. Pulse shift after the fine-tuning optimization for the CNOT gate.	51
3.17. Robust performance against uncertainty α_{t_0} in t_0 for the optimal CNOT gates of $\Omega_{<1\text{mT}}$ (red diamond-line) and $\Omega_{<1.5\text{mT}}$ (yellow square-line), and the C-phase gate (blue circle-line).	52
3.18. The optimal control pulses of the CNOT gate with $\Omega_{<1\text{mT}}$ and $\Omega_{<1.5\text{mT}}$	53
3.19. $\langle J_{2,U-\epsilon} \rangle$ topography of $I_2 \otimes X_1$ gate with $\sigma_{U-\epsilon} = 3\text{GHz}$ versus maximum pulse strength Ω_X^{Max} and Ω_Y^{Max} for the J_1 optimized ensemble (2389 samples).	54
3.20. Robust performance against uncertainty α_{t_0} in t_0 for the optimal single-qubit $I_2 \otimes X_1$ gate and $H_2 \otimes I_1$ gate.	55
3.21. The optimal control pulses of the single-qubit $I_2 \otimes X_1$ gate and $H_2 \otimes I_1$ gate.	55



1. Introduction

A bit is the fundamental storage and computing unit in classical computers. This fundamental unit in quantum computers is called a quantum bit (qubit), which is defined through a realistic two-level system. The two-level states, $|0\rangle$ and $|1\rangle$, of a qubit correspond to 0 and 1 of a classical bit, respectively. However, a qubit can according to quantum mechanics be in the superposition state of $|0\rangle$ and $|1\rangle$, $\alpha|0\rangle + \beta|1\rangle$, and a classical bit can only be 0 or 1. Combining with other properties of quantum mechanics such as entanglement, quantum computers via quantum algorithms can tackle certain problems, which can not be solved by the existing classical supercomputers. These quantum algorithms such as Shor's algorithm and Grover's algorithm command the quantum computers to execute a specific task via a composition of quantum gates. A quantum gate is operated on the qubits by our controls in the system, and is just the propagator for the qubit system. The dynamics of a quantum gate is governed by the Schrödinger equation. However, there exist noise and uncertainty in a realistic system, causing the gate error or infidelity for each gate. In this case, a quantum algorithm, composed of many quantum gates, may easily fail. Fortunately, fault-tolerant quantum computation (FTQC) via a set of universal quantum gates, in terms of which any unitary operation can be expressed to arbitrary accuracy, can correct these errors if gate error of each universal quantum gate is below some threshold, for example, 10^{-2} for surface codes [1]. Therefore, our goal is to make all universal quantum gates robust against the strength of noise and uncertainty to meet the FTQC threshold requirement and to realize practical quantum computation.

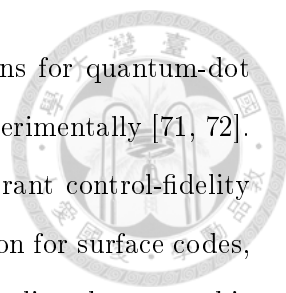
Quantum gates in open quantum systems have been investigated by various methods such as dynamical decoupling methods [2, 3, 4, 5, 6, 7, 8, 9, 10, 11] and optimal control methods [12, 13, 14, 15, 16, 17, 18, 19]. For classical noise, there are many robust control methods such as composite pulses [20, 21, 22, 23, 24, 25, 26, 27, 28, 29], soft uniaxial positive control for orthogonal drift error (SUPCODE) [30, 31, 32, 33, 34, 35], sampling-based



learning control method [36, 37, 38], inhomogeneous control methods [39, 40], analytical method [41], single-shot pulse method [42], optimal control methods [43, 44, 45], invariant-based inverse engineering method [46, 47], and filter-transfer-function (FTF) methods [48, 49, 50, 51]. However, in most of these methods [20, 21, 22, 23, 24, 25, 26, 27, 28, 29, 30, 31, 32, 33, 34, 35, 36, 37, 38, 39, 40, 41, 42, 43, 44], noise is assumed to be quasi-static. We call these robust control strategies the quasi-static-noise (QSN) methods. But this QSN assumption is not always valid [52]. The robust performance of control pulses obtained by the QSN methods under time-dependent noise (e.g., $1/f^\alpha$ noise) [32, 33, 35, 53] have been investigated, and it was found that they can still work well for relatively low-frequency non-Markovian noise (e.g., $1/f^\alpha$ noise with $\alpha \gtrsim 1$).

Stochastic time-dependent noise is treated in the FTF method [48, 49, 50] in which the area of the filter-transfer function in the frequency region, where the noise power spectral density (PSD) is non-negligible, is minimized. However, in this approach only the filter-transfer function overlapping with the noise PSD in the preset frequency region is considered, but the detailed information of the distribution of the noise PSD is not included in the optimization cost function. Here we develop an optimal control method in time domain by choosing the ensemble average gate infidelity (error) as our cost function for optimization. As a result, the noise correlation function (CF) or equivalently the detailed noise PSD distribution appears naturally in our chosen optimization cost function. Therefore our method can have better robust performance against noise in a general case. The idea of our method is simple, and our method is not limited to particular system models, noise models, and noise CFs. We demonstrate our robust control method for classical noise, but our method can be easily generalized to the case of quantum noise by replacing the ensemble average for classical noise with the trace over the degrees of freedom of the quantum noise (environment) [51]. In other words, our method can be applied to systems with both classical noise and quantum noise present simultaneously.

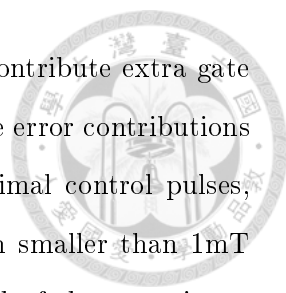
Electron spin qubits in semiconductor quantum dots [54] are promising solid-state systems to realize quantum computation. Significant progresses of quantum-dot spin qubits for quantum information processing have been made with III-V semiconductors such as GaAs [55, 56, 57, 58, 59, 60, 61, 62, 63, 64, 65, 66, 67], but the coherence time of the qubits is limited by the strong dephasing from the environment nuclear spins [68]. On the other hand, the coherence time is substantially improved by using the Si-based host substrate



[69, 70, 71, 72, 73, 74]. Recently, important quantum gate operations for quantum-dot spin qubits in isotopically purified silicon have been demonstrated experimentally [71, 72]. There, the single-qubit gates have been demonstrated with fault-tolerant control-fidelity [71], but the two-qubit gate fidelity [72] has not yet reached the criterion for surface codes, primarily due to the noise of the electrical voltage control used to realize the two-qubit gate.

Our goal is to construct robust quantum gates for quantum-dot spin qubits in purified silicon with fidelity enabling large-scale FTQC by our robust control method. In the experiment of this system [72], a single-qubit gate is realized by tuning down the detuning energy to a small constant value to decouple the two-qubit coupling, and the qubit working in this detuning energy region is not sensitive to the electrical noise. Inversely, a two-qubit gate is realized by tuning up the detuning energy to a large constant value to increase the coupling between two qubits, and the qubit working in this detuning energy region is very sensitive to the electrical noise. Therefore, for two-qubit gates, the electrical noise is the dominant source for fidelity degradation. Besides, when operating a sequence of single-qubit gates and two-qubit gates, the rise and fall times of the detuning energy between two-qubit gate and single-qubit gates would cause gate errors. And changing detuning energy accompanies stark shifts on the quantum-dot qubits, which may result in additional gate errors if the calibration is not precise. Therefore, we propose to keep the detuning energy as a constant value when operating a sequence of single-qubit and two-qubit gates to prevent the fidelity degradation from tuning the detuning energy up and down. After finishing a sequence of gate operations, the detuning energy can be pulled to a small value for the idle time.

Therefore, we keep the detuning energy as a constant value, and only control two AC magnetic fields to operate single-qubit gates and two-qubit gates against the electrical noise with realistic system parameters from the experiment [72]. In addition to the electrical noise, we also consider other factors degrading the gate fidelity in our realistic model for simulation such as the uncertainty in the system parameter and the filtering effects due to the finite bandwidth of waveform generators. In experiment, the interdot tunnel coupling is obtained by fitting the experimental data, and thus there may exist some uncertainty in the interdot tunnel coupling, and the uncertainty will degrade the gate fidelity. When we apply our optimal control pulses in an experiment, their shape will be



altered due to the filtering effects, and the pulse distortion will also contribute extra gate errors. Then we apply our robust control method to minimize the gate error contributions from the noise, the uncertainty, and the filtering effects by our optimal control pulses, which satisfy the constraint of the maximum magnetic field strength smaller than 1mT due to the power limitation through the on-chip ESR line. Instead of decomposing a controlled-NOT (CNOT) gate into a C-phase gate and several single-qubit gates in series as in the experiment [72], we can construct single smooth pulses for CNOT gates directly to reduce the gate operation time and the accumulated gate errors from the decomposed gates. Finally, we demonstrate that our optimal CNOT gate with maximum magnetic field strength smaller than 1mT can suppress the infidelity contribution from the electrical noise to $\sim 10^{-5}$ (around two orders of magnitude improvement compared with the simulation of the realized ideal C-phase gate in experiment) and can be robust against the uncertainty $\sim 10\%$ of the interdot tunnel coupling for the threshold of surface codes (10^{-2}). For our optimal single-qubit gates with maximum magnetic field strength smaller than 1mT, the infidelity contribution from the electrical noise is also suppressed to $\sim 10^{-5}$ and the robustness against the uncertainty error of the interdot tunnel coupling is over 15% for the threshold of surface codes. The gate operation time of our optimal single-qubit gates is also improved to $200 \sim 250\text{ns}$ from $1.5\mu\text{s}$ (π pulse in the experiment [72]). The gate infidelities mentioned above have been recovered from the fidelity degradation due to the filtering effects for both single-qubit gates and CNOT gates. To conclude, our robust control strategy can provide high-fidelity and robust single-qubit gates and CNOT gates for quantum-dot spin qubits in isotopically purified silicon, paving an essential step toward large-scale FTQC.

The thesis is organized as follows. In Chapter 2, we introduce our robust control method and demonstrate its performance. In Chapter 3, we apply our robust control method introduced in Chapter 2 to construct high-fidelity and robust single-qubit gates and CNOT gates for quantum-dot spin qubits in isotopically purified silicon. In Chapter 4, we conclude what we did and show the future development directions for robust quantum gates.



2. Robust quantum gates for stochastic time-varying noise

In this chapter, we first introduce the concept of ensemble average infidelity and our robust control method. We then demonstrate the performance of our method through comparing with the quasi-static-noise (QSN) method and the filter-transfer-function (FTF) method, and finally generalize our method to open quantum system.

2.1. Ensemble average infidelity

We describe the dynamics of the n -qubit system by its propagator

$$U(t) = \mathcal{T}_+ \exp[-i \int_0^t \mathcal{H}(t') dt'], \quad (2.1)$$

where $\mathcal{H}(t)$ is the Hamiltonian of the system (in this chapter we set $\hbar = 1$), and \mathcal{T}_+ is the time-ordering operator. We can control $\mathcal{H}(t)$ from $t = 0$ to $t = t_f$ to obtain $U(t_f)$ by Eq. (2.1), and $U(t_f)$ is just a quantum gate for the n -qubit system with operation time t_f . Assume that U_T is our target gate, we can define the gate error (gate infidelity) as

$$\mathcal{I} \equiv 1 - \frac{1}{4^n} \left| \text{Tr} \left[U_T^\dagger U(t_f) \right] \right|^2, \quad (2.2)$$

where Tr denotes a trace over the n -qubit system state space. In a realistic system, there may exist noise, and thus the Hamiltonian of the system $\mathcal{H}(t)$ should include two parts

$$\mathcal{H}(t) = \mathcal{H}_I(t) + \mathcal{H}_N(t), \quad (2.3)$$

where $\mathcal{H}_I(t)$ is the ideal system Hamiltonian and $\mathcal{H}_N(t)$ is the noise Hamiltonian. If there is no noise in the system ($\mathcal{H}_N(t) = 0$), the Hamiltonian $\mathcal{H}(t)$ will recover to the ideal

system Hamiltonian $\mathcal{H}_I(t)$, and then the system propagator $U(t) = U_I(t)$, where

$$U_I(t) = \mathcal{T}_+ \exp[-i \int_0^t \mathcal{H}_I(t') dt'] \quad (2.4)$$

is the ideal system propagator. For there may exist many sources of noise, the general form of the noise Hamiltonian is

$$\mathcal{H}_N(t) = \sum_j \beta_j(t) H_{N_j}(t), \quad (2.5)$$

where $\beta_j(t)$ is the strength of the j -th noise and $H_{N_j}(t)$ is the corresponding system coupling operator term. In general, $\beta_j(t)$ is time-varying and stochastic, but if $\beta_j(t)$ is a constant and non-stochastic, β_j can be regarded as a systematic error or uncertainty.

To see the noise contribution in the gate infidelity \mathcal{I} , we transform the system to the interaction picture by $U_I(t)$, and then the system Hamiltonian in the interaction picture is

$$\tilde{\mathcal{H}}_N(t) = \sum_j \beta_j(t) R_j(t), \quad (2.6)$$

where

$$R_j(t) \equiv U_I^\dagger(t) H_{N_j}(t) U_I(t). \quad (2.7)$$

Then the system propagator in the interaction picture is

$$\tilde{U}(t_f) = \mathcal{T}_+ \exp[-i \int_0^{t_f} \tilde{\mathcal{H}}_N(t') dt'] \quad (2.8)$$

If noise strength is not too strong, we can expand $\tilde{U}(t_f)$ by Dyson series [75] as the form $\tilde{U}(t_f) = I + \Psi_1 + \Psi_2 + \dots$, where the first two terms of Ψ_j are

$$\Psi_1 = -i \int_0^{t_f} \tilde{\mathcal{H}}_N(t') dt', \quad (2.9)$$

$$\Psi_2 = - \int_0^{t_f} dt_1 \int_0^{t_1} dt_2 \tilde{\mathcal{H}}_N(t_1) \tilde{\mathcal{H}}_N(t_2). \quad (2.10)$$

Now we transform the propagator in the interaction picture $\tilde{U}(t_f)$ back to the original frame to obtain

$$U(t_f) = U_I(t_f) \cdot [I + \Psi_1 + \Psi_2 + \dots], \quad (2.11)$$

and substitute it into the gate infidelity definition in Eq. (2.2). The expanded infidelity \mathcal{I} (see Appendix A) takes the form

$$\mathcal{I} = J_1 + J_2 + \epsilon + \mathcal{O}(\tilde{\mathcal{H}}_N^m, m \geq 3), \quad (2.12)$$

$$J_1 \equiv 1 - \frac{1}{4^n} \left| \text{Tr} \left[U_T^\dagger U_I(t_f) \right] \right|^2, \quad (2.13)$$

$$J_2 \equiv -\frac{1}{2^{n-1}} \text{Re} [\text{Tr} (\Psi_2)] - \frac{1}{4^n} |\text{Tr} (\Psi_1)|^2. \quad (2.14)$$

Here J_1 is the definition of gate infidelity for the ideal system $\mathcal{H}_I(t)$, J_2 is the lowest-order contribution of the noise to the gate infidelity, ϵ (detailed form shown in Appendix A) denotes an extra contribution that is correlated to J_1 and the Dyson expansion terms Ψ_j , and $\mathcal{O}(\tilde{\mathcal{H}}_N^m, m \geq 3)$ represents other higher-order terms excluding ϵ . If noise strength is not too strong such that $|\Psi_{j+1}| \ll |\Psi_j|$, the extra contribution ϵ will become negligible when J_1 is getting small (see discussion in Appendix A). The symbol Re in Eq. (2.14) denotes taking the real part of the quantity it acts on. Because noise $\beta_j(t)$ is stochastic in general, we denote the ensemble average of the infidelity over the different noise realizations as

$$\langle \mathcal{I} \rangle = J_1 + \langle J_2 \rangle + \langle \epsilon \rangle + \left\langle \mathcal{O}(\tilde{\mathcal{H}}_N^m, m \geq 3) \right\rangle. \quad (2.15)$$

Here

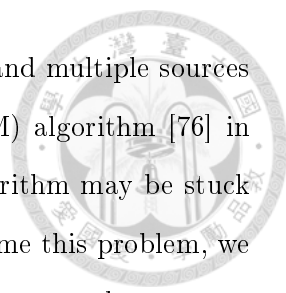
$$\begin{aligned} \langle J_2 \rangle &= \sum_{j,k} \int_0^{t_f} dt_1 \int_0^{t_1} dt_2 C_{jk}(t_1, t_2) \frac{\text{Tr} [R_j(t_1) R_k(t_2)]}{2^{n-1}} \\ &\quad - \sum_{j,k} \int_0^{t_f} dt_1 \int_0^{t_f} dt_2 C_{jk}(t_1, t_2) \frac{\text{Tr} [R_j(t_1)] \text{Tr} [R_k(t_2)]}{4^n}, \end{aligned} \quad (2.16)$$

where $C_{jk}(t_1, t_2) = \langle \beta_j(t_1) \beta_k(t_2) \rangle$ is the CF for noise $\beta_j(t_1)$ and $\beta_k(t_2)$. The first-order noise term proportional to $\text{Re}[\text{Tr}(\Psi_1)]$ vanishes due to the fact that $\text{Tr}(\Psi_1)$ is purely imaginary rather than the assumption of $\langle \beta_j(t) \rangle = 0$ (see Appendix A). If different sources of noise are independent, $C_{jk}(t_1, t_2) = 0$ for $j \neq k$, and if noise Hamiltonian $\mathcal{H}_N(t)$ is traceless, the second term in Eq. (2.16) vanishes. If β_j is a systematic error or uncertainty, $C_{jj}(t_1, t_2) = \beta_j^2$.

2.2. Optimization method and noise suppression

The ideal Hamiltonian $\mathcal{H}_I(t)$ is a function of the control field $\Omega(t)$, that is $\mathcal{H}_I(t) = \mathcal{H}_I(\Omega(t))$, and the control field $\Omega(t)$ is chosen to be a function of a set of control parameters $[a_1, a_2, \dots]$. Then $U_I(t)$ and each term of the ensemble average infidelity $\langle \mathcal{I} \rangle$ in Eq. (2.15) are also a function of the control parameter set $[a_1, a_2, \dots]$. Our goal is to search the optimal parameter set $[a_1, a_2, \dots]$ that minimizes the ensemble average infidelity $\langle \mathcal{I} \rangle$. If the noise strength or fluctuation is not large, then the dominant noise contribution to $\langle \mathcal{I} \rangle$ is from $\langle J_2 \rangle$ as the higher order terms $\langle \mathcal{O}(\tilde{\mathcal{H}}_N^m, m \geq 3) \rangle$ can be neglected (see Appendix B). J_1 can generally be made sufficiently small so that the extra term $\langle \epsilon \rangle$ in $\langle \mathcal{I} \rangle$ of Eq. (2.15) can be safely ignored. So we concentrate on the minimization of $\langle \mathcal{I} \rangle \cong J_1 + \langle J_2 \rangle$ for obtaining the optimal control parameter set.

We use the two-step optimization to achieve this goal. The first step is called the J_1 optimization in which J_1 is the cost function. The gate infidelities J_1 in an ideal unitary system with gate-operation-controllability and a sufficient number of control parameters can be made as low as one wishes, limited only by the machine precision of the computation. So using an ensemble of random control parameter sets as initial guesses, we obtain after the J_1 optimization an ensemble of optimized control parameters sets all with very low values of J_1 . The second step is called the $J_1 + \langle J_2 \rangle$ optimization. We take $J_1 + \langle J_2 \rangle$ as a cost function and randomly choose some optimized control parameter sets in the first optimization step as initial guesses to run the optimal control algorithm. After the $J_1 + \langle J_2 \rangle$ optimization, we obtain an ensemble of control parameter sets with low values of $J_1 + \langle J_2 \rangle$, and then choose the lowest one as the optimal control parameter set. The purpose of using the two-step optimization is to improve optimization efficiency. If we run the $J_1 + \langle J_2 \rangle$ optimization directly from an ensemble of random control parameter sets, we need more optimization iterations to achieve the goal, and the success rate is relatively low compared with the two-step optimization. Besides, the $J_1 + \langle J_2 \rangle$ optimization enables us to know separately the optimized values of J_1 and $\langle J_2 \rangle$. When $\langle J_2 \rangle$ can be minimized to a very small value as in the case of static or low-frequency noise, one has to use a small time step for simulation to make J_1 smaller than $\langle J_2 \rangle$. However, for high-frequency noise, $\langle J_2 \rangle$ is hard to be minimized to a very small value, and one can instead choose a suitable larger time step to make J_1 just one or two orders of magnitude smaller than $\langle J_2 \rangle$,



saving substantially the optimization time especially for multiqubits and multiple sources of noise. We use the gradient-free and model-free Nelder-Mead (NM) algorithm [76] in both the J_1 and $J_1 + \langle J_2 \rangle$ optimization steps. However, the NM algorithm may be stuck in local traps in the $J_1 + \langle J_2 \rangle$ parameter space topography. To overcome this problem, we use the repeating-NM algorithm in the $J_1 + \langle J_2 \rangle$ optimization step. The control parameter set from the first $J_1 + \langle J_2 \rangle$ optimization may lie in a local trap. Therefore, we add random fluctuations to this control parameter set and try to pull it out of the trap. Then we use this shifted control parameter set as an initial guess to run the second $J_1 + \langle J_2 \rangle$ optimization. We repeat the same procedure many times until the values of $J_1 + \langle J_2 \rangle$ can not be improved (reduced) anymore, and then output the corresponding control parameter set. Our optimization method employing the gradient-free and model-free NM algorithm is quite general, capable of dealing with different forms or structures of the ideal system Hamiltonian $\mathcal{H}_I(t)$, control field $\Omega(t)$, noise Hamiltonian $\mathcal{H}_N(t)$, and noise CF $C_{jk}(t_1, t_2)$ for a few qubit systems.

The robustness of our method can be understood as follows. After the two-step optimization, one can obtain small $J_1 + \langle J_2 \rangle$. Generally, J_1 can be even a few orders of magnitude smaller than $\langle J_2 \rangle$, and then $\langle \mathcal{I} \rangle \cong \langle J_2 \rangle$. For simplicity, let us assume that there is only one source of traceless noise present in the system with correlation function given by $C(t_1, t_2) = \bar{\sigma}^2 \tilde{C}(t_1, t_2)$, where $\bar{\sigma}$ is the standard deviation of the noise strength fluctuation. Then from Eq. (2.16), we have $\langle \mathcal{I} \rangle \cong \langle J_2 \rangle = \bar{\sigma}^2 \{ \int_0^{t_f} dt_1 \int_0^{t_1} dt_2 \tilde{C}(t_1, t_2) \text{Tr}[R(t_1)R(t_2)] / 2^{n-1} \}$. If the value of $\{ \int_0^{t_f} dt_1 \int_0^{t_1} dt_2 \tilde{C}(t_1, t_2) \text{Tr}[R(t_1)R(t_2)] / 2^{n-1} \}$ can be reduced more, then larger noise $\bar{\sigma}^2$ can be tolerated under the same error (infidelity) threshold, that is, the quantum gate can be more robust to noise fluctuation. The infidelity $\langle \mathcal{I} \rangle$ to the lowest noise order is proportional to $\bar{\sigma}^2$; but if $\bar{\sigma}$ is too large, then the higher order terms $\langle \mathcal{O}(\tilde{\mathcal{H}}_N^m, m \geq 3) \rangle$ should be considered. Therefore, robust performance can be demonstrated by showing the relation of full-order $\langle \mathcal{I} \rangle$ versus $\bar{\sigma}$. The full-order $\langle \mathcal{I} \rangle$ we use to show the robust performance is calculated using the full evolution of the total system-noise Hamiltonian without any approximation. By inputting the optimal control parameter set obtained by the optimization strategy into the total system-noise Hamiltonian $\mathcal{H}(t) = \mathcal{H}_I(t) + \mathcal{H}_N(t)$ to obtain numerically the full propagator for a single noise realization, we can calculate the gate infidelity \mathcal{I} using Eq. (2.2) for the noise realization. The procedure is repeated for many different noise realizations. Then we take an ensemble average of the infidelities over the

different noise realizations to obtain $\langle \mathcal{I} \rangle$.



2.3. Demonstration of our optimal control method

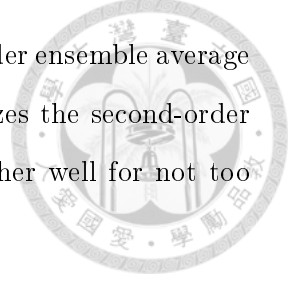
In principle, we could deal with any given form of the noise correlation function (or equivalently the noise PSD) to insert into Eq. (2.16) for the $J_1 + \langle J_2 \rangle$ optimization. But as a particular example, we choose the Ornstein-Uhlenbeck (OU) process $\beta_{OU}(t)$ to simulate stochastic time-varying noise [77]. Studying the influence of and developing robust strategies against time-dependent noise is an important subject of research in quantum control problems both theoretically and experimentally [48, 49, 50, 52, 53]. If the initial noise $\beta_{OU}(t = 0)$ is a normal distribution with zero mean and with standard deviation σ_{OU} , then the noise CF of the OU process $\beta_{OU}(t)$ is

$$C_{OU}(t_1, t_2) = \sigma_{OU}^2 \exp(-\gamma_{OU} |t_1 - t_2|) \quad (2.17)$$

with the noise correlation time $\tau \sim (1/\gamma_{OU})$, and the corresponding noise PSD is Lorentzian

$$S_{OU}(\omega) = \frac{2\sigma_{OU}^2\gamma_{OU}}{(\gamma_{OU}^2 + \omega^2)}. \quad (2.18)$$

Lorentzian PSDs of spin noise resulting in a fluctuating magnetic field at the location of the qubits in InGaAs semiconductor quantum dots have been measured experimentally [78, 79]. Generally, a small γ_{OU} corresponds to low-frequency or quasi-static noise; a large γ_{OU} corresponds to high-frequency noise. The noise $\beta_{OU}(t)$ can be simulated through the formula $\beta_{OU}(t + dt) = (1 - \gamma_{OU}dt)\beta_{OU}(t) + \sigma_{OU}\sqrt{2\gamma_{OU}}dW(t)$, where $W(t)$ is a Wiener process [77]. Figures 2.1(c), (d), and (e) show the different realizations of the noise $\beta_{OU}(t)$ with $\sigma_{OU} = 10^{-3}$ for different values of $\gamma_{OU}/\omega_0 = 10^{-7}$, 10^{-3} , and 10^{-1} , respectively, where ω_0 is the typical system frequency. We note here that the particular choice of the OU noise should by no means diminish the value of our work or the power of our method. Any given or experimentally measured well-behaved noise PSD or noise CF can be dealt with. We will demonstrate later that our method can also work effectively for another form of noise PSD different from that of the OU noise when we compare the performance of our method with that of the FTF method. The reason for using the OU noise in the system-noise Hamiltonian here is that it is relatively easy to simulate its stochastic noise



realizations in the time domain. Therefore, we can calculate the full-order ensemble average infidelity $\langle \mathcal{I} \rangle$ to show that our $J_1 + \langle J_2 \rangle$ optimization, which minimizes the second-order noise contribution to the average infidelity $\langle \mathcal{I} \rangle$, can indeed work rather well for not too strong a noise fluctuation.

2.3.1. Comparison with the quasi-static-noise method

2.3.1.1. Single-qubit gates

We demonstrate as an example the implementation of single-qubit gates in the presence of time-varying noise using our method. The ideal system Hamiltonian for the qubit is

$$\mathcal{H}_I(t) = \omega_0 \frac{Z}{2} + \Omega_X(t) \frac{X}{2}, \quad (2.19)$$

where X and Z stand for the Pauli matrices, ω_0 is the qubit transition frequency, and $\Omega_X(t)$ is the control field in the X term. The noise Hamiltonian is written as

$$\mathcal{H}_N(t) = \beta_Z(t) \omega_0 \frac{Z}{2} + \beta_X(t) \Omega_X(t) \frac{X}{2}. \quad (2.20)$$

We call $\beta_Z(t)$ the Z -noise and $\beta_X(t)$ the X -noise, and assume that they are independent OU noises with CFs $C_{ZZ}(t_1, t_2) = \sigma_{ZZ}^2 \exp(-\gamma_{ZZ} |t_1 - t_2|)$ and $C_{XX}(t_1, t_2) = \sigma_{XX}^2 \exp(-\gamma_{XX} |t_1 - t_2|)$ as the form of Eq. (2.17). We choose the control pulse as a composite sine pulse expressed as

$$\Omega_X(t) = \sum_{k=1}^{k_{\max}} a_k \sin\left(m_k \pi \frac{t}{t_f}\right), \quad (2.21)$$

where the set of the strengths of the single sine pulses is the control parameter set $[a_k] = [a_1, a_2, \dots, a_{k_{\max}}]$ and $\{m_k\}$ is a set of integers, chosen depending on the nature of the system Hamiltonians and the target gates as well as the properties of the noise models.

We define below three optimization strategies, namely, the ideal-gate (IDG) strategy, quasi-static-noise (QSN) strategy, and time-varying-noise (TVN) strategy. The IDG strategy is to perform the first-step optimization (J_1 optimization) only and to show the performance of an ideal gate pulse in the presence of noise. The TVN strategy is our proposed method described earlier above, in which the actual γ_{ZZ} and γ_{XX} values are used in the noise CFs of the cost function $\langle J_2 \rangle$ for the second-step optimization. The QSN strategy uses the same optimization procedure as the TVN strategy, but with $\gamma_{ZZ} = \gamma_{XX} = 0$ for

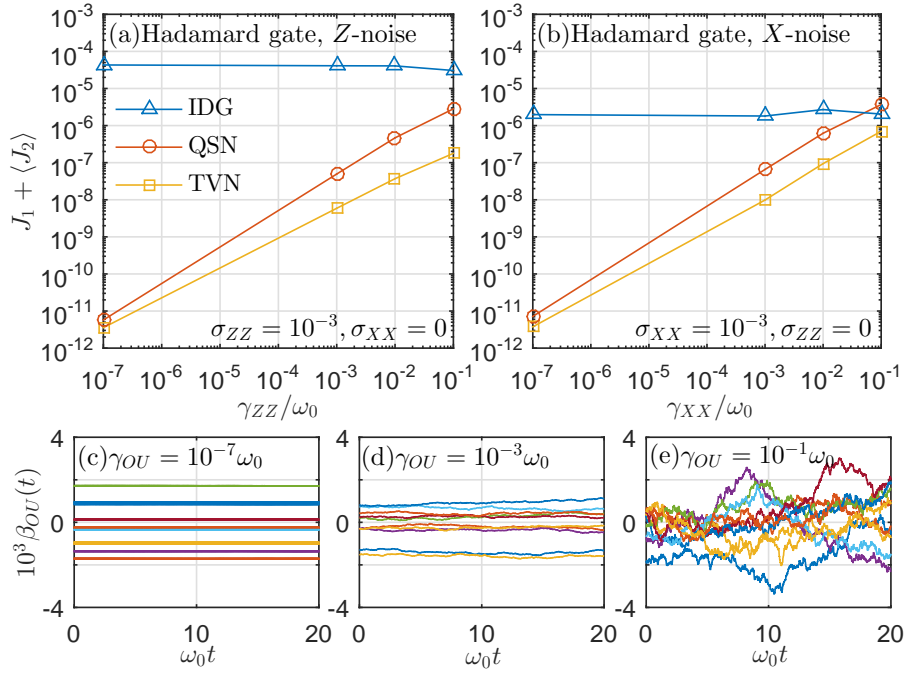


Figure 2.1.: $J_1 + \langle J_2 \rangle$ versus (a) γ_{ZZ} for Z -noise ($\sigma_{ZZ} = 10^{-3}$, $\sigma_{XX} = 0$) and (b) γ_{XX} for X -noise ($\sigma_{XX} = 10^{-3}$, $\sigma_{ZZ} = 0$). The $J_1 + \langle J_2 \rangle$ values are obtained using the optimal control parameter sets of the Hadamard gate from the IDG strategy (blue triangles), QSN strategy (red circles), and TVN strategy (yellow squares). Ten realizations of OU noise $\beta_{OU}(t)$ with $\sigma_{OU} = 10^{-3}$ for γ_{OU}/ω_0 equal to (c) 10^{-7} , (d) 10^{-3} , and (e) 10^{-1} .

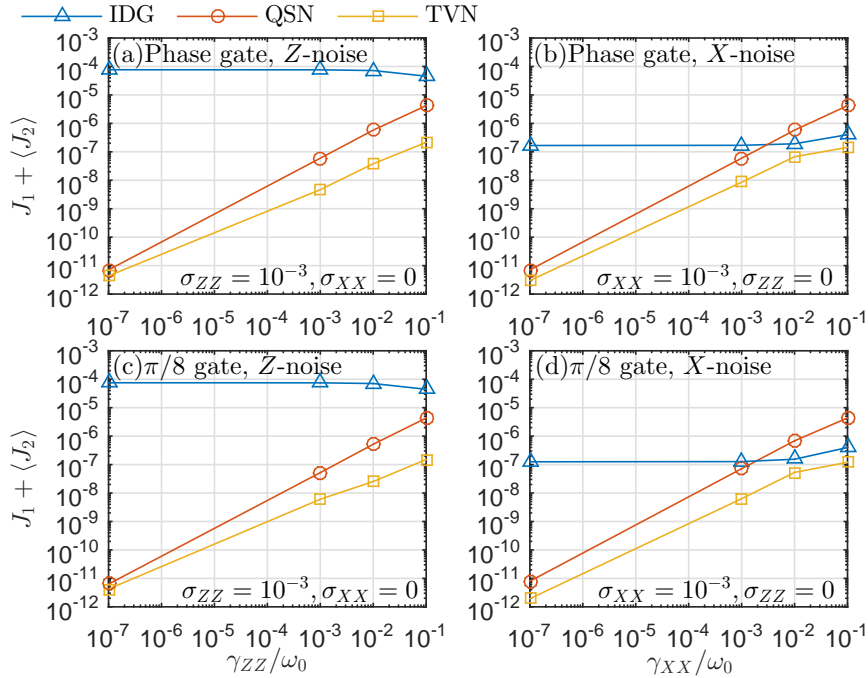
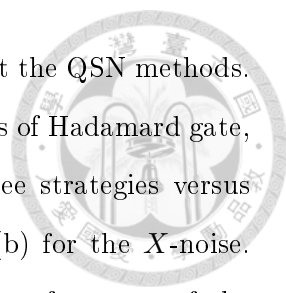


Figure 2.2.: $J_1 + \langle J_2 \rangle$ values versus γ_{ZZ} for Z -noise ($\sigma_{ZZ} = 10^{-3}$, $\sigma_{XX} = 0$) and versus γ_{XX} for X -noise ($\sigma_{XX} = 10^{-3}$, $\sigma_{ZZ} = 0$) obtained from the IDG strategy (blue triangles), QSN strategy (red circles), and TVN strategy (yellow squares) for the phase gate shown in (a) and (b), respectively, and for the $\pi/8$ gate in (c) and (d), respectively.



the noise CFs in the cost function $\langle J_2 \rangle$. Thus it is regarded to represent the QSN methods. We choose the gate operation time $t_f = 20/\omega_0$. After the optimizations of Hadamard gate, we plot the corresponding $J_1 + \langle J_2 \rangle$ values obtained from these three strategies versus γ_{ZZ} in Figure 2.1(a) for the Z -noise and versus γ_{XX} in Figure 2.1(b) for the X -noise. For low-frequency (quasi-static) noise ($\gamma_{ZZ} = \gamma_{XX} = 10^{-7}\omega_0$), the performance of the TVN strategy and the QSN strategy are about the same but they are several orders of magnitude better in infidelity $J_1 + \langle J_2 \rangle$ value than the IDG strategy which does not take the noise into account at all. As the noise goes from the low frequency to high frequency ($\gamma_{ZZ} = \gamma_{XX} = 10^{-1}\omega_0$), the TVN strategy taking account of the TVN information in the cost function gets better and better (from a factor-level to an order-of-magnitude-level) improvement in $J_1 + \langle J_2 \rangle$ values than the QSN strategy in which noise is assumed to be quasi-static. In addition to the Hadamard gate, we perform calculations for other quantum gates, namely the phase gate, $\pi/8$ gate and controlled-NOT (CNOT) gate, in the fault-tolerant universal set in terms of which any unitary operation can be expressed to arbitrary accuracy. The $J_1 + \langle J_2 \rangle$ values versus γ_{ZZ} and versus γ_{XX} obtained from the three strategies are shown in Figures 2.2(a) and (b), respectively, for the phase gate and in Figures 2.2(c) and (d), respectively, for the $\pi/8$ gate. Their performances are similar to those in Figure 2.1(a) and (b) of the Hadamard gate. The optimization results for the two-qubit CNOT gate are presented in Sec. 2.3.1.2.

Next, we take the optimal control parameter sets of the Hadamard gate from these three strategies to show their robust performance against Z -noise, X -noise, and Z -& X -noise at a low frequency ($\gamma_{ZZ} = \gamma_{XX} = 10^{-7}\omega_0$) in Figures 2.3(a), (b), and (c) and at a high frequency ($\gamma_{ZZ} = \gamma_{XX} = 10^{-1}\omega_0$) in Figures 2.4(a), (b), and (c). For low-frequency noise and for low noise strength ($\sigma_{XX} < 10^{-1}$, $\sigma_{ZZ} < 10^{-1}$), one can see in Figure 2.3 that the full-order ensemble average infidelity $\langle \mathcal{I} \rangle$ scales for the IDG strategy as the second power of the noise standard deviation (σ_{ZZ} , σ_{XX}) but scales for the TVN and QSN strategies as the fourth power. This implies that $\langle \mathcal{I} \rangle \cong \langle J_2 \rangle$ for the IDG strategy, but the TVN and QSN strategies can nullify the contribution from $\langle J_2 \rangle$ for the low-frequency (quasi-static) noise and the dominant contribution in $\langle \mathcal{I} \rangle$ comes from the next higher-order term, i.e., $\langle \mathcal{I} \rangle \cong \langle \mathcal{O}(\tilde{\mathcal{H}}_N^4) \rangle$. In this case, our method, the TVN strategy, still performs slightly better than the QSN strategy. For gate error (infidelity) less than the error threshold of 10^{-2} of surface codes required for FTQC, the Hadamard gate of TVN strategy can be robust

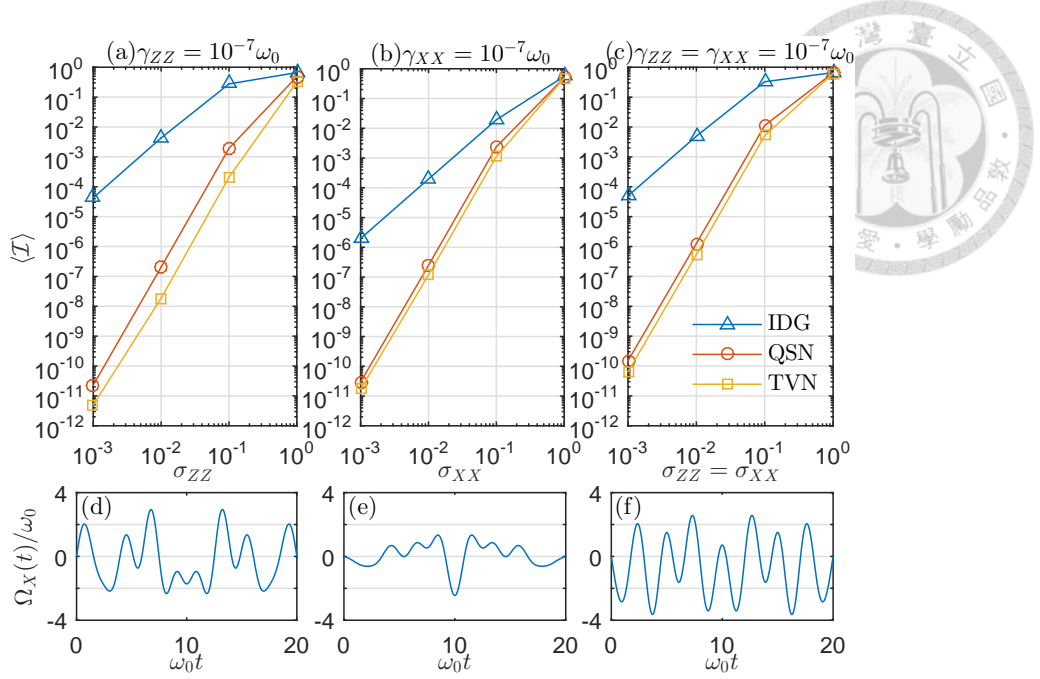


Figure 2.3.: Robust performance of the Hadamard gate of the IDG strategy (blue triangles), QSN strategy (red circles), and TVN strategy (yellow squares) for low-frequency ($\gamma_{ZZ} = \gamma_{XX} = 10^{-7}\omega_0$) (a) Z -noise, (b) X -noise, and (c) Z -&- X -noise. The corresponding optimal control pulses of the TVN strategy for Z -noise, X -noise, and Z -&- X -noise are shown in (d), (e), and (f), respectively. The number of control parameters $k_{\max}=10$ for $\Omega_X(t)$ in (d)-(f).

to $\sigma_{ZZ} \sim 30\%$ for low-frequency Z -noise (i.e., against noise fluctuation with a standard deviation up to about 30% of $\omega_0/2$), robust to $\sigma_{XX} \sim 20\%$ for the X -noise [i.e., against noise fluctuation with a standard deviation up to about 20% of $\Omega_X(t)/2$], and robust to $\sigma_{ZZ} = \sigma_{XX} \sim 10\%$ for Z -&- X -noise as shown in Figures 2.3(a), (b), and (c), respectively. The corresponding optimal control pulses of the TVN strategy are shown in Figures 2.3(d), (e), and (f), respectively.

For high-frequency noise shown in Figure 2.4, the full-order ensemble average infidelity $\langle \mathcal{I} \rangle$ scales as the second power of the noise standard deviation (σ_{ZZ} , σ_{XX}) for all three strategies and noises. This indicates that for high-frequency noise $\langle J_2 \rangle$ is not nullified completely, and is only minimized. Even in this case, the TVN strategy still has over two orders of magnitude improvement in $\langle \mathcal{I} \rangle$ compared with the IDG strategy, and over one order of magnitude improvement compared with the QSN strategy for the Z -noise at small noise strengths as shown in Figure 2.4(a). For $\langle \mathcal{I} \rangle \lesssim 10^{-2}$ less than the FTQC error threshold of the surface codes, the Hadamard gate implemented by our optimal control pulse shown in Figure 2.4(d) can be robust to $\sigma_{ZZ} \sim 20\%$ for the Z -noise. On the other hand, for the high-frequency X -noise, $\langle \mathcal{I} \rangle$ obtained by the QSN strategy has

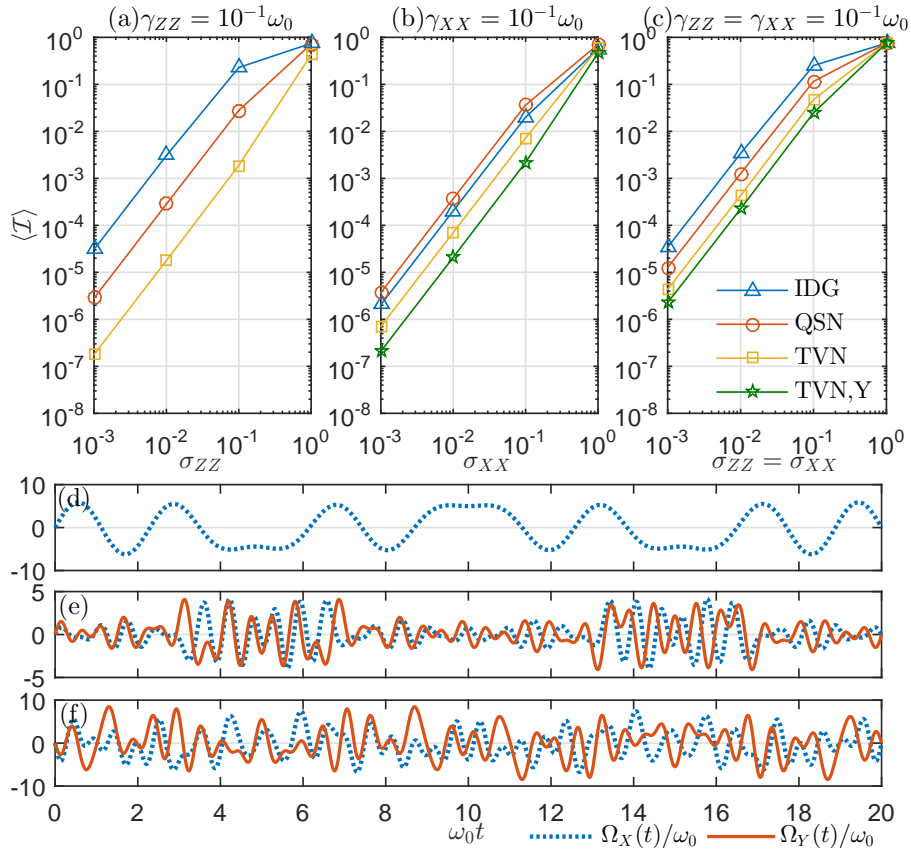
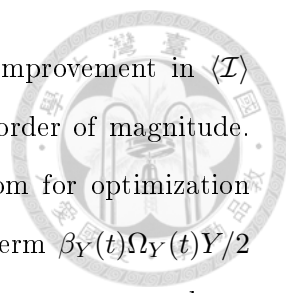


Figure 2.4.: Robust performance of the Hadamard gate of the IDG strategy (blue triangles), QSN strategy (red circles), and TVN strategy (yellow squares) for high-frequency ($\gamma_{ZZ} = \gamma_{XX} = 10^{-1}\omega_0$) (a) Z-noise, (b) X-noise, and (c) Z-&-X-noise. For TVN strategy with an additional Y control (green pentagrams) in (b), $\gamma_{YY} = \gamma_{XX} = 10^{-1}\omega_0$ and $\sigma_{YY} = \sigma_{XX}$, and in (c), $\gamma_{YY} = \gamma_{ZZ} = \gamma_{XX} = 10^{-1}\omega_0$ and $\sigma_{YY} = \sigma_{XX} = \sigma_{ZZ}$. Optimal control pulses of the TVN strategy (d) for Z-noise and of the TVN strategy with an additional Y control and accompanying Y-noise (e) for X-noise and (f) for Z-&-X-noise. The number of control parameters $k_{\max}=10$ for $\Omega_X(t)$ in (d) and $k_{\max}=20$ for both $\Omega_X(t)$ and $\Omega_Y(t)$ in (e) and (f).



even slightly higher values than those by the IDG strategy. The improvement in $\langle \mathcal{I} \rangle$ by the TVN strategy over the other two strategies is less than one order of magnitude. To improve the gate performance, we increase the degrees of freedom for optimization by adding a control term $\Omega_Y(t)Y/2$ and its accompanying Y -noise term $\beta_Y(t)\Omega_Y(t)Y/2$ in the Hamiltonian. We choose, for simplicity, $\gamma_{YY} = \gamma_{XX}$ and $\sigma_{YY} = \sigma_{XX}$, and use the same optimal procedure as the TVN strategy. The improvement in $\langle \mathcal{I} \rangle$ of the TVN strategy with an additional Y control as compared with the TVN strategy is over a half order of magnitude. As a result, the Hadamard gate with the optimal control pulses of the TVN strategy with an additional Y control shown in Figure 2.4(e) can be robust to $\sigma_{XX} = \sigma_{YY} \sim 20\%$ for $\langle \mathcal{I} \rangle \lesssim 10^{-2}$. Note that the optimization algorithm seems to find control pulses with stronger strengths to suppress the Z -noise, but searches weaker control pulses to minimize the X -noise cost function since the system coupling operator term of the X -noise is proportional to the control field $\Omega_X(t)$ in our noise model. So for the case with the Z -noise and X -noise simultaneously present, there is a trade-off in the control pulse strength for the cost function optimization between the Z -noise and the X -noise. Consequently, the ensemble infidelity of the Z -&- X noise does not reach a low value as in the case with only Z -noise or X -noise. Thus one can see from Figure 2.4(c) that the improvement in $\langle \mathcal{I} \rangle$ of the TVN strategy over the IDG strategy is just near one order of magnitude, and only a half order as compared with the QSN strategy. A similar trade-off also takes place for the TVN strategy with additional Y control, although it performs slightly better than the TVN strategy with only the $\Omega_X(t)$ control field. Nevertheless, the Hadamard gate implemented with the optimal pulse obtained by the TVN strategy with additional Y control shown in Figure 2.4(f) can be still robust to $\sigma_{ZZ} = \sigma_{XX} = \sigma_{YY} \sim 6\%$ for $\langle \mathcal{I} \rangle \lesssim 10^{-2}$.

2.3.1.2. Two-qubit gates

Next, we demonstrate that our method can find control pulses for high-fidelity two-qubit CNOT gate operations in the presence of multiple sources of high-frequency noise. The two-qubit Hamiltonian is chosen as

$$\mathcal{H}_I(t) = \omega_0 \frac{Z_1}{2} + \Omega_{X_1}(t) \frac{X_1}{2} + \omega_0 \frac{Z_2}{2} + \Omega_{X_2}(t) \frac{X_2}{2} + J(t) \frac{Z_1 Z_2}{2}, \quad (2.22)$$

where Z_j and X_j denote the Pauli's matrix operators for qubit j , $\Omega_{X_j}(t)$ is the control field applied to qubit j and $J(t)$ is the two-qubit coupling strength. We assume OU noise can be present in each of the five terms, and σ_{ZZ1} , σ_{ZZ2} , σ_{XX1} , σ_{XX2} , and σ_{JJ} are, respectively, the corresponding standard deviation σ_{OU} , and γ_{ZZ1} , γ_{ZZ2} , γ_{XX1} , γ_{XX2} , and γ_{JJ} are, respectively, the corresponding γ_{OU} . We choose the control fields $\Omega_{X_1}(t)$ and $\Omega_{X_2}(t)$ as composite sine pulses, and the two-qubit control $J(t)$ as a composite sine pulse with a constant shift.

The robust performance of the CNOT gate using the three strategies for high-frequency ($\gamma_{ZZ1} = \gamma_{ZZ2} = \gamma_{XX1} = \gamma_{XX2} = \gamma_{JJ} = 10^{-1}\omega_0$) Z -noise, X -&- J -noise, and Z -&- X -&- J -noise are shown in Figures 2.5(a), (b), and (c), respectively. The corresponding optimal control pulses of the TVN strategy for operation time $t_f = 100/\omega_0$ are shown in Figures 2.5(d), (e), and (f), respectively. For $\omega_0 t_f = 100$, our method (the TVN strategy) in the case of the Z -noise and the case of the X -&- J -noise shows a one order of magnitude improvement in $\langle \mathcal{I} \rangle$ values compared with the QSN strategy for low noise strength, but only a half-order improvement in the case of the Z -&- X -&- J -noise. This is because in the case of the Z -&- X -&- J -noise, there is a trade-off in the control pulse strength for the cost function optimization between the Z -noise and the X -&- J -noise, similar to that in the single-qubit case. The robust performance can be improved by reducing gate operation time t_f , for example, from $t_f = 100/\omega_0$ to $t_f = 20/\omega_0$, to decrease the duration of the influence of the noises. This can be seen from the purple pentagrams in Figures 2.5(a) and (c). In the case of the X -&- J -noise in Figure 2.5(b), only slight improvement is observed for the $t_f = 20/\omega_0$ case because when the operation time decreases, it is hard to make the strengths of the control fields $\Omega_X^j(t)$ and $J(t)$ all low as in the $t_f = 100/\omega_0$ case. For high-frequency noise and for FTQC error threshold $\langle \mathcal{I} \rangle \lesssim 10^{-2}$ of the surface codes, the CNOT gate with operation time $t_f = 20/\omega_0$ can be robust to $\sigma_{ZZ1} = \sigma_{ZZ2} \sim 10\%$ for the Z -noise, robust to $\sigma_{XX1} = \sigma_{XX2} = \sigma_{JJ} \sim 10\%$ for the X -&- J -noise, and robust to $\sigma_{ZZ1} = \sigma_{ZZ2} = \sigma_{XX1} = \sigma_{XX2} = \sigma_{JJ} \sim 3\%$ for the Z -&- X -&- J -noise by our method.

We describe briefly about the computational resources and computation time in our calculations. In the case of the Z -&- X -&- J -noise, we use 40 control parameters in a parameter set to run the two-step optimization for the two-qubit CNOT gate, and choose 100 random initial guesses of the parameter sets for the first-step optimization and 10 parameter sets obtained in the first-step optimization as initial guesses for the second step

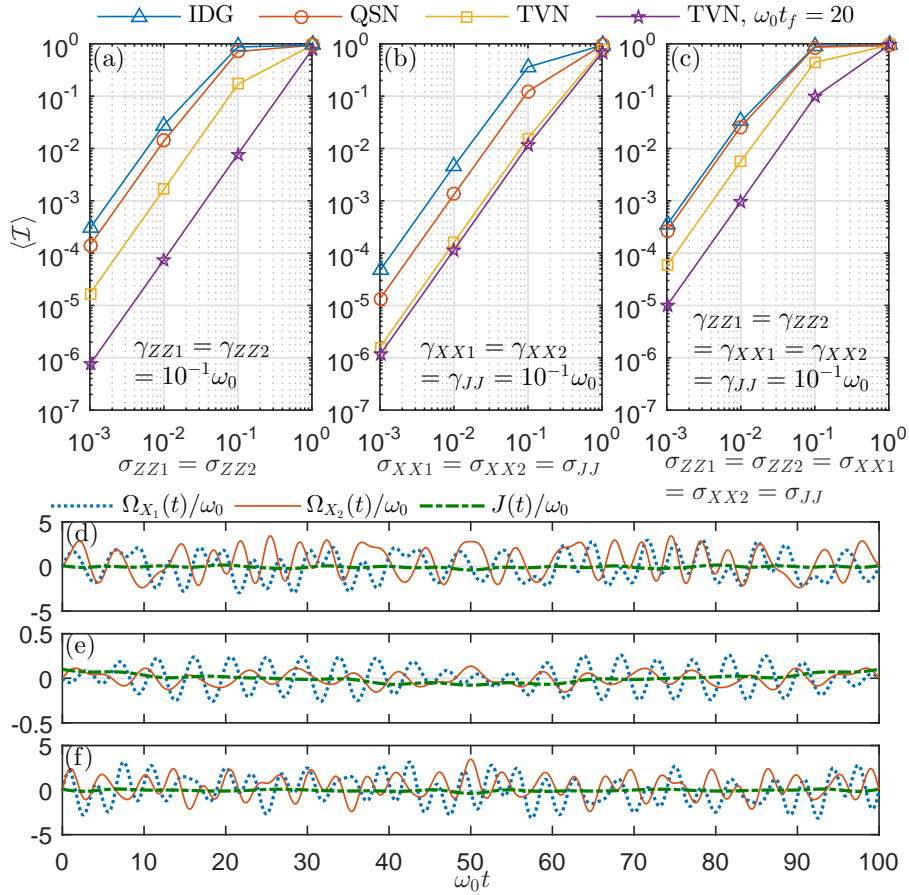


Figure 2.5.: Robust performance of CNOT gates of the IDG strategy ($\omega_0 t_f = 100$, blue triangles), QSN strategy ($\omega_0 t_f = 100$, red circles), TVN strategy ($\omega_0 t_f = 100$, yellow squares; and $\omega_0 t_f = 20$, purple pentagrams) for high-frequency ($\gamma_{ZZ1} = \gamma_{ZZ2} = \gamma_{XX1} = \gamma_{XX2} = \gamma_{JJ} = 10^{-1}\omega_0$) (a) Z-noise, (b) X-&-J-noise, and (c) Z-&-X-&-J-noise. The optimal control pulses of the TVN strategy ($\omega_0 t_f = 100$) for the Z-noise, X-&-J-noise, and Z-&-X-&-J-noise are shown in (d), (e), and (f), respectively. The numbers of control parameters $k_{\max}=16, 16$, and 8 for $\Omega_{X_1}(t)$, $\Omega_{X_2}(t)$, and $J(t)$, respectively, in (d) and (f); $k_{\max}=12, 12$, and 6 for $\Omega_{X_1}(t)$, $\Omega_{X_2}(t)$, and $J(t)$, respectively, in (e).

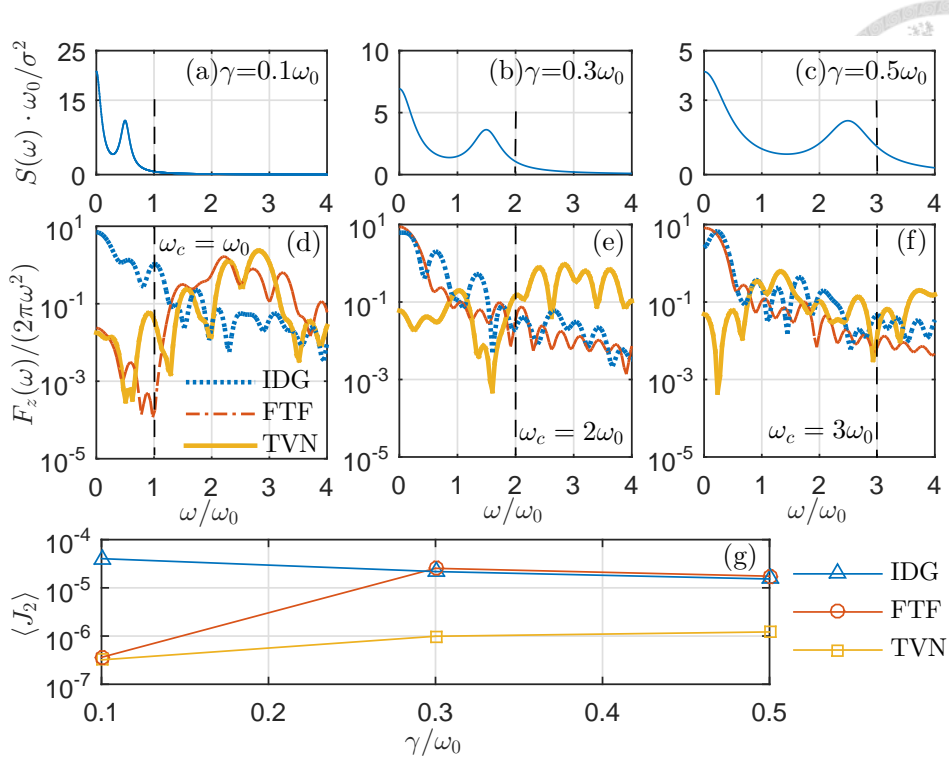


Figure 2.6.: The behavior of $[F_z(\omega)/(2\pi\omega^2)]$ obtained using the optimal control parameter sets from the IDG strategy (thick dotted blue line), FTF strategy (thin dash-dotted red line), and TVN strategy (thick solid yellow line) for the noise PSD $S(\omega)$ with (a) $\gamma = 0.1\omega_0$, (b) $\gamma = 0.3\omega_0$, and (c) $\gamma = 0.5\omega_0$ is shown in (d), (e), and (f), respectively. (g) The corresponding $\langle J_2 \rangle$ values.

optimization. We use a total of 60 2-GHz-CPU cores and it takes about 2 days to obtain the control pulses and robust performance calculations of Figure 2.5(c). These resources and time spent to construct the robust high-fidelity CNOT gates against five sources of high-frequency noise are quite acceptable.

2.3.2. Comparison with the filter-transfer-function method

In this subsection, we compare our method with the FTF method [48, 49, 50]. The cost function $\langle J_2 \rangle$ in Eq. (2.16) can be transformed to the frequency domain as

$$\langle J_2 \rangle = \sum_j \frac{1}{2\pi} \int_{-\infty}^{\infty} \frac{d\omega}{\omega^2} S_j(\omega) F_j(\omega), \quad (2.23)$$

where $S_j(\omega)$ is the noise PSD for the j -th noise, and $F_j(\omega)$ is the corresponding filter-transfer function. The cost function of the j -th noise for optimization in the FTF method is defined as $A_j \equiv \int_{\omega_L}^{\omega_c} F_j(\omega) d\omega$ [48, 49, 50]. The region $[\omega_L, \omega_c]$ of the integration of the cost function A_j is determined by the non-negligible region of the noise PSD. In order

to compare with our method, we use the same form of control pulse, the same number of control parameters, and the same optimal procedure except, for the FTF method, changing the cost function from $J_1 + \langle J_2 \rangle$ to $J_1 + A_j$ in the second step of the two-step optimization. We call this procedure the FTF strategy. Then we apply the IDG strategy, FTF strategy, and TVN strategy to find high-fidelity Hadamard gate for one-qubit system with single Z -noise. To demonstrate the advantage of our method over the FTF method, we choose the noise PSD for the Z -noise to contain a high-frequency distribution as

$$S(\omega) = \sigma^2 \left[\frac{2\gamma}{\gamma^2 + \omega^2} + \frac{\gamma}{\gamma^2 + (5\gamma - \omega)^2} + \frac{\gamma}{\gamma^2 + (5\gamma + \omega)^2} \right] \quad (2.24)$$

that has two peaks at $\omega = 0$ and $\omega = 5\gamma$. As the value of γ increases, the dominant distribution associated with the second peak of the PSD $S(\omega)$ moves to a high frequency region in which the FTF method may not work very effectively. We demonstrate that our method, including the detailed noise PSD distribution in the cost function, can still in this case suppress the gate error coming from $S(\omega)$, a PSD different from that in the OU noise model used previously. The lower limit ω_L of the integral of the cost function A_z for the FTF strategy is chosen to be zero, and the upper limit ω_c is chosen to be $1\omega_0$, $2\omega_0$, and $3\omega_0$ to enclose the dominant distribution of $S(\omega)$ [see Figures 2.6(a), (b), and (c)] for $\gamma = 0.1\omega_0$, $0.3\omega_0$, and $0.5\omega_0$, respectively. For the single Z -noise considered here, the infidelity from Eq. (2.23) is $\langle J_2 \rangle = \int_{-\infty}^{\infty} d\omega S(\omega) [F_z(\omega)/(2\pi\omega^2)]$. The improvement of $\langle J_2 \rangle$ can be analyzed through the overlap of $S(\omega)$ with $[F_z(\omega)/(2\pi\omega^2)]$ [45]. If the control pulses can make $[F_z(\omega)/(2\pi\omega^2)]$ small in the dominant distribution region of $S(\omega)$, then $\langle J_2 \rangle$ can be significantly improved (reduced). We plot $[F_z(\omega)/(2\pi\omega^2)]$ evaluated by the optimal control parameter sets obtained from the above three strategies for three different values of $\gamma = 0.1\omega_0$, $0.3\omega_0$, and $0.5\omega_0$ of $S(\omega)$ in Figures 2.6(d), (e), and (f), respectively. The corresponding $\langle J_2 \rangle$ values are shown in Figure 2.6(g). By taking the case of $\gamma = 0.3\omega_0$ as an example, the function $[F_z(\omega)/(2\pi\omega^2)]$ of the TVN strategy shows apparent drops near the two peaks of the noise PSD at $\omega = 0$ and $\omega = 1.5\omega_0$, but the function for the FTF strategy and the IDG strategy does not. Thus, about one order of magnitude improvement in $\langle J_2 \rangle$ of the TVN strategy over the other two strategies is observed. In short, as the range of dominant distribution of the PSD enlarges [e.g., from Figure 2.6(a) to Figure 2.6(c)], the TVN strategy, including the detailed noise information (CF) in the optimization cost

function [45], can suppress the dominant infidelity contribution more effectively than the FTF strategy. Furthermore, the concatenation method is used to construct control pulses against two different non-commuting noises in the FTF method [49, 50]. But using the concatenation method to deal with the case of multicontrols, multiple sources of noise, and multiqubits may be very complicated. On the other hand, our method can find robust control pulses for high-fidelity CNOT gates that involve three control knobs and up to five sources of high-frequency noise as demonstrated in Figure 2.5.

2.4. Generalization to open quantum system

From Sec. 2.1 to Sec. 2.3, we describe the dynamics of the qubits in the space which includes the degrees of freedom in the qubit-system only, and doesn't include those in the environment, that is, we treat the problems in a closed system. For an open quantum system, the dynamics of the qubits is described in the space which includes the qubit-system subspace (degrees of freedom in the qubit-system) and the environment subspace (degrees of freedom in the environment). Thus the total Hamiltonian of an open quantum system can be written as

$$\mathcal{H}(t) = \mathcal{H}_S(t) + \mathcal{H}_{CN}(t) + \mathcal{H}_E(t) + \mathcal{H}_{QN}(t). \quad (2.25)$$

Here $\mathcal{H}_S(t)$ and $\mathcal{H}_{CN}(t)$ are defined in the qubit-system subspace, and $\mathcal{H}_S(t)$ is the ideal qubit-system Hamiltonian and $\mathcal{H}_{CN}(t)$ is the classical noise Hamiltonian, which correspond to $\mathcal{H}_I(t)$ and $\mathcal{H}_N(t)$, respectively, discussed in a closed system from Sec. 2.1 to Sec. 2.3. $\mathcal{H}_E(t)$ is the environment Hamiltonian and is defined in the environment subspace. In an open quantum system, except the classical noise, the quantum noise also degrades the gate fidelity and is described by the quantum noise Hamiltonian $\mathcal{H}_{QN}(t)$, coupling the qubit-system subspace and the environment subspace together. Detailed form of these Hamiltonians in Eq. (2.25) are shown below:



$$\mathcal{H}_S(t) = H_S(t) \otimes I^E, \quad (2.26)$$

$$\mathcal{H}_{CN}(t) = \left[\sum_j \beta_j(t) S_{CN_j}(t) \right] \otimes I^E, \quad (2.27)$$

$$\mathcal{H}_E(t) = I^S \otimes H_E(t), \quad (2.28)$$

$$\mathcal{H}_{QN}(t) = \sum_j S_{QN_j}(t) \otimes E_j(t). \quad (2.29)$$

Here I^E and I^S are the identity operators in the environment subspace and in the qubit-system subspace, respectively. $H_S(t)$ is the ideal qubit-system Hamiltonian operator in the qubit-system subspace, and $H_E(t)$ is the environment Hamiltonian operator in the environment subspace. In Eq. (2.27), $\beta_j(t)$ is the strength of the j -th classical noise and $S_{CN_j}(t)$ is the corresponding system coupling operator term. For the quantum noise Hamiltonian in Eq. (2.29), $S_{QN_j}(t)$ and $E_j(t)$ are the system-environment coupling operators in the qubit-system subspace and in the environment subspace, respectively. In fact, if we choose $E_j(t) = \beta_j(t)I^E$, quantum noise recovers to classical noise, but the treatment processes for classical noise and quantum noise are somewhat different, so we separate them.

Following treatment processes are similar to those in a closed system in Sec. 2.1. First, we transform the Hamiltonian to the interaction picture by $U_S(t) \otimes U_E(t)$, where

$$U_S(t) = \mathcal{T}_+ \exp\left[-i \int_0^t H_S(t') dt'\right], \quad (2.30)$$

$$U_E(t) = \mathcal{T}_+ \exp\left[-i \int_0^t H_E(t') dt'\right] \quad (2.31)$$

are the ideal qubit-system propagator and the environment propagator, respectively. Then the total Hamiltonian in the interaction picture becomes $\tilde{\mathcal{H}}_{CN}(t) + \tilde{\mathcal{H}}_{QN}(t)$, where

$$\tilde{\mathcal{H}}_{CN}(t) = \left[\sum_j \beta_j(t) R_{CN_j}(t) \right] \otimes I^E, \quad (2.32)$$

$$\tilde{\mathcal{H}}_{QN}(t) = \sum_j R_{QN_j}(t) \otimes R_{E_j}(t), \quad (2.33)$$

and

$$R_{CN_j}(t) \equiv U_S^\dagger(t) S_{CN_j}(t) U_S(t), \quad (2.34)$$

$$R_{QN_j}(t) \equiv U_S^\dagger(t) S_{QN_j}(t) U_S(t), \quad (2.35)$$

$$R_{E_j}(t) \equiv U_E^\dagger(t) E_j(t) U_E(t). \quad (2.36)$$



The total propagator in the interaction picture at the gate operation time t_f is

$$\tilde{U}(t_f) = \mathcal{T}_+ \exp[-i \int_0^{t_f} (\tilde{\mathcal{H}}_{CN}(t) + \tilde{\mathcal{H}}_{QN}(t)) dt']. \quad (2.37)$$

If the strength of both classical noise and quantum noise is not too large, we can expand $\tilde{U}(t_f)$ by Dyson series [75] as the form $\tilde{U}(t_f) = I + \Psi_1 + \Psi_2 + \dots$, where the first two terms of Ψ_j are

$$\Psi_1 = -i \int_0^{t_f} [\tilde{\mathcal{H}}_{CN}(t) + \tilde{\mathcal{H}}_{QN}(t)] dt', \quad (2.38)$$

$$\Psi_2 = - \int_0^{t_f} dt_1 \int_0^{t_1} dt_2 [\tilde{\mathcal{H}}_{CN}(t_1) + \tilde{\mathcal{H}}_{QN}(t_1)] [\tilde{\mathcal{H}}_{CN}(t_2) + \tilde{\mathcal{H}}_{QN}(t_2)]. \quad (2.39)$$

The total propagator in the original frame becomes

$$U(t_f) = [U_S(t_f) \otimes U_E(t_f)] \cdot (I + \Psi_1 + \Psi_2 + \dots). \quad (2.40)$$

Next derivations are different from those in a closed system in Sec. 2.1. In general, the dynamics of an open quantum system is described by a density matrix

$$\rho(t) = U(t) \rho(0) U^\dagger(t). \quad (2.41)$$

Here we assume the initial density matrix is separable, $\rho(0) = \rho_S(0) \otimes \rho_E(0)$, and $\rho_S(0)$ is the initial density matrix in the qubit-system subspace, and $\rho_E(0)$ is the initial density matrix in the environment subspace. To see the quantum noise contribution to the ensemble average gate infidelity, we need to trace over the degrees of freedom in the environment to

obtain the reduced density matrix in the qubit-system subspace as

$$\rho_S(t) = \text{Tr}_E \rho(t) = U_S(t) (\rho_S(0) + \bar{\Psi}_1 + \bar{\Psi}_2 + \dots) U_S^\dagger(t), \quad (2.42)$$

where the definitions of $\bar{\Psi}_1$ and $\bar{\Psi}_2$ are

$$\bar{\Psi}_1 \equiv \text{Tr}_E[\Psi_1(\rho_S(0) \otimes \rho_E(0)) + \text{h.c.}], \quad (2.43)$$

$$\bar{\Psi}_2 \equiv \text{Tr}_E[\Psi_2(\rho_S(0) \otimes \rho_E(0)) + \text{h.c.}] + \text{Tr}_E[\Psi_1(\rho_S(0) \otimes \rho_E(0))\Psi_1^\dagger]. \quad (2.44)$$

Here “h.c.” is the abbreviation of Hermitian conjugate. Tr_E denotes tracing over the degrees of freedom in the environment subspace only it acts on. To see the classical noise contribution to the ensemble average infidelity, we can take the ensemble average of the reduced density matrices $\rho_S(t)$ in Eq. (2.42) over different classical noise realizations or take the ensemble average of infidelities later, and no matter the former method or the latter method, we can obtain the same results. And we use the latter method to derive the cost functions.

In order to obtain the propagator for the reduced density matrix $\rho_S(t)$, we should vectorize it as

$$\text{vec}[\rho_S(t)] = G(t)\text{vec}[\rho_S(0)]. \quad (2.45)$$

Here $\text{vec}[\rho_S(0)]$ is the initial vectorized reduced density matrix, $\text{vec}[\rho_S(t)]$ is the vectorized reduced density matrix at time t , the symbol vec denotes vectorizing the matrix it acts on, for example, in one-qubit system $\text{vec}[\rho_S(t)] = (\rho_{S,11}(t), \rho_{S,21}(t), \rho_{S,12}(t), \rho_{S,22}(t))^T$, and

$$G(t) \equiv [U_S^\star(t) \otimes U_S(t)] \cdot (I + \bar{\psi}_1 + \bar{\psi}_2 + \dots). \quad (2.46)$$

is the propagator of the vectorized reduced density matrix. The relation between $\bar{\Psi}_j$ in Eq. (2.42) and $\bar{\psi}_j$ in Eq. (2.46) is

$$\text{vec}[\bar{\Psi}_j] \equiv \bar{\psi}_j \text{vec}[\rho_S(0)]. \quad (2.47)$$



Now we can define the gate infidelity in an open quantum system as

$$\mathcal{I}_{\text{open}} \equiv 1 - \frac{1}{2^{2n}} \text{Re}\{\text{Tr}[G_T^\dagger G(t_f)]\}, \quad (2.48)$$

where $G_T = U_T^* \otimes U_T$ is the target gate for the vectorized reduced density matrix, and U_T is the target gate in the qubit-system subspace, n is the qubit number. Tr here denotes a trace over the matrix it acts on. The gate infidelity definition in an open quantum system $\mathcal{I}_{\text{open}}$ in Eq. (2.48) can recover to the gate infidelity definition in a closed system \mathcal{I} in Eq. (2.2) if $G(t)$ can be written as $G(t) = V^*(t) \otimes V(t)$, where $V(t)$ is a matrix with the same dimensions as U_T . Substituting $G(t)$ in Eq. (2.46) and G_T into $\mathcal{I}_{\text{open}}$ in Eq. (2.48), we can obtain the expanded $\mathcal{I}_{\text{open}}$ as

$$\mathcal{I}_{\text{open}} = J_1 + J_{2,\text{open}} + \xi + \mathcal{O}(\tilde{\mathcal{H}}_{CN}^m, \tilde{\mathcal{H}}_{QN}^m, m \geq 3), \quad (2.49)$$

$$J_1 \equiv 1 - \frac{1}{2^{2n}} \text{Re}\{\text{Tr}[G_T^\dagger G_S(t_f)]\}, \quad (2.50)$$

$$J_{2,\text{open}} \equiv -\frac{1}{2^{2n}} \text{Re}[\text{Tr}(\bar{\psi}_1 + \bar{\psi}_2)]. \quad (2.51)$$

The forms of above equations are similar to those in a closed system from Eq. (2.12) to Eq. (2.14). Here J_1 is the definition of gate infidelity for the ideal qubit-system, where $G_S(t) \equiv [U_S^*(t) \otimes U_S(t)]$ and $U_S(t)$ is the ideal qubit-system propagator in Eq. (2.30). $J_{2,\text{open}}$ is the lowest-order contribution of the classical noise and the quantum noise to the gate infidelity; the function of ξ is equivalent to that of ϵ in a closed system as discussed in Appendix A, and $\mathcal{O}(\tilde{\mathcal{H}}_{CN}^m, \tilde{\mathcal{H}}_{QN}^m, m \geq 3)$ represents other higher-order terms of noise excluding ξ . Substituting the definition of $\bar{\psi}_1$ and $\bar{\psi}_2$ into $J_{2,\text{open}}$ in Eq. (2.51), we can easily obtain $\text{Tr}(\bar{\psi}_1) = 0$ without extra assumptions, and thus $J_{2,\text{open}} = -\text{Re}[\text{Tr}(\bar{\psi}_2)]/2^{2n}$.

For quantum noise, $\mathcal{I}_{\text{open}}$ has been the ensemble average infidelity because the action of taking the ensemble average for quantum noise has been done when we trace the degrees of freedom in the environment to obtain the reduced density matrix in Eq. (2.42). Next, for classical noise, we take the ensemble average of $\mathcal{I}_{\text{open}}$ over different classical noise realizations to obtain the complete ensemble average infidelity for both classical noise and



quantum noise

$$\langle \mathcal{I}_{\text{open}} \rangle = J_1 + \langle J_{2,\text{open}} \rangle + \langle \xi \rangle + \left\langle \mathcal{O}(\tilde{\mathcal{H}}_{CN}^m, \tilde{\mathcal{H}}_{QN}^m, m \geq 3) \right\rangle,$$



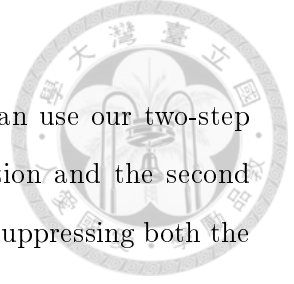
where

$$\begin{aligned} \langle J_{2,\text{open}} \rangle &= \sum_{j,k} \int_0^{t_f} dt_1 \int_0^{t_1} dt_2 C_{jk}^{CN}(t_1, t_2) \cdot \text{Tr}[R_{CN_j}(t_1)R_{CN_k}(t_2)]/2^{n-1} \\ &\quad - \sum_{j,k} \int_0^{t_f} dt_1 \int_0^{t_f} dt_2 C_{jk}^{CN}(t_1, t_2) \cdot \text{Tr}[R_{CN_j}(t_1)]\text{Tr}[R_{CN_k}(t_2)]/4^n \\ &\quad + \sum_{j,k} \int_0^{t_f} dt_1 \int_0^{t_1} dt_2 \text{Re}[C_{jk}^{QN}(t_1, t_2)] \cdot \text{Tr}[R_{QN_j}(t_1)R_{QN_k}(t_2)]/2^{n-1} \\ &\quad - \sum_{j,k} \int_0^{t_f} dt_1 \int_0^{t_f} dt_2 \text{Re}[C_{jk}^{QN}(t_1, t_2)] \cdot \text{Tr}[R_{QN_j}(t_1)]\text{Tr}[R_{QN_k}(t_2)]/4^n \\ &\quad + \sum_{j,k} \int_0^{t_f} dt_1 \int_0^{t_1} dt_2 \langle \beta_j(t_1) \rangle \text{Tr}_E[R_{E_k}(t_2)\rho_E(0)] \cdot \text{Tr}[R_{CN_j}(t_1)R_{QN_k}(t_2)]/2^{n-1} \\ &\quad + \sum_{j,k} \int_0^{t_f} dt_1 \int_0^{t_1} dt_2 \text{Tr}_E[R_{E_j}(t_1)\rho_E(0)] \langle \beta_k(t_2) \rangle \cdot \text{Tr}[R_{QN_j}(t_1)R_{CN_k}(t_2)]/2^{n-1} \\ &\quad - \sum_{j,k} \int_0^{t_f} dt_1 \int_0^{t_f} dt_2 \langle \beta_j(t_1) \rangle \text{Tr}_E[R_{E_k}(t_2)\rho_E(0)] \cdot \text{Tr}[R_{CN_j}(t_1)]\text{Tr}[R_{QN_k}(t_2)]/2^{2n-1}. \end{aligned} \tag{2.52}$$

Here $C_{jk}^{CN}(t_1, t_2) \equiv \langle \beta_j(t_1)\beta_k(t_2) \rangle$ is the correlation function of the classical noise $\beta_j(t_1)$ and $\beta_k(t_2)$; $C_{jk}^{QN}(t_1, t_2) \equiv \text{Tr}_E[R_{E_j}(t_1)R_{E_k}(t_2)\rho_E(0)]$ is the correlation function of the quantum noise $R_{E_j}(t_1)$ and $R_{E_k}(t_2)$. The first two terms in Eq. (2.52) are the lowest-order contribution of the classical noise to the ensemble average infidelity $\langle \mathcal{I}_{\text{open}} \rangle$, and these two terms are exactly the same as $\langle J_2 \rangle$ derived in a closed system in Eq. (2.16). The next two terms are the lowest-order contribution of the quantum noise to $\langle \mathcal{I}_{\text{open}} \rangle$, which have similar forms as those of the classical noise. The last three terms are the contribution from the combination of the classical noise and the quantum noise, and these three terms can be omitted if the classical noise has zero mean, $\langle \beta_j(t_1) \rangle = 0$, or the quantum noise has zero mean, $\text{Tr}_E(R_{E_j}(t_1)\rho_E(0)) = 0$. For this case, only the classical noise and quantum noise correlation functions, $C_{jk}^{CN}(t_1, t_2)$ and $C_{jk}^{QN}(t_1, t_2)$, the coupling operators to the ideal qubit-system, $S_{CN_j}(t)$ and $S_{QN_j}(t)$, and the ideal qubit-system Hamiltonian, $H_S(t)$, are

required to evaluate J_1 and $\langle J_{2,\text{open}} \rangle$ for optimization.

Once cost functions J_1 and $\langle J_{2,\text{open}} \rangle$ are defined clearly, then we can use our two-step optimization introduced in Sec. 2.2, with the first step J_1 optimization and the second step $J_1 + \langle J_{2,\text{open}} \rangle$ optimization, to find the optimal control pulses for suppressing both the classical noise and the quantum noise simultaneously.





3. Applications to quantum-dot electron spin qubits in isotopically purified silicon

In this chapter, we first give a brief introduction to quantum-dot electron spin qubits. Then we focus on the qubits in isotopically purified silicon: we describe the simulation skills for the ideal system, analyze the electrical noise and other factors degrading the gate fidelity in the realistic system, and finally we apply our robust control method for the system and demonstrate the performance of our optimal high-fidelity single-qubit gates and CNOT gates.

3.1. Quantum-dot electron spin qubits

The idea of quantum-dot electron spin qubits was first proposed by Loss and DiVincenzo [54] in 1998. In their model shown in Figure 3.1, the qubit is defined by the electron spin state in a single-electron semiconductor quantum dot, the two-qubit coupling via the exchange interaction is controlled by the tunnel coupling between two dots, an auxiliary ferromagnetic dot (FM) is designed to operate single-qubit gates, and another auxiliary dot with an electrometer is for spin state read-out, etc. They showed that the quantum-dot electron spin qubit was a promising candidate for realizing quantum computation because the five requirements for quantum computation, that is, identification of well-defined qubits, reliable state preparations, low decoherence, accurate quantum gate operations, and strong quantum measurements were all satisfied for their proposal.

Early development of this proposal mainly focused on III-V semiconductor quantum dots such as GaAs. And there were two major types of qubits for the realizations of the proposal, i.e., single-spin qubits and singlet-triplet ($S - T_0$) qubits. For single-spin

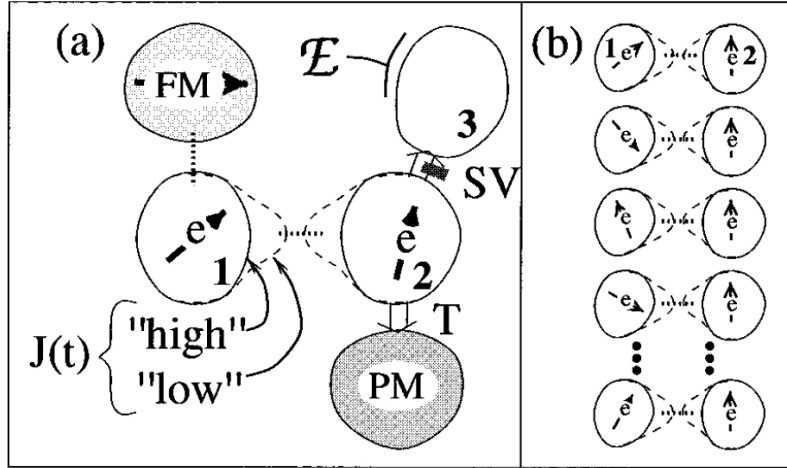


Figure 3.1.: Loss-and-DiVincenzo's model for quantum dot spin qubit (courtesy of Daniel Loss and David P. DiVincenzo, 1998).

qubits, the basis states are spin-up state $|\uparrow\rangle$ and spin-down state $|\downarrow\rangle$ of the electron in the single-electron quantum dot. The qubits were realized by F. H. L. Koppens et al. [56] in 2006, and the two-qubit gates via exchange interaction were also realized in 2011 [63, 64]. Another type of qubit is called the singlet-triplet ($S - T_0$) qubit, which was realized by J. R. Petta et al. [55] in 2005, and the basis states of the qubit are $|S\rangle = \frac{1}{\sqrt{2}}(|\uparrow\downarrow\rangle - |\downarrow\uparrow\rangle)$ and $|T_0\rangle = \frac{1}{\sqrt{2}}(|\uparrow\downarrow\rangle + |\downarrow\uparrow\rangle)$, which are constructed from spin states $|\uparrow\rangle$ or $|\downarrow\rangle$ of the electrons in two adjacent single-electron quantum dots. Because $|S\rangle$ and $|T_0\rangle$ states have zero magnetic quantum number, they are insensitive to uniform fluctuations in the magnetic field. Two-qubit gates via capacitive coupling of two adjacent $S - T_0$ qubits were realized in 2012 [65]. The architecture of single-spin qubit and $S - T_0$ qubit is shown in the left panel and right panel of Figures 3.2, respectively. The key drawback for these qubits is just the host material-GaAs itself. This is because all three nuclear species ^{69}Ga , ^{71}Ga , and ^{75}As of the host material GaAs have nuclear spin $3/2$ and typically there are $\sim 10^6$ nuclei in a quantum dot [80], strong hyperfine interaction (the coupling between the electron spin of the qubit and the nuclear spins of the host material) limits the dephasing time (T_2^*) of the qubit to be $\sim 10\text{ns}$.

The effective way to overcome the drawback is to replace the host material GaAs by the new material with more nuclear-spin-free atoms. Defining the quantum dots in silicon is a good choice because the most abundant stable silicon isotopes on earth are ^{28}Si ($\sim 92.2\%$), ^{29}Si ($\sim 4.7\%$), and ^{30}Si ($\sim 3.1\%$), and only ^{29}Si has nuclear spin $1/2$ and both ^{28}Si and ^{30}Si have zero nuclear spin. Therefore, for the qubits in the silicon-based quantum dots,

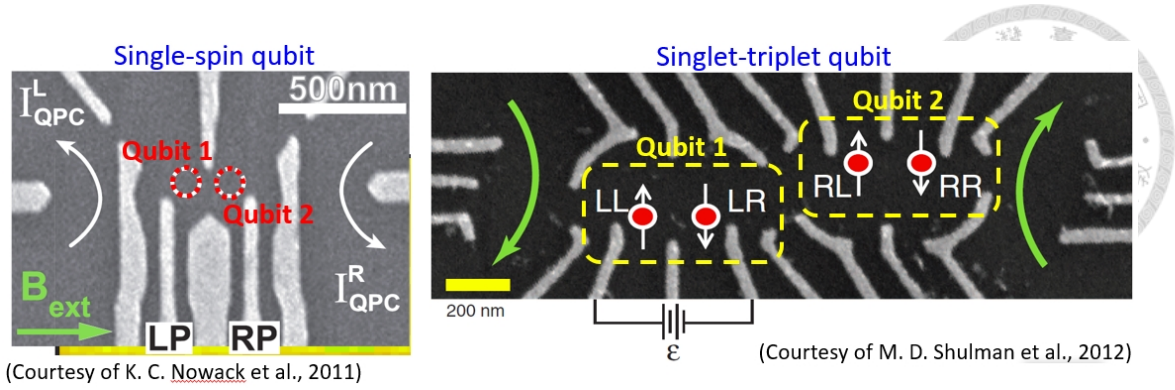


Figure 3.2.: The architecture of single-spin qubit (left panel) and singlet-triplet qubit (right panel) in GaAs semiconductor quantum dots.

the hyperfine interaction from the host material, silicon, can be largely reduced, that is the dephasing time (T_2^*) can be greatly improved. In the Si/SiGe quantum dots, T_2^* was improved to 360ns for the singlet-triplet qubits [69] in 2012, and to ~ 900 ns for single-spin qubits [70] in 2014. In the natural silicon quantum dots, T_2^* was further improved to $\sim 2\mu$ s for single-spin qubits [74] in 2016. However, the T_2^* is still limited by 5% ^{29}Si atoms (nuclear spin 1/2) in the natural silicon substrate. In 2014, M. Veldhorst et al. [71] defined the quantum dots in the isotopically purified ^{28}Si with a residual concentration of ^{29}Si 800 ppm, and then observed that T_2^* for the single-spin qubits is remarkably extended to 120μ s and realized the single qubit gates (a π -pulse 1.6μ s) with infidelity 4×10^{-3} below the threshold of surface codes 10^{-2} .

Another benefit for the quantum dots in the isotopically purified silicon is that the complete fabrication is compatible with the standard CMOS (complementary metal-oxide-semiconductor) manufacturing technology, an appealing feature to realize large-scale (many qubits) quantum computation. The fabrication process of the quantum dot in silicon starts from a MOSFET (metal-oxide-semiconductor field-effect transistor) including source (S), drain (D), and the gates (L1, L2) as shown in Figure 3.3 [81]. When the transistor is in inversion mode, the 2DEG (2-dimensional electron gas) appears underneath the gate oxide (SiO_2). Then the single-electron quantum dot underneath the gate electrode P is formed by adjusting the gate voltage of the electrode P to deplete the excess electrons.

Therefore, the quantum-dot electron spin qubits in isotopically purified silicon (^{28}Si) is indeed a promising candidate for realizing quantum computation. However, the infidelity of the two-qubit C-phase gate [72], primarily due to the electrical noise, is still higher than the error threshold of surface codes. We aim to construct high-fidelity and robust

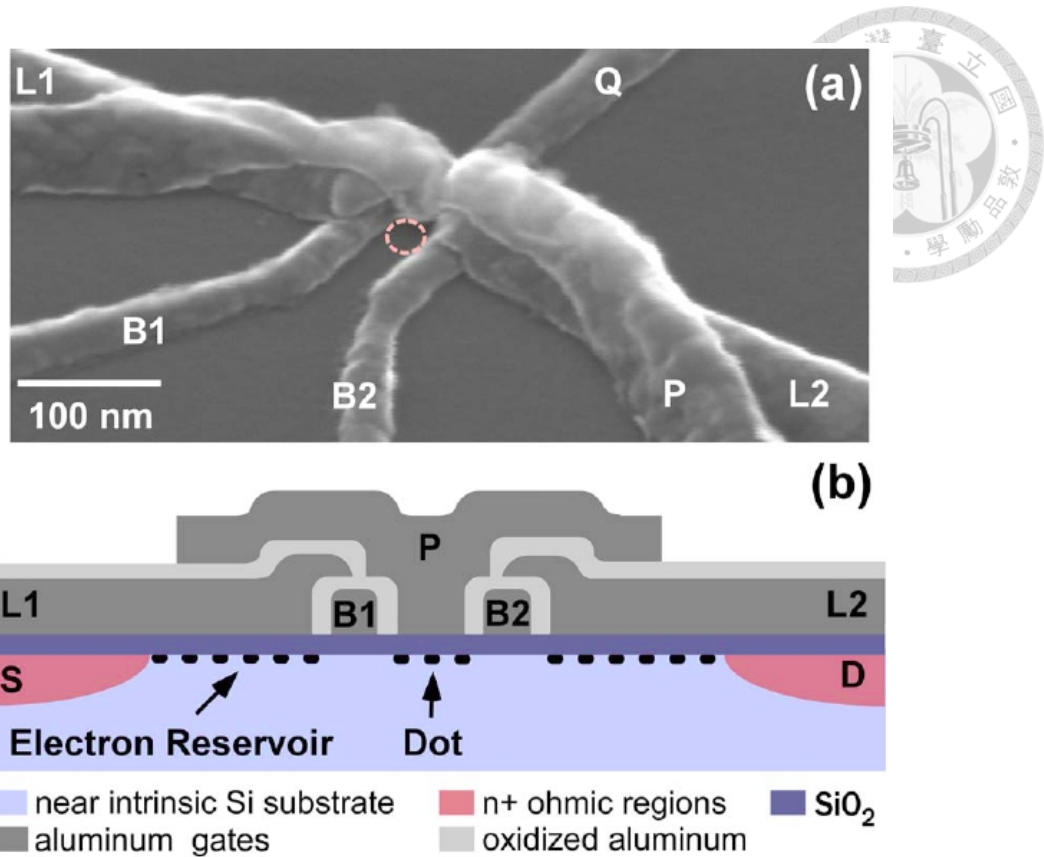


Figure 3.3.: Quantum dots in silicon (courtesy of W. H. Lim et al., 2009).

CNOT gates for this system using our robust control method described in Chapter 2. The architecture of this two-qubit system is shown in Figures 3.4 [72]. The two qubits are defined underneath the electrodes G_1 and G_2 . The tunnel coupling between two dots is a fixed constant after fabrication and thus can't be controlled. For the system, there are only two control channels: the first is the AC magnetic field on both qubits via on-chip electron spin resonance (ESR) line and the second is the detuning energy via the gate voltage of the electrode G_1 or G_2 . In the following sections, we use this architecture of quantum-dot electron spin qubits in isotopically purified silicon [72] to describe the simulation skills for the ideal system, then to analyze the electrical noise and other factors degrading the gate fidelity in the realistic system, and finally to implement our robust control method to demonstrate optimal CNOT gates and single-qubit gates.

3.2. Ideal system

For quantum-dot electron spin qubit in isotopically purified silicon, the ideal two-qubit Hamiltonian written in the basis states of $(|\text{dot}2, \text{dot}1\rangle =) |\uparrow, \uparrow\rangle, |\uparrow, \downarrow\rangle, |\downarrow, \uparrow\rangle, |\downarrow, \downarrow\rangle$ and

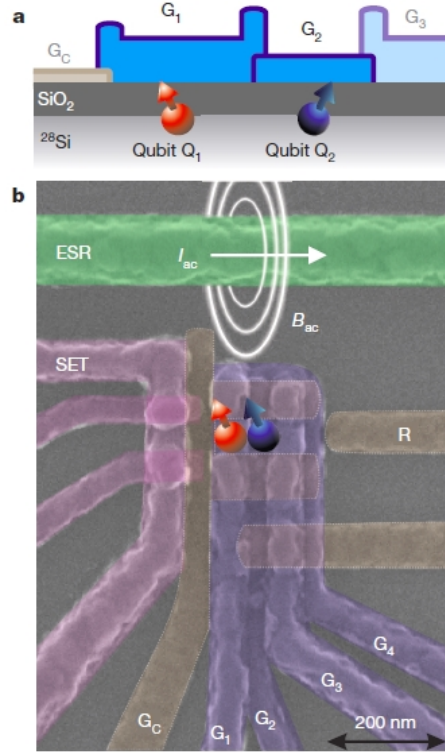


Figure 3.4.: Architecture of the quantum-dot electron spin qubits in isotopically purified silicon (courtesy of M. Veldhorst et al., 2015).

$|0, 2\rangle$ can be expressed as

$$\mathcal{H}_I(t) = h \begin{pmatrix} \bar{E}_Z & \frac{1}{2}E_X(t) & \frac{1}{2}E_X(t) & 0 & 0 \\ \frac{1}{2}E_X(t) & \frac{1}{2}\delta E_Z & 0 & \frac{1}{2}E_X(t) & t_0 \\ \frac{1}{2}E_X(t) & 0 & -\frac{1}{2}\delta E_Z & \frac{1}{2}E_X(t) & -t_0 \\ 0 & \frac{1}{2}E_X(t) & \frac{1}{2}E_X(t) & -\bar{E}_Z & 0 \\ 0 & t_0 & -t_0 & 0 & U - \epsilon \end{pmatrix}, \quad (3.1)$$

where h is the Plank constant, $\bar{E}_Z = (E_{Z_1} + E_{Z_2})/2$ is the average frequency and $\delta E_Z = (E_{Z_2} - E_{Z_1})$ is the frequency difference in Zeeman splitting between the two dots with E_{Z_1} and E_{Z_2} the Zeeman splitting frequencies in the z -direction for dot1 and dot2, respectively, t_0 is the interdot tunnel coupling and hU is the on-site Coulomb energy, and $h\epsilon$ is the detuning energy or relative alignment of the potential of the two dots.

$$E_X(t) = g\mu_B B_X(t)/h = \frac{g\mu_B}{h} \left(\Omega_X(t) \cos(\bar{E}_Z 2\pi t) + \Omega_Y(t) \cos(\bar{E}_Z 2\pi t + \frac{\pi}{2}) \right), \quad (3.2)$$

is the Zeeman splitting frequency in the x -direction for both two dots. We control an AC magnetic field $B_X(t)$ via on-chip ESR line with amplitudes $\Omega_X(t)$ and $\Omega_Y(t)$ to operate quantum gates.

The realistic values of the system parameters for realizing C-phase gates in experiment [72] are $\bar{E}_Z = 39.16\text{GHz}$, $\delta E_Z = -40\text{MHz}$, and $t_0 = 900\text{MHz}$. Substitute these values and $E_X(t) = 0$ into the ideal Hamiltonian \mathcal{H}_I in Eq. (3.1), we can evaluate the energy levels $\lambda_{|\uparrow\uparrow\rangle}$, $\lambda_{|\uparrow\downarrow\rangle}$, $\lambda_{|\downarrow\uparrow\rangle}$, $\lambda_{|\downarrow\downarrow\rangle}$, and $\lambda_{|0,2\rangle}$ of \mathcal{H}_I for states $|\uparrow, \uparrow\rangle$, $|\uparrow, \downarrow\rangle$, $|\downarrow, \uparrow\rangle$, $|\downarrow, \downarrow\rangle$, and $|0, 2\rangle$, respectively. $\lambda_{|\uparrow\uparrow\rangle} = \bar{E}_Z$ and $\lambda_{|\downarrow\downarrow\rangle} = -\bar{E}_Z$, which are independent of ϵ . $\lambda_{|\uparrow\downarrow\rangle}$, $\lambda_{|\downarrow\uparrow\rangle}$, and $\lambda_{|0,2\rangle}$ are function of ϵ . As ϵ increases from zero to a large value ($\epsilon \gg U$), $\lambda_{|\uparrow\downarrow\rangle}$ decreases from $\sim -\frac{1}{2}|\delta E_Z|$ to $\sim (U - \epsilon)$, and $\lambda_{|\downarrow\uparrow\rangle}$ decreases from $\sim \frac{1}{2}|\delta E_Z|$ to $\sim -\frac{1}{2}|\delta E_Z|$. Introduce the effective detuning frequencies

$$\nu_{\uparrow\downarrow} \equiv -\frac{1}{2}|\delta E_Z| - \lambda_{|\uparrow\downarrow\rangle}, \quad (3.3)$$

$$\nu_{\downarrow\uparrow} \equiv +\frac{1}{2}|\delta E_Z| - \lambda_{|\downarrow\uparrow\rangle}. \quad (3.4)$$

For the fast C-phase gate in experiment, $\nu_{\uparrow\downarrow} \sim 3\text{MHz}$, and we can extract the corresponding $(U - \epsilon) \sim 300\text{GHz}$ by our calculation as shown in Figure 3.5. However, these realistic values of the system parameters in the ideal Hamiltonian $\mathcal{H}_I(t)$ in Eq. (3.1) range from 40MHz to 300GHz ($|\delta E_Z| = 40\text{MHz}$, $t_0 = 900\text{MHz}$, $\bar{E}_Z = 39.16\text{GHz}$, and $U - \epsilon = 300\text{GHz}$), and thus a very small time-step for simulation of the system is needed, that is, very long computation time is required. Two approximations can help for this problem. First, for $(U - \epsilon) \gg t_0$ and $(U - \epsilon) \gg |\delta E_Z|$, we can use the Schrieffer-Wolff transformation with approximation [82] to convert $t_0 (= 900\text{MHz})$ into the numerator and $U - \epsilon (= 300\text{GHz})$ into the denominator of a new parameter with a smaller value in the transformed Hamiltonian. Second, for $\bar{E}_Z \gg g\mu_B |\Omega_X(t)| / h$ and $\bar{E}_Z \gg g\mu_B |\Omega_Y(t)| / h$ ($\bar{E}_Z = 39.16\text{GHz}$; the maximum strength of $g\mu_B |\Omega_X(t)| / h$ and $g\mu_B |\Omega_Y(t)| / h$ are $\sim 27.965\text{MHz}$ for the power limitation of the on-chip ESR line), we can use the rotating wave approximation to eliminate the large-value term \bar{E}_Z in the Hamiltonian in the rotating frame.

First, we transform the ideal Hamiltonian $\mathcal{H}_I(t)$ to

$$\tilde{\mathcal{H}}_I^{\text{SW}}(t) = e^S \mathcal{H}_I(t) e^{-S} \quad (3.5)$$

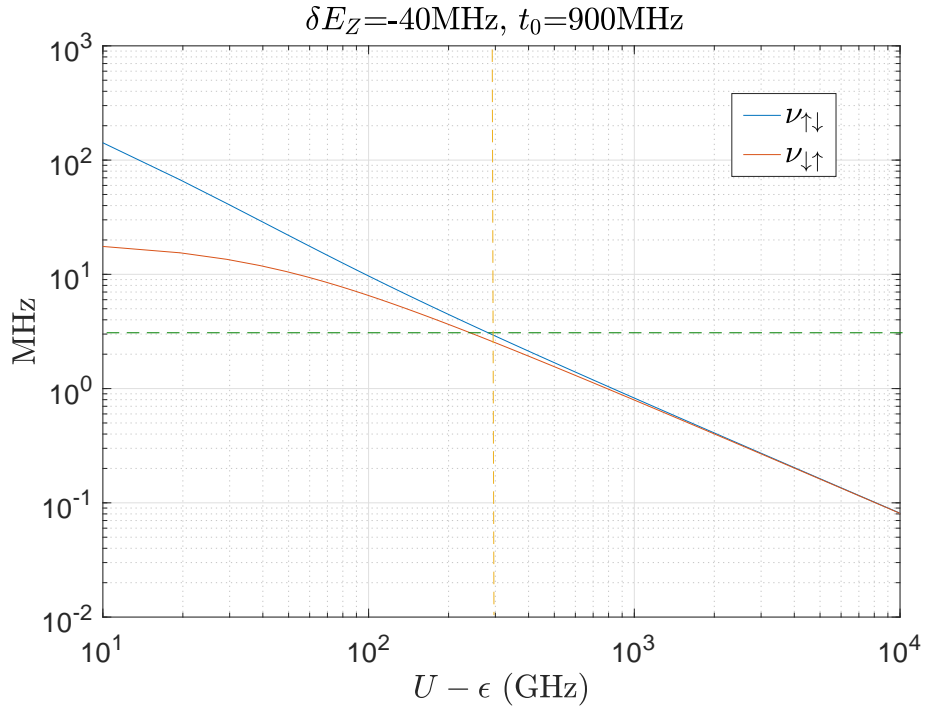


Figure 3.5.: The effective detuning frequencies $\nu_{\uparrow\downarrow}$ and $\nu_{\downarrow\uparrow}$ versus $U - \epsilon$ for $\delta E_Z = -40\text{MHz}$ and $t_0 = 900\text{MHz}$.

by Schrieffer-Wolff transformation (SW) [82], where

$$S = \begin{pmatrix} 0 & 0 & 0 & 0 & 0 \\ 0 & 0 & 0 & 0 & -\gamma(-\delta E_Z) \\ 0 & 0 & 0 & 0 & \gamma(\delta E_Z) \\ 0 & 0 & 0 & 0 & 0 \\ 0 & \gamma(-\delta E_Z) & -\gamma(\delta E_Z) & 0 & 0 \end{pmatrix}, \quad (3.6)$$

and

$$\gamma(\delta E_Z) = \frac{t_0}{U - \epsilon + \delta E_Z/2}. \quad (3.7)$$

For $(U - \epsilon) \gg t_0$ and $(U - \epsilon) \gg |\delta E_Z|$, we can expand $\tilde{\mathcal{H}}_I^{\text{SW}}(t)$ in Eq. (3.5) to the second order of S and omit the terms including $O[\gamma^2(\delta E_Z)]$ or $[\gamma(-\delta E_Z) - \gamma(\delta E_Z)]$ to obtain the Hamiltonian $\tilde{\mathcal{H}}_I^{\text{SWA}}(t)$ (SWA denotes the Hamiltonian is transformed by Schrieffer-Wolff transformation with the above approximations). The estimated error for the above omitted terms is $\sim 10^{-5}$ at most for $t_f = 500\text{ns}$, that is, the infidelity simulation error by $\tilde{\mathcal{H}}_I^{\text{SWA}}(t)$ is $\sim 10^{-5}$. After SWA, the subspace spanned by the computational basis

states $\{|\uparrow, \uparrow\rangle, |\uparrow, \downarrow\rangle, |\downarrow, \uparrow\rangle, |\downarrow, \downarrow\rangle\}$ and the subspace spanned by $|0, 2\rangle$ are decoupled in the Hamiltonian $\tilde{\mathcal{H}}_I^{\text{SWA}}(t)$. Therefore, we can treat the Hamiltonian

$$\tilde{\mathcal{H}}_{I,4\times 4}^{\text{SWA}}(t) = h \begin{pmatrix} \bar{E}_Z & \frac{1}{2}E_X(t) & \frac{1}{2}E_X(t) & 0 \\ \frac{1}{2}E_X(t) & \frac{1}{2}\delta E_Z - J_m & \frac{1}{2}(J_p + J_m) & \frac{1}{2}E_X(t) \\ \frac{1}{2}E_X(t) & \frac{1}{2}(J_p + J_m) & -\frac{1}{2}\delta E_Z - J_m & \frac{1}{2}E_X(t) \\ 0 & \frac{1}{2}E_X(t) & \frac{1}{2}E_X(t) & -\bar{E}_Z \end{pmatrix} \quad (3.8)$$

in the computational basis states $\{|\uparrow, \uparrow\rangle, |\uparrow, \downarrow\rangle, |\downarrow, \uparrow\rangle, |\downarrow, \downarrow\rangle\}$ only, where

$$J_p \equiv \frac{t_0^2}{U - \epsilon + \delta E_Z/2}, \quad (3.9)$$

$$J_m \equiv \frac{t_0^2}{U - \epsilon - \delta E_Z/2}. \quad (3.10)$$

With SWA, the large-value system parameters, $U - \epsilon = 300\text{GHz}$ and $t_0 = 900\text{MHz}$, are transformed into J_p and J_m , and $J_p \approx J_m \cong 2.7\text{MHz}$ is comparable with $\delta E_Z = 40\text{MHz}$. Thus the remaining large-value system parameter in the Hamiltonian $\tilde{\mathcal{H}}_{I,4\times 4}^{\text{SWA}}(t)$ in Eq. (3.8) is $\bar{E}_Z = 39.16\text{GHz}$, and we use the rotating wave approximation to overcome it.

We transform $\tilde{\mathcal{H}}_{I,4\times 4}^{\text{SWA}}(t)$ to the rotating frame (RF) through the transformation formula

$$\tilde{\mathcal{H}}_{I,4\times 4}^{\text{SWA,RF}}(t) = U_0^\dagger(t)\tilde{\mathcal{H}}_{I,4\times 4}^{\text{SWA}}(t)U_0(t) - i\hbar U_0^\dagger(t)\dot{U}_0(t), \quad (3.11)$$

where

$$U_0(t) = \begin{pmatrix} \exp(-i\bar{E}_Z 2\pi t) & 0 & 0 & 0 \\ 0 & 1 & 0 & 0 \\ 0 & 0 & 1 & 0 \\ 0 & 0 & 0 & \exp(+i\bar{E}_Z 2\pi t) \end{pmatrix}. \quad (3.12)$$

In $\tilde{\mathcal{H}}_{I,4\times 4}^{\text{SWA,RF}}(t)$, there exist some terms such as $[g\mu_B\Omega_X(t)/h] \cdot [1 + \exp(\pm i2\bar{E}_Z 2\pi t)]$ and $[g\mu_B\Omega_Y(t)/h] \cdot [1 - \exp(\pm i2\bar{E}_Z 2\pi t)]$, and we can omit the terms $[g\mu_B\Omega_X(t)/h] \exp(\pm i2\bar{E}_Z 2\pi t)$ and $[g\mu_B\Omega_Y(t)/h] \exp(\pm i2\bar{E}_Z 2\pi t)$ for $\bar{E}_Z = 39.16\text{GHz}$ is much larger than the maximum values of $g\mu_B |\Omega_X(t)|/h$ and $g\mu_B |\Omega_Y(t)|/h$ ($\sim 27.965\text{MHz}$, which corresponds 1mT for the maximum strength constraint of $|\Omega_X(t)|$ and $|\Omega_Y(t)|$ due to the power limitation of

the on-chip ESR line). Then we can obtain the Hamiltonian with the rotating wave approximation (RWA),



$$\begin{aligned} & \tilde{\mathcal{H}}_{I,4 \times 4}^{\text{SWA,RWA}}(t) \\ &= h \begin{pmatrix} 0 & \frac{1}{4}\bar{\Omega}_X(t) - i\frac{1}{4}\bar{\Omega}_Y(t) & \frac{1}{4}\bar{\Omega}_X(t) - i\frac{1}{4}\bar{\Omega}_Y(t) & 0 \\ \frac{1}{4}\bar{\Omega}_X(t) + i\frac{1}{4}\bar{\Omega}_Y(t) & \frac{1}{2}\delta E_Z - J_m & \frac{1}{2}(J_p + J_m) & \frac{1}{4}\bar{\Omega}_X(t) - i\frac{1}{4}\bar{\Omega}_Y(t) \\ \frac{1}{4}\bar{\Omega}_X(t) + i\frac{1}{4}\bar{\Omega}_Y(t) & \frac{1}{2}(J_p + J_m) & -\frac{1}{2}\delta E_Z - J_m & \frac{1}{4}\bar{\Omega}_X(t) - i\frac{1}{4}\bar{\Omega}_Y(t) \\ 0 & \frac{1}{4}\bar{\Omega}_X(t) + i\frac{1}{4}\bar{\Omega}_Y(t) & \frac{1}{4}\bar{\Omega}_X(t) + i\frac{1}{4}\bar{\Omega}_Y(t) & 0 \end{pmatrix}, \end{aligned} \quad (3.13)$$

where

$$\bar{\Omega}_X(t) \equiv \frac{g\mu_B}{h}\Omega_X(t), \quad (3.14)$$

$$\bar{\Omega}_Y(t) \equiv \frac{g\mu_B}{h}\Omega_Y(t). \quad (3.15)$$

After SWA and RWA, J_p , J_m , $\bar{\Omega}_X(t)$, $\bar{\Omega}_Y(t)$, and δE_Z in $\tilde{\mathcal{H}}_{I,4 \times 4}^{\text{SWA,RWA}}(t)$ range from 2.7MHz to 40MHz, and thus $\tilde{\mathcal{H}}_{I,4 \times 4}^{\text{SWA,RWA}}(t)$ is good for simulation.

We solve the Schrödinger equation, $i\hbar \frac{d}{dt} \tilde{U}_{I,4 \times 4}^{\text{SWA,RWA}}(t) = \tilde{\mathcal{H}}_{I,4 \times 4}^{\text{SWA,RWA}}(t) \tilde{U}_{I,4 \times 4}^{\text{SWA,RWA}}(t)$, to obtain the propagator $\tilde{U}_{I,4 \times 4}^{\text{SWA,RWA}}(t)$, and transform this propagator from the rotating frame back to the Schrieffer-Wolff transformed frame by the formula

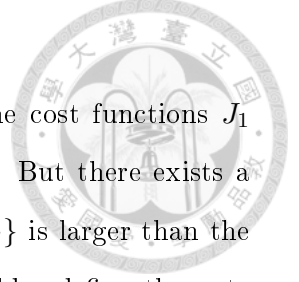
$$\tilde{U}_{I,4 \times 4}^{\text{SWA}}(t) = U_0(t) \tilde{U}_{I,4 \times 4}^{\text{SWA,RWA}}(t). \quad (3.16)$$

In the Schrieffer-Wolff transformed frame, we combine the dynamics in the subspace $|0, 2\rangle$ and $U_{I,4 \times 4}^{\text{SWA}}(t)$ in the subspace of the computational basis states to obtain the propagator in the full space

$$\tilde{U}_I^{\text{SWA}}(t) = \begin{pmatrix} \tilde{U}_{I,4 \times 4}^{\text{SWA}}(t) & 0 \\ 0 & \exp(-i\{U - \epsilon + t_0[\gamma(-\delta E_Z) + \gamma(\delta E_Z)]\}2\pi t) \end{pmatrix}. \quad (3.17)$$

Finally, the ideal system propagator in the original frame, $U_I(t)$, is obtained via the transformation

$$U_I(t) \cong e^{-S} \tilde{U}_I^{\text{SWA}}(t) e^{+S}, \quad (3.18)$$



where we expand e^{-S} and e^{+S} to the second order of S .

With the ideal system propagator $U_I(t)$, we can then evaluate the cost functions J_1 and $\langle J_2 \rangle$ for two-step optimization to find the robust control pulses. But there exists a problem, that is, the simulation space $\{|\uparrow, \uparrow\rangle, |\uparrow, \downarrow\rangle, |\downarrow, \uparrow\rangle, |\downarrow, \downarrow\rangle, |0, 2\rangle\}$ is larger than the computational space $\{|\uparrow, \uparrow\rangle, |\uparrow, \downarrow\rangle, |\downarrow, \uparrow\rangle, |\downarrow, \downarrow\rangle\}$. Therefore, we should redefine the gate infidelity as

$$\mathcal{I} \equiv 1 - \frac{1}{16} \left| \text{Tr} \left[U_T^\dagger U_{4 \times 4}(t_f) \right] \right|^2. \quad (3.19)$$

Here U_T is the two-qubit target gate, and $U_{4 \times 4}(t_f)$ is the propagator in the subspace spanned by the two-qubit computational basis states $\{|\uparrow, \uparrow\rangle, |\uparrow, \downarrow\rangle, |\downarrow, \uparrow\rangle, |\downarrow, \downarrow\rangle\}$, projected from the propagator $U(t_f)$ of the total Hamiltonian at the final gate operation time t_f . For the new definition of \mathcal{I} in Eq. (3.19), we should do some corresponding modifications for J_1 and $\langle J_2 \rangle$. The modified

$$J_1 = 1 - \frac{1}{16} \left| \text{Tr} \left(U_T^\dagger U_{I,4 \times 4}(t_f) \right) \right|^2, \quad (3.20)$$

where $U_{I,4 \times 4}(t_f)$ is the projected propagator in the subspace of the computational basis states from the ideal system propagator $U_I(t_f)$. For the modified J_1 definition in Eq. (3.20), the leakage error, i.e., the state probability remains in the $|0, 2\rangle$ subspace, is also accounted for. And the modified

$$\begin{aligned} \langle J_2 \rangle &= \sum_{j,k} \int_0^{t_f} dt_1 \int_0^{t_1} dt_2 C_{jk}(t_1, t_2) \text{Re}\{\text{Tr}[(R_j(t_1)R_k(t_2))_{4 \times 4}]\} / (2\hbar^2) \\ &\quad - \sum_{j,k} \int_0^{t_f} dt_1 \int_0^{t_1} dt_2 C_{jk}(t_1, t_2) \text{Tr}[R_{j,4 \times 4}(t_1)] \text{Tr}[R_{k,4 \times 4}(t_2)] / (16\hbar^2), \end{aligned} \quad (3.21)$$

where $R_j(t) \equiv U_I^\dagger(t) H_{N_j}(t) U_I(t)$ defined in Eq. (2.7), and $R_{j,4 \times 4}(t)$ and $(R_j(t_1)R_k(t_2))_{4 \times 4}$ are projected in the subspace of the computational basis states from $R_j(t)$ and $R_j(t_1)R_k(t_2)$, respectively. With the modified J_1 in Eq. (3.20), and the modified $\langle J_2 \rangle$ in Eq. (3.21), we are ready to apply our two-step optimization introduced in Sec. 2.2 to construct high-fidelity and robust quantum gates for this system once the noise or the uncertainty are defined clearly.



3.3. Realistic system


In this section, we analyze the dominant factors degrading the gate fidelity in the realistic system of quantum-dot electron spin qubits in isotopically purified silicon, which include the electrical noise $\beta_{U-\epsilon}(t)$, the uncertainty α_{t_0} in tunnel coupling t_0 , and the filtering effects on the control pulses due to the finite bandwidth of waveform generator [83, 84]. Therefore, a more realistic Hamiltonian taking these factors into account becomes

$$\mathcal{H}(t) = h \begin{pmatrix} \bar{E}_Z & \frac{1}{2}E_X^{\text{filt}}(t) & \frac{1}{2}E_X^{\text{filt}}(t) & 0 & 0 \\ \frac{1}{2}E_X^{\text{filt}}(t) & \frac{1}{2}\delta E_Z & 0 & \frac{1}{2}E_X^{\text{filt}}(t) & (t_0 + \alpha_{t_0}) \\ \frac{1}{2}E_X^{\text{filt}}(t) & 0 & -\frac{1}{2}\delta E_Z & \frac{1}{2}E_X^{\text{filt}}(t) & -(t_0 + \alpha_{t_0}) \\ 0 & \frac{1}{2}E_X^{\text{filt}}(t) & \frac{1}{2}E_X^{\text{filt}}(t) & -\bar{E}_Z & 0 \\ 0 & (t_0 + \alpha_{t_0}) & -(t_0 + \alpha_{t_0}) & 0 & U - \epsilon + \beta_{U-\epsilon}(t) \end{pmatrix}, \quad (3.22)$$

$$E_X^{\text{filt}}(t) = \frac{g\mu B}{h} \left(\Omega_X^{\text{filt}}(t) \cos(\bar{E}_Z 2\pi t) + \Omega_Y^{\text{filt}}(t) \cos(\bar{E}_Z 2\pi t + \frac{\pi}{2}) \right), \quad (3.23)$$

where $\Omega_X^{\text{filt}}(t)$ and $\Omega_Y^{\text{filt}}(t)$ are the actual output field amplitudes with the filtering effects accounted for.

To understand the influence of the electrical noise $\beta_{U-\epsilon}(t)$ on the dynamics of the qubits, we simulate the experiment in Section 7 of the Supplementary Information of the paper by Veldhorst et al. [72]. In this experiment, the probability of the state $|\uparrow\downarrow\rangle$, $P(|\uparrow\downarrow\rangle)$, is measured after the operations $(\pi/2)_{X_2} \rightarrow (\pi/2)_{Z_2} \rightarrow \text{C-phase}(\tau_Z) \rightarrow (\pi/2)_{Y_2}$ with initial state $|\downarrow, \downarrow\rangle$ for different τ_Z (gate operation time of C-phase gate). Gates $(\pi/2)_{X_2}$, $(\pi/2)_{Y_2}$, and $(\pi/2)_{Z_2}$ represent $\frac{\pi}{2}$ rotation in X-direction, Y-direction, and Z-direction, respectively, for dot2 qubit, and identity operation for dot1 qubit simultaneously. In experiment, C-phase is realized by tuning ϵ up to a large constant value (small $U - \epsilon$, $U > \epsilon$) for a period time τ_Z , and then tuning ϵ down to a small constant value (large $U - \epsilon$) to turn off the two-qubit coupling. To see the probability oscillation from the two-qubit coupling, the probability in experiment is measured in the rotating frame by



$$U_1(t) = \begin{pmatrix} e^{-i\bar{E}_Z 2\pi t} & 0 & 0 & 0 & 0 \\ 0 & e^{-i\frac{1}{2}\delta E_Z 2\pi t} & 0 & 0 & 0 \\ 0 & 0 & e^{+i\frac{1}{2}\delta E_Z 2\pi t} & 0 & 0 \\ 0 & 0 & 0 & e^{+i\bar{E}_Z 2\pi t} & 0 \\ 0 & 0 & 0 & 0 & 1 \end{pmatrix} \quad (3.24)$$

to eliminate \bar{E}_Z and δE_Z in the Hamiltonian. If there is no electrical noise, this probability

$$P(|\uparrow, \downarrow\rangle) \cong \frac{1}{2} + \frac{1}{2} \cos \left[\left(J_m - \frac{\delta E_Z}{4} \left(\frac{\Omega_J}{\delta E_Z} \right)^2 + \frac{\delta E_Z}{16} \left(\frac{\Omega_J}{\delta E_Z} \right)^4 \right) 2\pi\tau_Z \right], \quad (3.25)$$

$\Omega_J \equiv J_p + J_m$, can be evaluated by the ideal Hamiltonian \mathcal{H}_I in Eq. (3.1) with SWA (Schrieffer-Wolff transformation with approximation in Sec. 3.2). For the realistic case (taking the electrical noise $\beta_{U-\epsilon}(t)$ into consideration), we use the realistic Hamiltonian in Eq. (3.22) with $E_X^{\text{filt}}(t) = 0$, $\alpha_{t_0} = 0$, $\bar{E}_Z = 39.16\text{GHz}$, $\delta E_Z = -40\text{MHz}$, $t_0 = 900\text{MHz}$, and $U - \epsilon = 300\text{GHz}$, and the electrical noise $\beta_{U-\epsilon}(t)$, chosen as a static and stochastic noise model (i.e., the noise strength is a time-independent constant value in each single run of experiment but this constant value can stochastically vary for different runs) with noise strengths obeying a normal distribution with standard deviation $\sigma_{U-\epsilon}$ and mean value $\mu_{U-\epsilon}$ to simulate the C-phase gate suffering the electrical noise effect. We assume $(\pi/2)_{X_2}$, $(\pi/2)_{Z_2}$, and $(\pi/2)_{Y_2}$ are all ideal gates. The ensemble average probability (1000 different $\beta_{U-\epsilon}(t)$ noise realizations), $\langle P(|\uparrow\downarrow\rangle) \rangle$, is calculated for $\sigma = 0, 3, 10\text{GHz}$ (mean value $\mu_{U-\epsilon} = 0$) in Figure 3.6. One observes that $\langle P(|\uparrow\downarrow\rangle) \rangle$ simulation with $\sigma_{U-\epsilon} = 3\text{GHz}$ is very close to the experiment in FIG. S6 in Section 7 of the Supplementary Information [72] as shown in Figure 3.7. Therefore, we assume the electrical noise $\beta_{U-\epsilon}(t)$ is static and stochastic with standard deviation $\sigma_{U-\epsilon} = 3\text{GHz}$ for the rest of quantum gate operation simulations.

In experiment, the interdot tunnel coupling t_0 is obtained by fitting the experimental data with the simulation by the ideal Hamiltonian in Eq. (3.1). Therefore, there may exist some uncertainty value α_{t_0} for t_0 extraction. We regard α_{t_0} as a systematic error, that is α_{t_0} is a fixed constant value for a specific two-qubit system, but the fixed constant α_{t_0} can vary for different two-qubit systems. For ideal system, $U - \epsilon$ and t_0 are converted

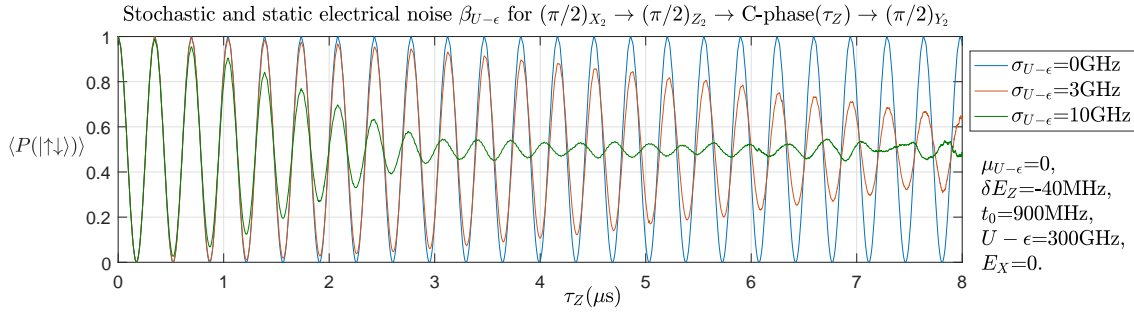


Figure 3.6.: Ensemble average probability $\langle P(|\uparrow\downarrow\rangle)$ simulation for stochastic and static electrical noise $\beta_{U-\epsilon}$ with mean value $\mu_{U-\epsilon} = 0$ and with standard deviation $\sigma_{U-\epsilon} = 0, 3, 10\text{GHz}$.

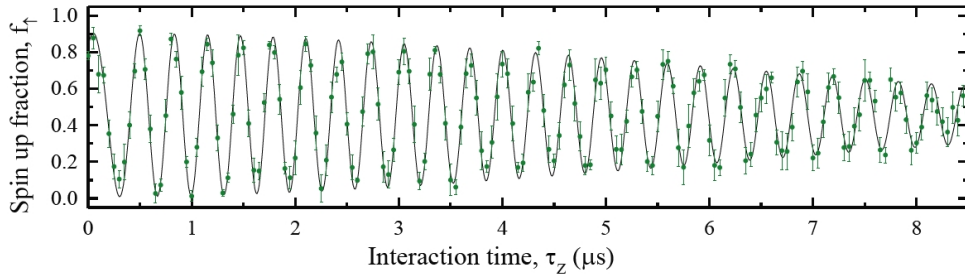


Figure 3.7.: The experimentally measured $\langle P(|\uparrow\downarrow\rangle)$ (courtesy of Veldhorst et al., 2015).

to J_p and J_m ($J_p \approx J_m \cong \frac{t_0^2}{U-\epsilon}$) in $\tilde{\mathcal{H}}_{I,4 \times 4}^{\text{SWA}}(t)$ in Eq. (3.8) by SWA. For the realistic system, the uncertainty α_{t_0} and the electrical noise $\beta_{U-\epsilon}$ are accompanied by t_0 and $U-\epsilon$, respectively, into J_p and J_m in $\tilde{\mathcal{H}}_{I,4 \times 4}^{\text{SWA}}(t)$ as the form $J_p \approx J_m \cong \frac{(t_0 + \alpha_{t_0})^2}{U-\epsilon + \beta_{U-\epsilon}}$. Assume α_{t_0} and $\beta_{U-\epsilon}$ are small fluctuations compared with t_0 and $U-\epsilon$, respectively, and then $J_p \approx J_m \cong \frac{t_0^2}{U-\epsilon} + \frac{2t_0}{U-\epsilon}\alpha_{t_0} - \frac{t_0^2}{(U-\epsilon)^2}\beta_{U-\epsilon}$. So $\frac{2t_0}{U-\epsilon}\alpha_{t_0}$ and $-\frac{t_0^2}{(U-\epsilon)^2}\beta_{U-\epsilon}$ are the corresponding uncertainty and noise contributions in the Hamiltonian, and the most important is that both uncertainty and noise contributions appear in the same locations of the Hamiltonian $\tilde{\mathcal{H}}_{I,4 \times 4}^{\text{SWA}}(t)$. Therefore, once the static electrical noise $\beta_{U-\epsilon}$ is suppressed, and the uncertainty error α_{t_0} is also minimized. Next, we simulate J_{2,t_0} versus $\langle J_{2,U-\epsilon} \rangle$, the lowest-order contribution to the ensemble average infidelity $\langle \mathcal{I} \rangle$ for the systematic error α_{t_0} and the stochastic and static noise $\beta_{U-\epsilon}$, respectively, from an ensemble of J_1 optimized control parameter sets of the CNOT gate ($\overline{E}_Z = 39.16\text{GHz}$, $\delta E_Z = -40\text{MHz}$, $t_0 = 900\text{MHz}$, $U-\epsilon = 300\text{GHz}$, and $t_f = 500\text{ns}$) as shown in Figure 3.8. One can see that as $\langle J_{2,U-\epsilon} \rangle$ decreases J_{2,t_0} also decreases with a constant ratio. By estimation, this ratio

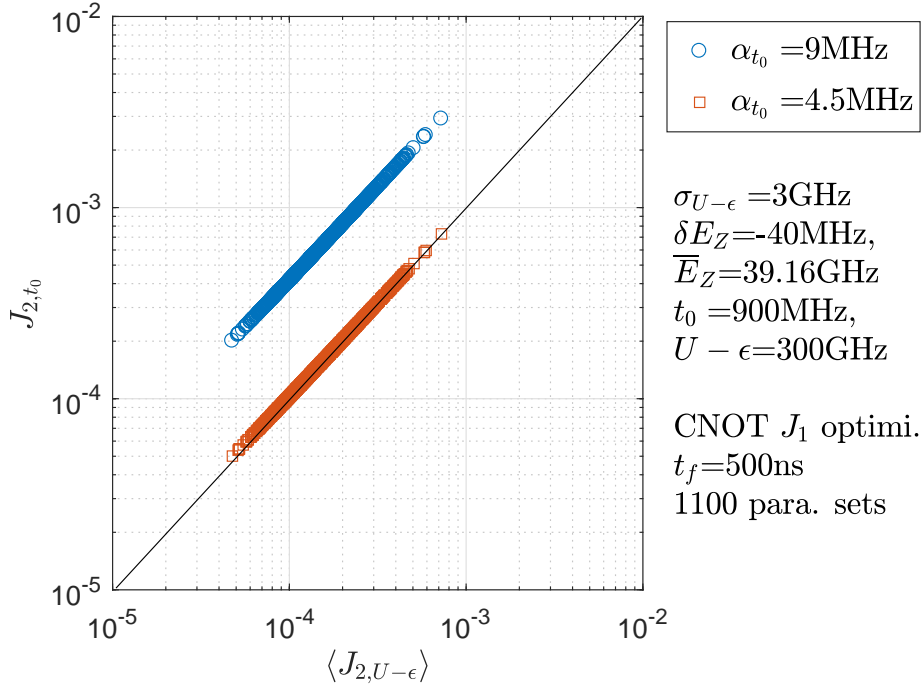


Figure 3.8.: J_{2,t_0} versus $\langle J_{2,U-\epsilon} \rangle$ with $\sigma_{U-\epsilon} = 3\text{GHz}$ for $\alpha_{t_0} = 9\text{MHz}$ and 4.5MHz .

$$\frac{J_{2,t_0}}{\langle J_{2,U-\epsilon} \rangle} \cong \frac{\left[\frac{2t_0}{U-\epsilon} \alpha_{t_0} \cdot t_f \right]^2}{\left[\frac{t_0^2}{(U-\epsilon)^2} \sigma_{U-\epsilon} \cdot t_f \right]^2} = \frac{4(U-\epsilon)^2}{t_0^2} \left(\frac{\alpha_{t_0}}{\sigma_{U-\epsilon}} \right)^2 \quad (3.26)$$

with $\sigma_{U-\epsilon} = 3\text{GHz}$ is ~ 4 and ~ 1 for $\alpha_{t_0} = 9\text{MHz}$ and 4.5MHz , respectively. These estimated ratios are comparable with our simulation in Figures 3.8. Therefore, J_{2,t_0} can be simultaneously minimized when we suppress $\langle J_{2,U-\epsilon} \rangle$ only under the conditions of the realistic values of system parameters and the electrical noise model. In other conditions, J_{2,t_0} may not linearly correlate to $\langle J_{2,U-\epsilon} \rangle$, and we should include both J_{2,t_0} and $\langle J_{2,U-\epsilon} \rangle$ in the cost function $\langle J_2 \rangle$ for optimization.

We choose the form of the control pulses as

$$\Omega_X(t) = \sum_{k=1}^{k_{\max}} a_k \sin^3(\omega_{X,k} \cdot t), \quad (3.27)$$

$$\Omega_Y(t) = \sum_{k=1}^{k_{\max}} b_k \sin^3(\omega_{Y,k} \cdot t), \quad (3.28)$$

to construct the optimal CNOT gates and all optimal single-qubit gates of the system.

Here

$$\omega_{X,k} = \frac{(2k-1)\pi}{t_f}, \quad (3.29)$$

$$\omega_{Y,k} = \frac{(2k)\pi}{t_f}, \quad (3.30)$$



and $\{a_1, a_2, \dots, a_{k_{\max}}\}$ and $\{b_1, b_2, \dots, b_{k_{\max}}\}$ are the control parameter sets for $\Omega_X(t)$ and $\Omega_Y(t)$, respectively. By using the third power of sine function with the oscillation frequency $\omega_{X,k}$ and $\omega_{Y,k}$ in Eq. (3.29) and Eq. (3.30) to compose the pulse, $\Omega_X(t)$ and $\Omega_Y(t)$ have zero pulse strength and zero pulse slope at $t = 0$ and $t = t_f$, which guarantees the smooth pulse-pulse connection of adjacent gates to reduce the extra error from the rise time issue. Besides, for the controllability of the quantum gates of this system, we should choose the symmetric form (symmetric to the middle gate operation time $t_f/2$) for pulse $\Omega_X(t)$ by $\omega_{X,k}$ in Eq. (3.29), and antisymmetric form for pulse $\Omega_Y(t)$ by $\omega_{Y,k}$ in Eq. (3.30). In experiment, there exist some realistic constraints on the control pulses such as the limitation of the maximum pulse strength and the filtering effects. For the power limitation of the on-chip ESR line, the maximum strength of both control pulses $|\Omega_X(t)|$ and $|\Omega_Y(t)|$ is limited by 1mT. This realistic constraint limits the region for searching the optimal control parameter set in the control parameter space $\{a_1, a_2, \dots, a_{k_{\max}}, b_1, b_2, \dots, b_{k_{\max}}\}$, and thus the performance of the optimal gate we find in the limited searching region could not be as good as that in the searching region without any constraints. Next, we discuss the filtering effects. When we input our optimal pulse $\Omega(t)$ (we use $\Omega(t)$ to represents $\Omega_X(t)$ and $\Omega_Y(t)$ pulses) to the instrument of the experiment, we expect the realistic pulse on the qubits is the same as our input. However, due to the finite bandwidth of waveform generators, our input optimal pulse $\Omega(t)$ is altered to the realistic filtered pulse $\Omega^{filt}(t)$ via the transfer function [83, 84]

$$\Omega^{filt}(t) = \frac{1}{2\pi} \int_{-\infty}^{+\infty} dt' \int_{-\infty}^{+\infty} d\omega F(\omega) e^{i(t-t')\omega} \Omega(t'), \quad (3.31)$$

where

$$F(\omega) = \exp(-\omega^2/\omega_0^2) \quad (3.32)$$

is the response function of the filter with ω_0 being the cutoff frequency. The transfer function can be rewritten as



$$\Omega^{\text{filt}}(t) = \frac{1}{2\pi} \int_{-\infty}^{+\infty} d\omega e^{i\omega t} F(\omega) \Omega(\omega), \quad (3.33)$$

where

$$\Omega(\omega) = \int_{-\infty}^{+\infty} dt' e^{-i\omega t'} \Omega(t') \quad (3.34)$$

is the input optimal pulse in the frequency domain. Assume $\Omega(\omega)$ distributes in the frequency region $[-\omega', \omega']$. If ω' is far below the cutoff frequency ω_0 , the response function of the filter $F(\omega)$, defined in Eq. (3.32), in the preset frequency region $[-\omega', \omega']$ approximates to 1, and thus the transfer function in Eq. (3.33) becomes $\Omega^{\text{filt}}(t) \cong \frac{1}{2\pi} \int_{-\omega'}^{+\omega'} d\omega e^{i\omega t} \Omega(\omega)$, just the Fourier transformation of $\Omega(\omega)$, and $\Omega^{\text{filt}}(t) \cong \Omega(t)$. For this case, $F(\omega)$ in the transfer function doesn't work, and thus the filtering effects can be neglected. However, as ω' approaches the cutoff frequency ω_0 , $F(\omega)$ works by nullifying more and more high-frequency distribution of $\Omega(\omega)$ in the transfer function, and thus the filtering effects become more and more apparent. Therefore, in the optimization process, we can not choose $\omega_{X,k}$ and $\omega_{Y,k}$ in the $\Omega_X(t)$ and $\Omega_Y(t)$ as high as we need because $F(\omega)$ will nullify the high frequency component of the pulse, which is in the working region of $F(\omega)$. In Figure 3.9, we show the optimal pulses of CNOT gate with $t_f = 500\text{ns}$ in the frequency domain, $\Omega_X(\omega)$ and $\Omega_Y(\omega)$. One can see that most frequency distribution of $\Omega_X(\omega)$ and $\Omega_Y(\omega)$ is around and below $\sim 20\text{MHz}$ because we choose the number of control parameters $k_{\text{max}} = 11$ for both $\Omega_X(t)$ and $\Omega_Y(t)$, and the maximum $\omega_{X,k_{\text{max}}}/2\pi = 21\text{MHz}$ and $\omega_{Y,k_{\text{max}}}/2\pi = 22\text{MHz}$ by Eq. (3.29) and Eq. (3.30). But there still exist some distribution of $\Omega_X(\omega)$ and $\Omega_Y(\omega)$ in the frequency higher than $\sim 20\text{MHz}$. This is because we choose the third power of sine function to compose the pulse as shown in Eq. (3.27) and Eq. (3.28), and the third power of sine function can be expanded to the first power of sine function, i.e., $\sin^3(\omega_{X,k} \cdot t) = \frac{3}{4} \sin(\omega_{X,k} \cdot t) - \frac{1}{4} \sin(3\omega_{X,k} \cdot t)$, and the contribution of the higher-frequency distribution of $\Omega_X(\omega)$ and $\Omega_Y(\omega)$ just comes from $\sin(3\omega_{X,k} \cdot t)$ and $\sin(3\omega_{Y,k} \cdot t)$, respectively. Next, we show the filtering effects on the optimal pulses of the CNOT gate in Figure 3.9 by the transfer function in Eq. (3.33) with the response function of the filter $F(\omega)$ in Eq. (3.32). We vary the cutoff frequency $\omega_0/2\pi$ from 425.4MHz to 50MHz to see the pulse shift as shown in Figure. 3.10 and the corresponding infidelity J_1 and $\langle J_{2,U-\epsilon} \rangle$ degradation

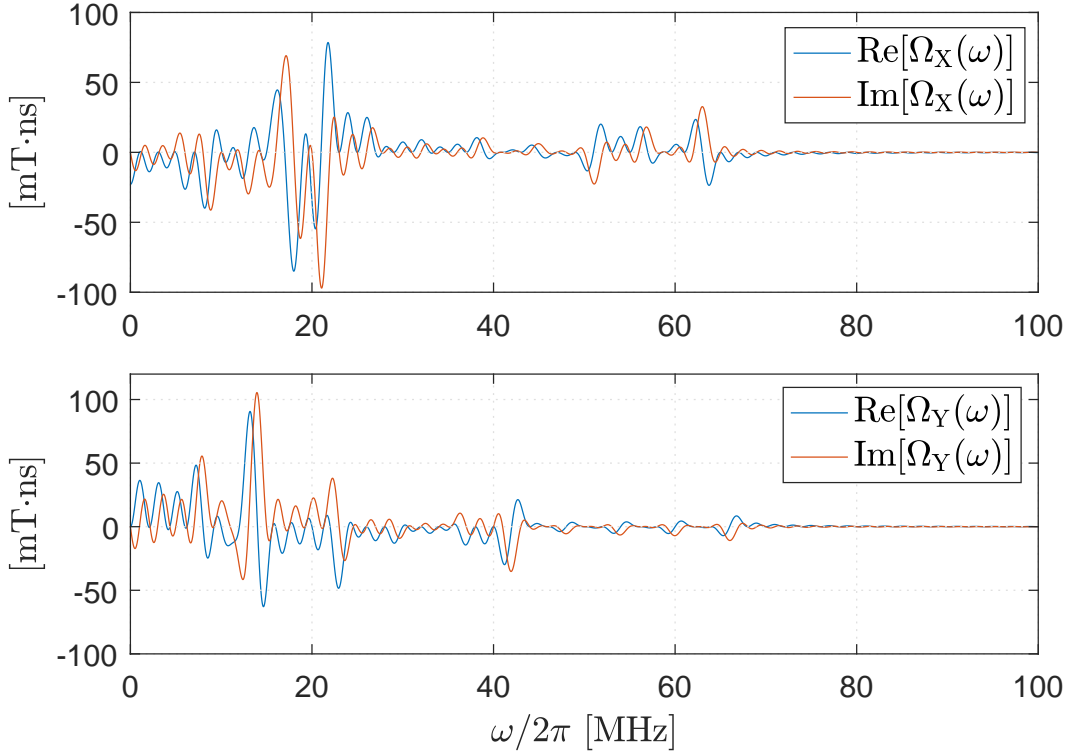


Figure 3.9.: $\Omega_X(\omega)$ and $\Omega_Y(\omega)$ of the optimal CNOT gate with $t_f = 500\text{ns}$.

as shown in Figure 3.11. One can see that as ω_0 decreases the pulse shift is more and more apparent and the corresponding infidelity J_1 is getting worse and worse, but the corresponding $\langle J_{2,U-\epsilon} \rangle$ is not sensitive to ω_0 until $\omega_0/2\pi \leq 100\text{MHz}$, which implies that the $\langle J_{2,U-\epsilon} \rangle$ topography in the control parameter space $\{a_1, a_2, \dots, a_{k_{\max}}, b_1, b_2, \dots, b_{k_{\max}}\}$ around our optimal control parameter set is very flat. Therefore, we can add a fine-tuning optimization (substituting the filtered pulse $\Omega^{\text{filt}}(t)$ into the cost functions) after the two-step optimization introduced in Sec. 2.2 to recover the J_1 degradation and keep $\langle J_{2,U-\epsilon} \rangle$ unchanged. We use the assumption of $\omega_0/2\pi = 425.4\text{MHz}$ (approximation for Tektronix AWG5014 [83]) for simulating the filtering effects on the quantum gates we demonstrate in the following section.

3.4. Demonstration of our control scheme

In the work of Veldhorst et al. [72], $U - \epsilon$ is tuned up to a larger value to turn off the exchange interaction when operating single-qubit gates, and $U - \epsilon$ is tuned down to a smaller value to turn on the exchange interaction when operating two-qubit gates. However, when operating a sequence of single-qubit gates and two-qubit gates, the rise and fall times of

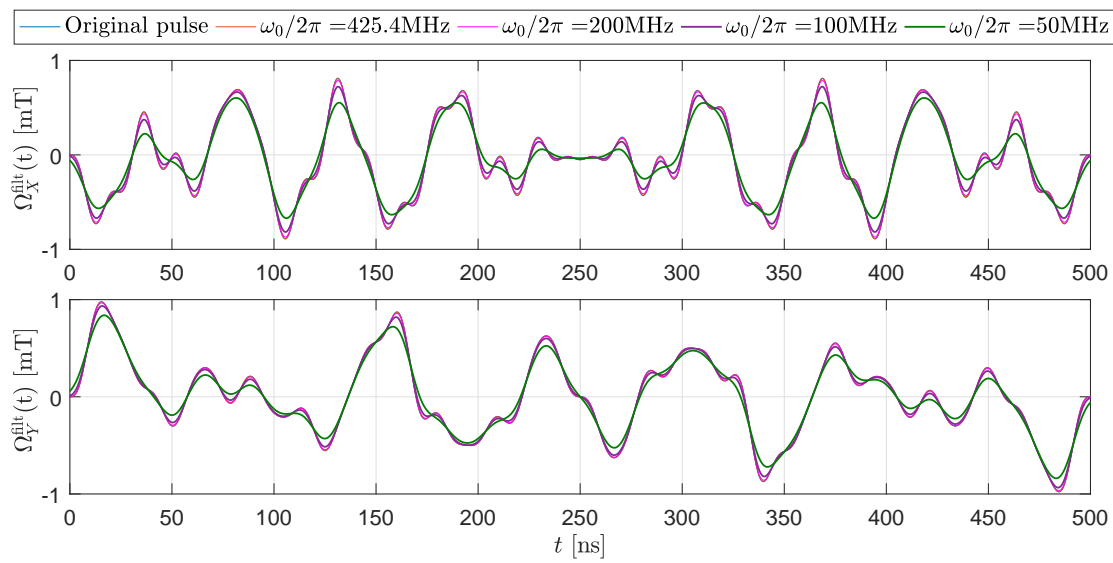
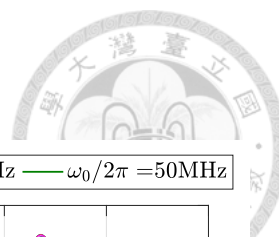


Figure 3.10.: The filtered pulse $\Omega_X^{\text{filt}}(t)$ and $\Omega_Y^{\text{filt}}(t)$ of the optimal CNOT gate by the transfer function with the response function of the filter $F(\omega) = \exp(-\omega^2/\omega_0^2)$.

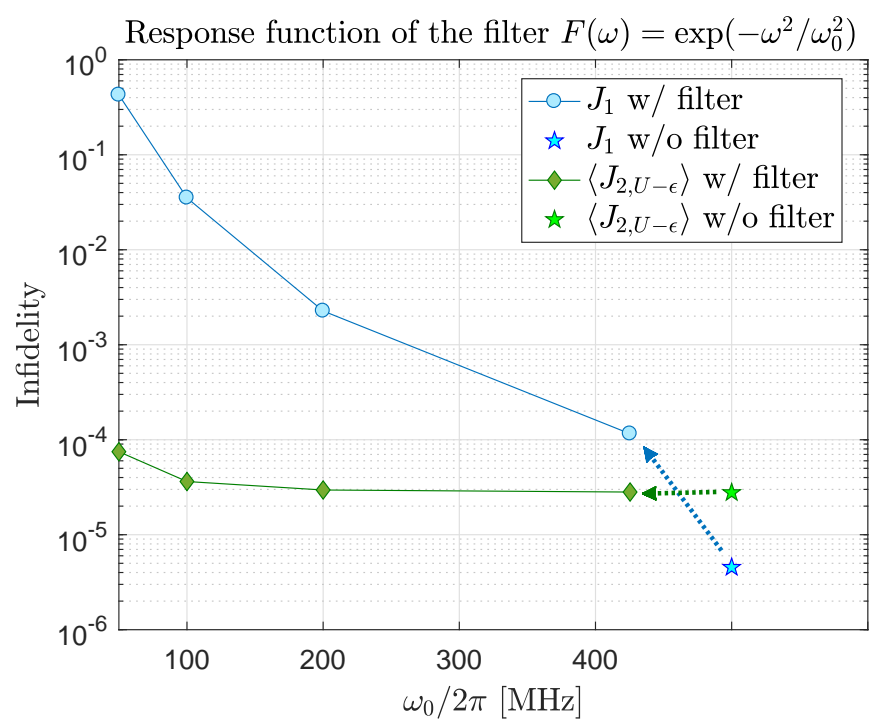


Figure 3.11.: J_1 and $\langle J_{2,U-\epsilon} \rangle$ degradation from the filtering effects.

$U - \epsilon$ between two-qubit gate and single-qubit gates would cause gate errors. Besides, changing $U - \epsilon$ accompanies stark shifts on the quantum-dot qubits, which may results in additional gate errors if the calibration is not precise. Therefore, we propose to keep $U - \epsilon$ as a constant value when operating a sequence of single-qubit and two-qubit gates to prevent the fidelity degradation from tuning $U - \epsilon$ up and down. After finishing a sequence of gate operations, the $U - \epsilon$ can be pulled to a larger value for the idle time. We choose the values of the system parameters as those used to realize C-phase gates experimentally in the work of Veldhorst et al. [72]: $\bar{E}_Z = 39.16\text{GHz}$, $\delta E_Z = -40\text{MHz}$, and $t_0 = 900\text{MHz}$. We keep $U - \epsilon = 300\text{GHz}$ (corresponding $\nu_{\uparrow\downarrow} \cong 3\text{MHz}$ as shown in Figure 3.5 for the fast C-phase gate in the experiment [72]) for gate operations. We control two AC magnetic field amplitudes $\Omega_X(t)$ and $\Omega_Y(t)$ to suppress the electric noise $\beta_{U-\epsilon}(t)$, to enlarge the robust window against the uncertainty α_{t_0} in t_0 , and to recover the gate fidelity deteriorated by the filtering effects, while keeping the maximum values of $|\Omega_X(t)|$ and $|\Omega_Y(t)|$ smaller than 1mT.

We use the ideal Hamiltonian $\mathcal{H}_I(t)$ in Eq. (3.1) with two approximations SWA and RWA to simulate the ideal propagator $U_I(t)$ as described in Sec. 3.2. With $U_I(t)$, we can simulate J_1 in Eq. (3.20). To suppress the gate error contribution from the electrical noise $\beta_{U-\epsilon}(t)$ and the uncertainty α_{t_0} simultaneously, we should define $\langle J_2 \rangle = \langle J_{2,U-\epsilon} \rangle + J_{2,t_0}$, where $\langle J_{2,U-\epsilon} \rangle$ is the lowest order contribution from the electrical noise $\beta_{U-\epsilon}(t)$ and J_{2,t_0} is that from the uncertainty α_{t_0} to the ensemble average infidelity $\langle \mathcal{I} \rangle$. However, as the discussion in Sec. 3.3, J_{2,t_0} and $\langle J_{2,U-\epsilon} \rangle$ are linearly correlated as shown in Figure 3.8, and thus we can suppress $\langle J_{2,U-\epsilon} \rangle$ only, i.e. $\langle J_2 \rangle = \langle J_{2,U-\epsilon} \rangle$, and J_{2,t_0} can also be minimized simultaneously. The definition of the noise Hamiltonian in Eq. (2.5) becomes $\mathcal{H}_N(t) = h\beta_{U-\epsilon}(t)H_{U-\epsilon}(t)$, where

$$H_{U-\epsilon}(t) = \begin{pmatrix} 0 & 0 & 0 & 0 & 0 \\ 0 & 0 & 0 & 0 & 0 \\ 0 & 0 & 0 & 0 & 0 \\ 0 & 0 & 0 & 0 & 0 \\ 0 & 0 & 0 & 0 & 1 \end{pmatrix}. \quad (3.35)$$

By the definition of $\langle J_2 \rangle$ in Eq. (3.21) and the static and stochastic noise model described in Sec. 3.3,



$$\begin{aligned} \langle J_{2,U-\epsilon} \rangle &= \frac{\sigma_{U-\epsilon}^2}{2} \int_0^{t_f} 2\pi dt_1 \int_0^{t_1} 2\pi dt_2 \text{Re}\{\text{Tr}[(R_{U-\epsilon}(t_1)R_{U-\epsilon}(t_2))_{4\times 4}]\} \\ &\quad - \frac{\sigma_{U-\epsilon}^2}{16} \left[\int_0^{t_f} 2\pi dt_1 \text{Tr}(R_{U-\epsilon,4\times 4}(t_1)) \right]^2, \end{aligned} \quad (3.36)$$

where $R_{U-\epsilon}(t) \equiv U_I^\dagger(t)H_{U-\epsilon}(t)U_I(t)$. With J_1 and $\langle J_2 \rangle$, we can apply the two-step optimization introduced in Sec. 2.2 to find the optimal pulses. To recover the J_1 degradation from the filtering effects, we should add an extra fine-tuning optimization after the two-step optimization. The cost function of the fine-tuning optimization is the same as the second step of the two-step optimization, i.e. $J_1 + \langle J_2 \rangle$, but the control pulses $\Omega_X(t)$ and $\Omega_Y(t)$ for simulating $J_1 + \langle J_2 \rangle$ is replaced by the filtered pulses $\Omega_X^{\text{filt}}(t)$ and $\Omega_Y^{\text{filt}}(t)$ via the transfer function in Eq. (3.33) with the response function of the filter $F(\omega)$ in Eq. (3.32) and the cutoff frequency $\omega_0/2\pi = 425.4\text{MHz}$ (approximation for Tektronix AWG5014 [83]). We use the Nelder-Mead (NM) algorithm [76] to search the optimal control parameter sets both in the two-step optimization and the fine-tuning optimization. Finally, we use the realistic Hamiltonian in Eq. (3.22) without extra approximations to simulate the ensemble average infidelity $\langle \mathcal{I} \rangle$ for demonstrating the suppression ability to the electrical noise and the robustness against the uncertainty α_{t_0} of our optimal quantum gates.

3.4.1. CNOT gates

For the CNOT gates, we choose the operation time $t_f = 500\text{ns}$, which is comparable to that of the fastest C-phase gate in the experiment [72]. And we choose the same number of control parameters k_{max} for both control pulses $\Omega_X(t)$ and $\Omega_Y(t)$ in Eq. (3.27) and in Eq. (3.28), and vary $k_{\text{max}} = 7$ to $k_{\text{max}} = 13$ for the J_1 optimization. After the J_1 optimization (100 random initial guesses), we show the optimized J_1 values versus the optimization iterations (NM algorithm) in Figure 3.12. One can see that if k_{max} is too small ($k_{\text{max}} \leq 9$), not all initial guesses can achieve the control parameter sets with the lowest J_1 values after the optimization; if k_{max} is too large ($k_{\text{max}} = 13$), more optimization iterations are needed to achieve the control parameter sets with the lowest J_1 values for some samples. Therefore, we choose $k_{\text{max}} = 11$ for the CNOT gate optimization. However, the lowest J_1 values after the optimization are around 4×10^{-6} and these values can not be improved to arbitrarily small (to the machine limit) even if we increase k_{max} or use smaller time-step

for simulation. To exclude the approximation issue, we also do the J_1 optimization by the ideal Hamiltonian in Eq. (3.1) without two approximations SWA and RWA, and observe the same result as the J_1 optimization with SWA and RWA. Therefore, we think that the controllability with only $\Omega_X(t)$ and $\Omega_Y(t)$ controls is not enough to fully control the system. Even so, J_1 is still over three orders of magnitude smaller than the threshold of surface codes 10^{-2} . Next, we see the distribution of the maximum pulse strength Ω_X^{Max} and Ω_Y^{Max} (the maximum values of $|\Omega_X(t)|$ and $|\Omega_Y(t)|$ within the gate operation time t_f) for the ensemble of J_1 optimized control parameter sets in Figure 3.13, and we observe that only a small portion of the ensemble with $\Omega_X^{\text{Max}} < 1\text{mT}$ and $\Omega_Y^{\text{Max}} < 1\text{mT}$. Therefore, we increase the ensemble size of the J_1 optimization to add more samples, satisfying $\Omega_X^{\text{Max}} < 1\text{mT}$ and $\Omega_Y^{\text{Max}} < 1\text{mT}$, after the optimization. Before implementing the second step of the two-step optimization, we show the corresponding $\langle J_{2,U-\epsilon} \rangle$ in Eq. (3.36) versus the corresponding Ω_X^{Max} and Ω_Y^{Max} for the J_1 optimized ensemble (1100 samples) in Figure. 3.14. One can see that most lower values of $\langle J_{2,U-\epsilon} \rangle$ appear in the region with $\Omega_X^{\text{Max}} > 1\text{mT}$ and $\Omega_Y^{\text{Max}} > 1\text{mT}$, and it implies that stronger pulse strength has benefit for suppressing the electrical noise. However, for the maximum pulse strength constraint in the realistic system, we need to choose the initial guesses for the second step optimization from the J_1 optimized control parameter sets in the region with $\Omega_X^{\text{Max}} < 1\text{mT}$ and $\Omega_Y^{\text{Max}} < 1\text{mT}$ (49 samples).

After the second step optimization, we first filter out the optimized control parameter sets with $\Omega_X^{\text{Max}} \geq 1\text{mT}$ or $\Omega_Y^{\text{Max}} \geq 1\text{mT}$, and then find an optimal control parameter set in the remaining sets with $J_1 = 4.53 \times 10^{-6}$ and $\langle J_{2,U-\epsilon} \rangle = 2.78 \times 10^{-5}$ and with $\Omega_X^{\text{Max}} = 0.89\text{mT}$ and $\Omega_Y^{\text{Max}} = 0.98\text{mT}$. To see the robustness against the uncertainty α_{t_0} for this optimal control parameter set, we simulate the ensemble average infidelity $\langle \mathcal{I} \rangle$ with the realistic Hamiltonian in Eq. (3.22) (standard deviation of the electrical noise $\sigma_{U-\epsilon} = 3\text{GHz}$; the cutoff frequency for filtering effects, $\omega_0/2\pi = 425.4\text{MHz}$) without SWA and RWA as shown in blue circle-line in Figure 3.15. At the point $\alpha_{t_0} = 0$, $J_{2,t_0} = 0$, our predicted ensemble average infidelity should be $\langle \mathcal{I} \rangle \cong J_1 + \langle J_{2,U-\epsilon} \rangle = 4.53 \times 10^{-6} + 2.78 \times 10^{-5} \cong 3 \times 10^{-5}$, but it contradicts with $\langle \mathcal{I} \rangle \cong 10^{-4}$ simulated by the realistic Hamiltonian in Figure 3.15. This is because the filtering effects degrade J_1 from 4.53×10^{-6} to 10^{-4} as shown in Figure 3.11. Therefore, we use the optimal control parameter set after two-step optimization as the initial guess for the fine-tuning optimization. The $\langle \mathcal{I} \rangle$ versus α_{t_0} after the fine-tuning optimization is shown in the red diamond-line in Figure 3.15, and at the point $\alpha_{t_0} = 0$, $\langle \mathcal{I} \rangle$

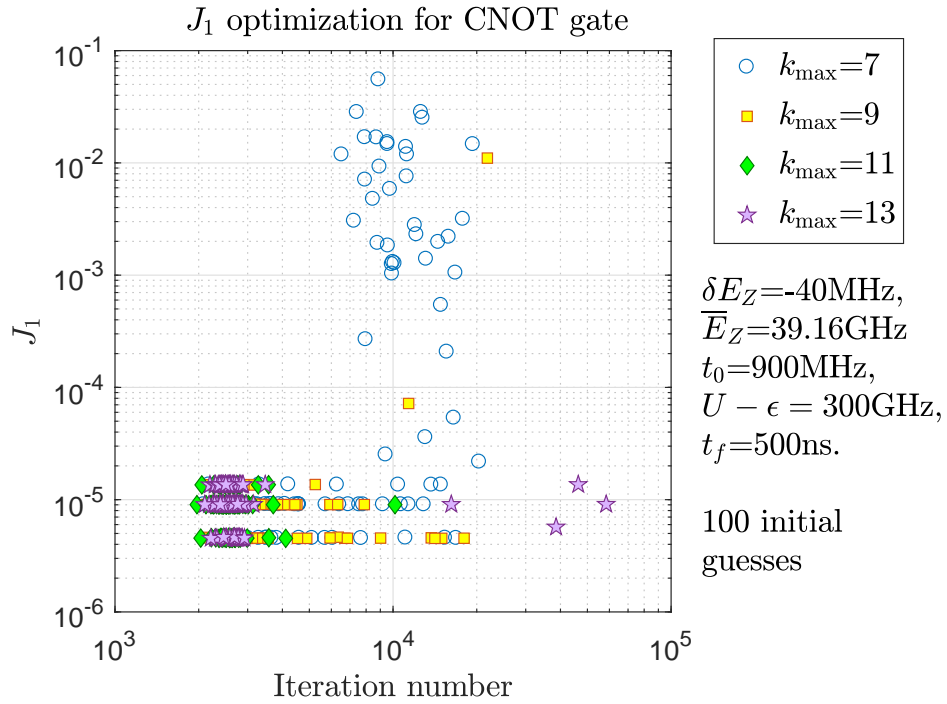
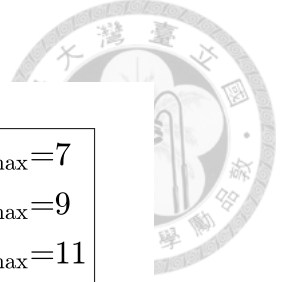


Figure 3.12.: The optimized J_1 values versus optimization iterations after the J_1 optimization for the CNOT gate.

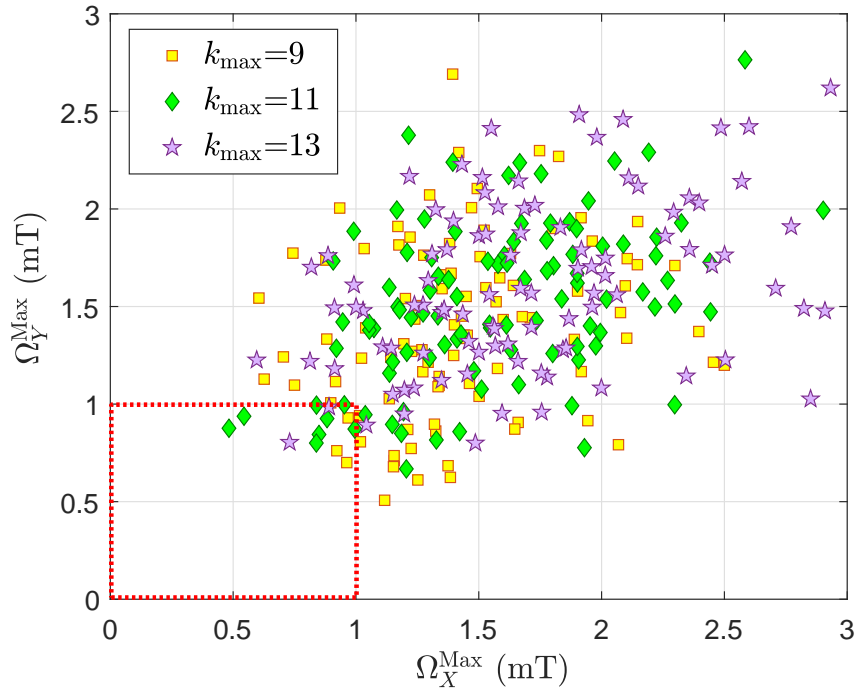


Figure 3.13.: The distribution of the maximum pulse strength Ω_X^{Max} and Ω_Y^{Max} after the J_1 optimization for the CNOT gate.

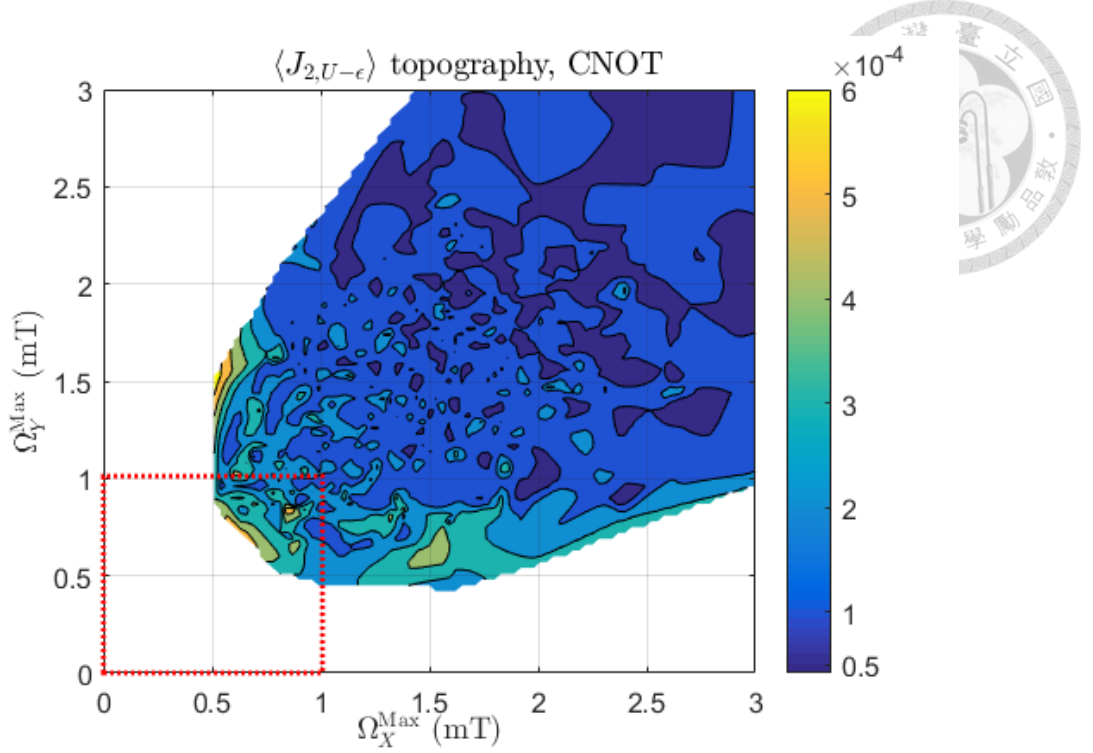


Figure 3.14.: The $\langle J_{2,U-\epsilon} \rangle$ topography of the CNOT gate with $\sigma_{U-\epsilon} = 3\text{GHz}$ versus maximum pulse strength Ω_X^{Max} and Ω_Y^{Max} for the J_1 optimized ensemble (1100 samples).

recovers to our original estimation $\sim 3 \times 10^{-5}$. Besides, one can see that the robustness curves ($\langle \mathcal{I} \rangle$ versus α_{t_0}) after the two-step optimization (blue circle-line) and after the fine-tuning optimization (red diamond-line) coincide for larger α_{t_0} . This is because, for large α_{t_0} , $\langle J_{2,U-\epsilon} \rangle$ and other higher-order noise contributions are larger than J_1 and thus dominate in $\langle \mathcal{I} \rangle$, and $\langle J_{2,U-\epsilon} \rangle$ is not sensitive to the filtering effects as shown in Figure 3.11 and other higher-order noise contributions could also be insensitive to the filtering effects, which results in the overlap of the two curves for large α_{t_0} . After the fine-tuning optimization, we obtain a new optimal control pulse, which can recover the J_1 degradation from the filtering effects, and the pulse shift from the original optimal control pulse after the two-step optimization is $\sim 10^{-3}\text{mT}$ as shown in Figure 3.16.

Next, we compare the performance of our optimal CNOT gates with the maximum pulse strength Ω_X^{Max} and Ω_Y^{Max} smaller than 1mT ($\Omega_{<1\text{mT}}$) and smaller than 1.5mT ($\Omega_{<1.5\text{mT}}$), and the C-phase gate (simulation for the ideal C-phase realized in the experiment [72]) in Figure 3.17. To see the ability to suppress the static and stochastic electrical noise $\beta_{U-\epsilon}$ with standard deviation $\sigma_{U-\epsilon} = 3\text{GHz}$, let us take $\alpha_{t_0} = 0$. At $\alpha_{t_0} = 0$, the ensemble average infidelity $\langle \mathcal{I} \rangle$ of the optimal CNOT gate of $\Omega_{<1\text{mT}}$ (red diamond-line)

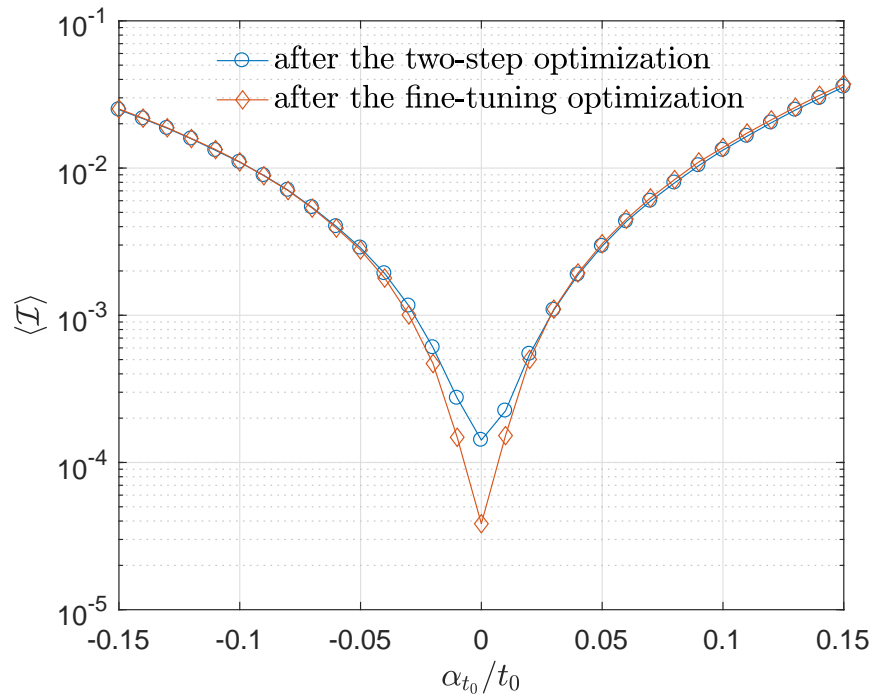
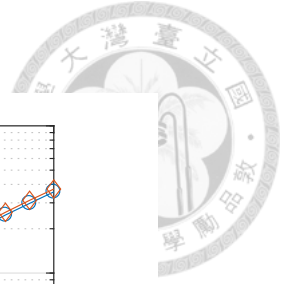


Figure 3.15.: $\langle \mathcal{I} \rangle$ of the CNOT gate versus α_{t_0} after the two-step optimization and after the fine-tuning optimization.

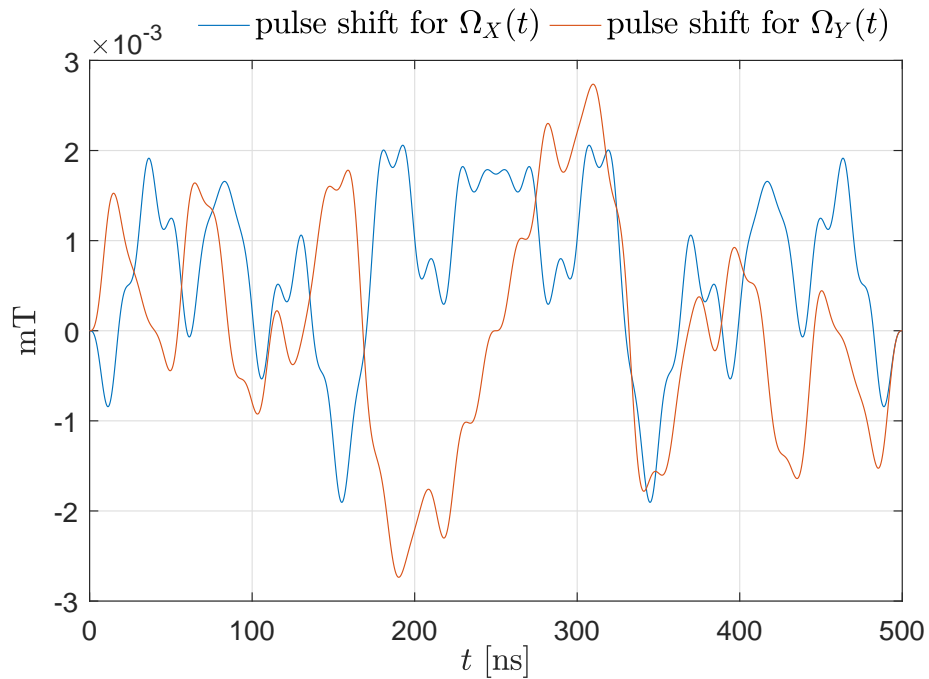


Figure 3.16.: Pulse shift after the fine-tuning optimization for the CNOT gate.

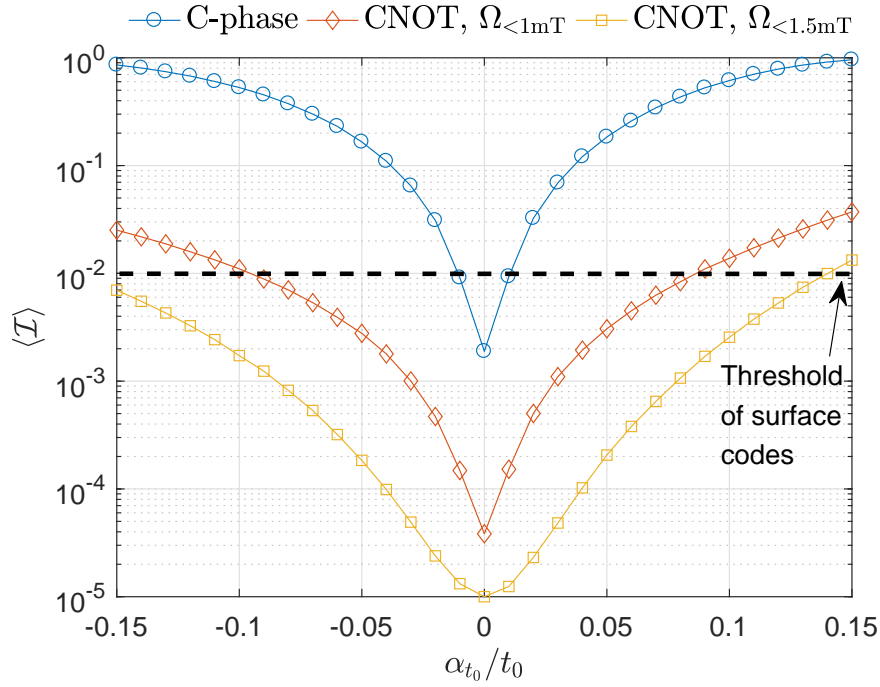


Figure 3.17.: Robust performance against uncertainty α_{t_0} in t_0 for the optimal CNOT gates of $\Omega_{<1\text{mT}}$ (red diamond-line) and $\Omega_{<1.5\text{mT}}$ (yellow square-line), and the C-phase gate (blue circle-line).

is improved near two orders of magnitude compared with that of the C-phase gate (blue circle-line). If the maximum pulse strength Ω_X^{Max} and Ω_Y^{Max} is relaxed to be smaller than 1.5mT ($\Omega_{<1.5\text{mT}}$), $\langle \mathcal{I} \rangle$ of the optimal CNOT gate (yellow square-line) is improved more than two orders of magnitude. For the robust performance against the uncertainty α_{t_0} in t_0 , the C-phase gate (blue circle-line) can be robust only to $\alpha_{t_0}/t_0 \lesssim 1\%$ for the threshold of the surface codes ($\langle \mathcal{I} \rangle \lesssim 10^{-2}$). Our optimal CNOT gate of $\Omega_{<1\text{mT}}$ (red diamond-line) can be robust to $\alpha_{t_0}/t_0 \sim 10\%$, and that of $\Omega_{<1.5\text{mT}}$ (yellow square-line) further robust to $\alpha_{t_0}/t_0 \sim 15\%$. The corresponding optimal pulses after the fine-tuning optimization for the CNOT gate of $\Omega_{<1\text{mT}}$ and the CNOT gate of $\Omega_{<1.5\text{mT}}$ are shown in Figure 3.18.

3.4.2. Single-qubit gates

In this subsection, we demonstrate the performance of two single-qubit gates $I_2 \otimes X_1$ (Identity gate for dot2 qubit and X-gate for dot1 qubit) and $H_2 \otimes I_1$ (Hadamard gate for dot2 qubit and Identity gate for dot1 qubit). We suitably choose the number of control parameters $k_{\text{max}} = 8$ for both $\Omega_X(t)$ and $\Omega_Y(t)$ of these two gates and choose the gate operation time $t_f = 200\text{ns}$ and $t_f = 250\text{ns}$ for $I_2 \otimes X_1$ and $H_2 \otimes I_1$, respectively. The

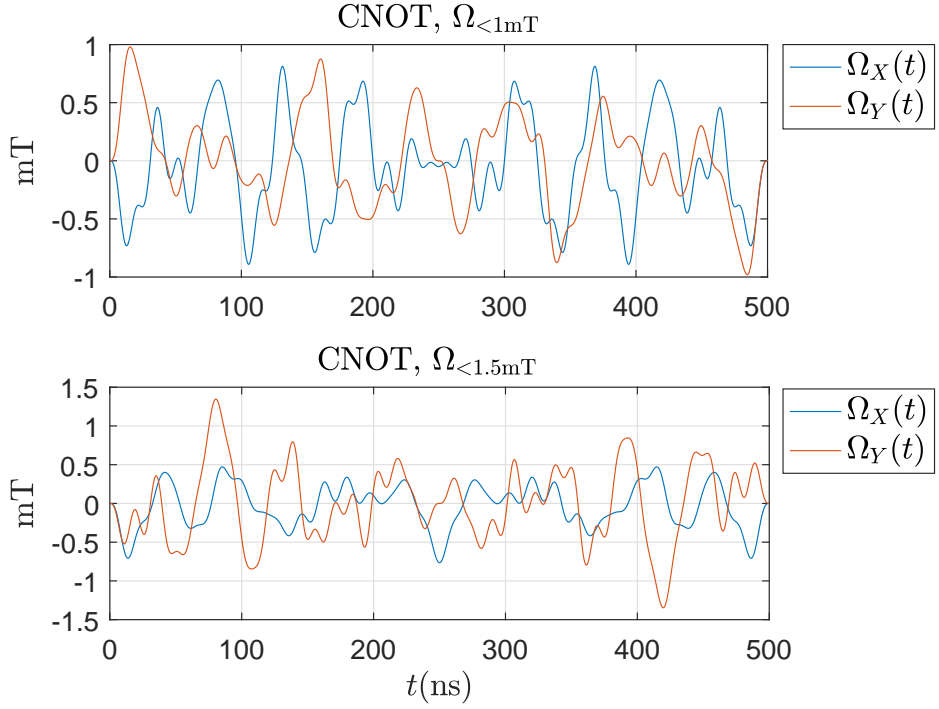


Figure 3.18.: The optimal control pulses of the CNOT gate with $\Omega_{<1\text{mT}}$ and $\Omega_{<1.5\text{mT}}$.

$\langle J_{2,U-\epsilon} \rangle$ topography of $I_2 \otimes X_1$ gate after the J_1 optimization is shown in Figure 3.19, and we compare it with that of the CNOT gate in Figure 3.14. One can see that the height difference in the $\langle J_{2,U-\epsilon} \rangle$ topography of the CNOT gate is only around one order of magnitude, while around two orders of magnitude for $I_2 \otimes X_1$ gate. Furthermore, the lowest $\langle J_{2,U-\epsilon} \rangle$ area (deep blue area) for $I_2 \otimes X_1$ gate is closer to the area with $\Omega_X^{\text{Max}} < 1\text{mT}$ and $\Omega_Y^{\text{Max}} < 1\text{mT}$ than that for the CNOT gate. That is, the $\langle J_{2,U-\epsilon} \rangle$ topography of $I_2 \otimes X_1$ gate around the area $\Omega_X^{\text{Max}} < 1\text{mT}$ and $\Omega_Y^{\text{Max}} < 1\text{mT}$ is more steep than that of the CNOT gate. Therefore, for the second step optimization of $I_2 \otimes X_1$ gate, all initial guesses in the area $\Omega_X^{\text{Max}} < 1\text{mT}$ and $\Omega_Y^{\text{Max}} < 1\text{mT}$ flow into the area $\Omega_{X,\text{max}} > 1\text{mT}$ or $\Omega_{Y,\text{max}} > 1\text{mT}$ more easily than that of the CNOT gate does.

So, we should add an extra cost function, the fluence (a measure of the field energy) [43],

$$\mathcal{F} \equiv \int_0^{t_f} |\Omega_X(t)|^2 dt + \int_0^{t_f} |\Omega_Y(t)|^2 dt \quad (3.37)$$

in the second step optimization and in the fine-tuning optimization to modify the cost function topography in the control parameter space, and the total cost function becomes

$$J_1 + \langle J_{2,U-\epsilon} \rangle + \xi \cdot \mathcal{F}, \quad (3.38)$$

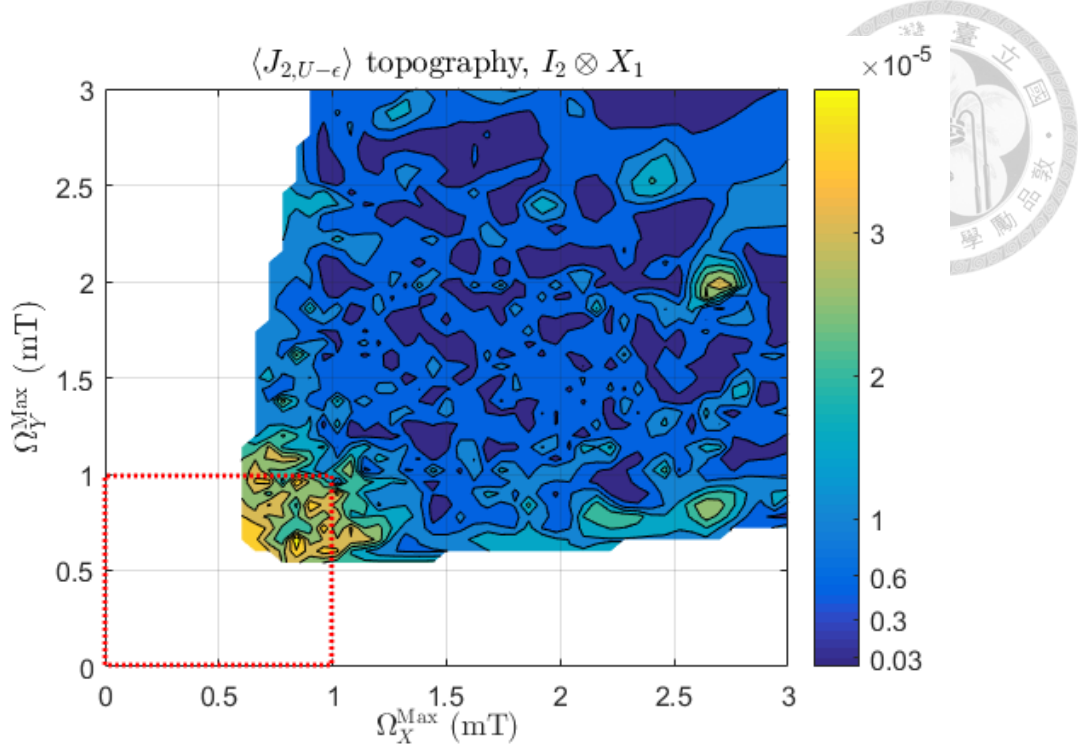


Figure 3.19.: $\langle J_{2,U-\epsilon} \rangle$ topography of $I_2 \otimes X_1$ gate with $\sigma_{U-\epsilon} = 3\text{GHz}$ versus maximum pulse strength Ω_X^{Max} and Ω_Y^{Max} for the J_1 optimized ensemble (2389 samples).

where the constant parameter ξ determines the contribution ratio of the fluence \mathcal{F} in the total cost function. If ξ is too small, \mathcal{F} doesn't work and the steep $\langle J_{2,U-\epsilon} \rangle$ topography still exists, while if ξ is too large, \mathcal{F} dominates all the topography and thus $\langle J_{2,U-\epsilon} \rangle$ can not be suppressed. And we find the optimal $\xi = 10^{-6}$. The performance of the optimal single-qubit $I_2 \otimes X_1$ gate and $H_2 \otimes I_1$ gate is shown in Figure 3.20, and the corresponding optimal pulses after the fine-tuning optimization are shown in Figure 3.21. Both optimal gates can suppress the static and stochastic electrical noise with $\sigma_{U-\epsilon} = 3\text{GHz}$ to $\langle \mathcal{I} \rangle \cong 10^{-5}$ (at $\alpha_{t_0} = 0$), and can be robust to α_{t_0}/t_0 more than 15% for the threshold of surface codes, $\langle \mathcal{I} \rangle \lesssim 10^{-2}$.

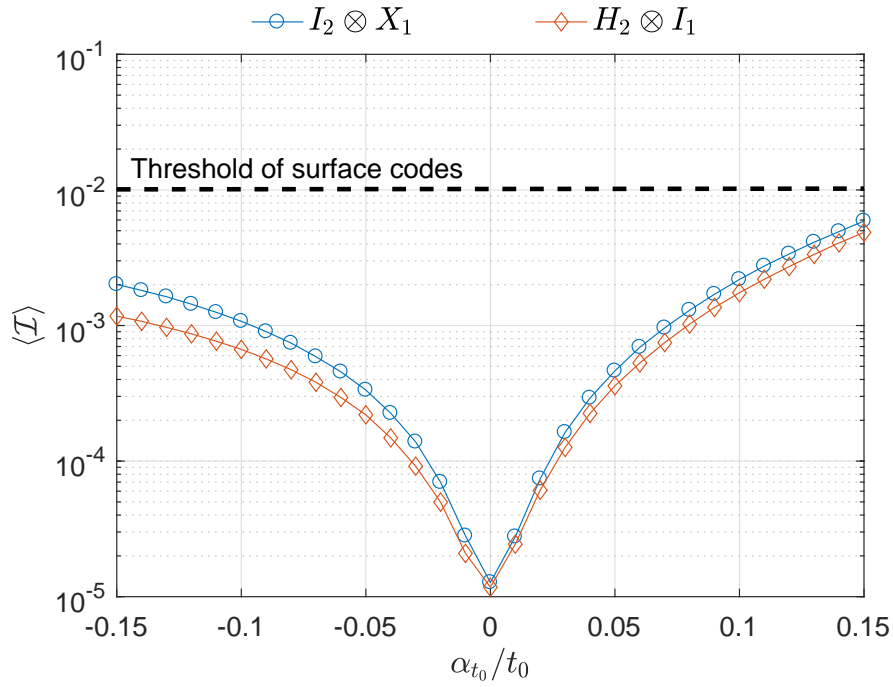
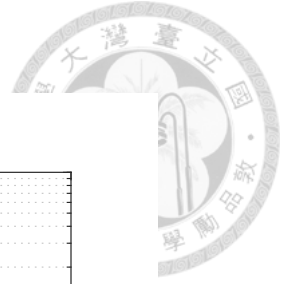


Figure 3.20.: Robust performance against uncertainty α_{t_0} in t_0 for the optimal single-qubit $I_2 \otimes X_1$ gate and $H_2 \otimes I_1$ gate.

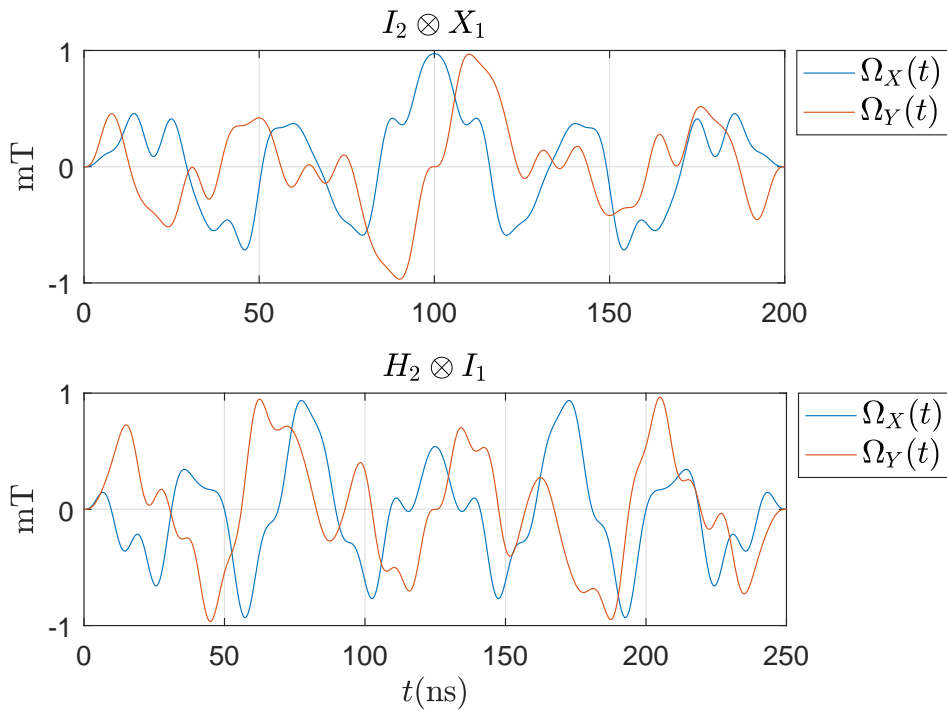


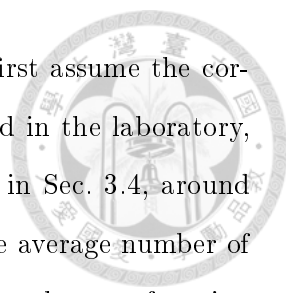
Figure 3.21.: The optimal control pulses of the single-qubit $I_2 \otimes X_1$ gate and $H_2 \otimes I_1$ gate.



4. Conclusion

Our two-step optimization method can provide robust control pulses of high-fidelity quantum gates for stochastic time-varying noise and systematic error. Besides, our method is quite general, and can be applied to different system models, noise models, and noise CFs (PSDs). We apply our robust control method to the realistic system, quantum-dot electron spin qubits in isotopically purified silicon. We use the realistic system parameters from the experiment, characterize the noise model and noise strength from the experiment, and also consider experiment constraints such as the power limitation of the on-chip ESR line and the finite bandwidth of waveform generators, and finally demonstrate the high-fidelity and robust single-qubit gates and CNOT gates for this realistic system by our robust control method. Therefore, our method will make essential steps toward constructing high-fidelity and robust quantum gates for FTQC in realistic quantum computing systems.

When our optimal pulses are applied to the qubits in the laboratory, the gate fidelity could degrade from our prediction for some unknown factors without taking into account in our simulation model. Therefore, some closed-loop optimization methods [85, 86] implemented in the laboratory are suggested to calibrate our optimal pulses for recovering the fidelity degradation from these unknown factors. The cost function for the closed-loop optimization in the laboratory is just the ensemble average infidelity $\langle \mathcal{I} \rangle$ which is obtained via many repetitions of infidelity measurement in the experiment. If the fluctuations of these unknown factors are small, then $\langle \mathcal{I} \rangle \cong J_1 + \langle J_2 \rangle$. If these unknown factors doesn't alter our original $\langle J_2 \rangle$ topography simulation and change only J_1 , the function of the closed-loop optimization in the laboratory corresponds to that of our fine-tuning optimization. If these unknown factors destroy our original $\langle J_2 \rangle$ topography simulation largely, our optimal control parameter set is no longer on the flat bottom of the realistic $\langle J_2 \rangle$ topography. Thus the function of the closed-loop optimization in the laboratory is equivalent to that of our second step of the two-step optimization. To estimate how much time is required



for implementing the closed-loop optimization in the laboratory, we first assume the corresponding fine-tuning optimization via NM algorithm is implemented in the laboratory, and, in the case of our optimal CNOT gate (22 control parameters) in Sec. 3.4, around 1000 optimization iterations are required for NM algorithm, where the average number of cost function calls per each iteration is ~ 3 [87]. So we need to input the cost function to NM algorithm ~ 3000 times, and the cost function in the closed-loop optimization is just the ensemble average infidelity $\langle \mathcal{I} \rangle$. Each $\langle \mathcal{I} \rangle$, obtained by randomized benchmarking [88, 89], can be performed in 2 seconds in the laboratory of the superconducting qubit system [86], and thus we can perform the corresponding fine-tuning optimization of our optimal CNOT gate in the laboratory in ~ 1.7 hours by ~ 3000 $\langle \mathcal{I} \rangle$ measurements. However, the optimization iterations of the second-step optimization is over 500 times as that of the fine-tuning optimization. Therefore, around ~ 35 days are required for the closed-loop optimization in the laboratory when the unknown factors change the original $\langle J_2 \rangle$ topography simulation largely, and in this case we think the practical way is to characterize these unknown factors in experiment, and then input the detailed information of these unknown factors to simulate the precise $\langle J_2 \rangle$ topography for our two-step optimization via classical computers. Another improvement way is to use more efficient optimal algorithms other than NM algorithm to reduce the total number of measurements for the closed-loop optimization in the laboratory [90].

To conclude, the optimal control theory enables us to construct robust and high-fidelity gate pulses against noise and uncertainty in qubit systems. The optimized pulses after closed-loop calibration and optimization in the experiments can implement desired quantum gates with target performance. Several advanced experiments using the optimal control pulses have been demonstrated [86, 91, 92, 93, 94]. Thus the optimal control theory is practical and applicable experimentally and can provide an essential input into the realization of large-scale FTQC.



A. : Derivation of Eqs. (2.12)-(2.14)

We present the derivation of Eqs. (2.12)-(2.14) and discuss the role of the extra term ϵ in Eq. (2.12). Substituting the total system propagator in the Dyson expansion $U(t_f) = U_I(t_f) \cdot (I + \Psi_1 + \Psi_2 + \dots)$ into the infidelity definition \mathcal{I} of Eq. (2.2), we obtain

$$\begin{aligned} \mathcal{I} = & J_1 \\ & - \frac{2}{4^n} \text{Re}\{\text{Tr}[U_T^\dagger U_I(t_f)]^* \cdot \text{Tr}[U_T^\dagger U_I(t_f) \cdot (\Psi_1 + \Psi_2 + \dots)]\} \\ & - \frac{1}{4^n} \left| \text{Tr}[U_T^\dagger U_I(t_f) \cdot (\Psi_1 + \Psi_2 + \dots)] \right|^2. \end{aligned} \quad (\text{A.1})$$

The first term J_1 on the right hand side of Eq. (A.1) is the gate infidelity for the ideal system defined in Eq. (2.13). Then we define the error shift matrix U_ϵ of the ideal propagator $U_I(t_f)$ at time t_f from the target gate U_T up to a global phase ϕ as

$$U_I(t_f) = e^{i\phi} U_T (I + U_\epsilon). \quad (\text{A.2})$$

Note that when the gate infidelity J_1 for the ideal system is made small, the matrix elements of U_ϵ also become small. Substituting the expression of $U_I(t_f)$ of Eq. (A.2) back to Eq. (A.1), we obtain

$$\begin{aligned} \mathcal{I} = & J_1 + \left\{ -\frac{1}{2^{n-1}} \text{Re}[\text{Tr}(\Psi_1)] \right\} \\ & + J_2 + \epsilon(U_\epsilon, \Psi_j) + \mathcal{O}(\tilde{\mathcal{H}}_N^m, m \geq 3), \end{aligned} \quad (\text{A.3})$$



where J_2 is defined in Eq. (2.14),

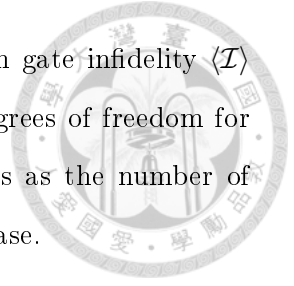
$$\begin{aligned}
\epsilon(U_\epsilon, \Psi_j) = & \\
& - \frac{1}{2^{n-1}} \text{Re}\{\text{Tr}[U_\epsilon(\Psi_1 + \Psi_2 + \dots)]\} \\
& - \frac{2}{4^n} \text{Re}\{\text{Tr}[U_\epsilon]^* \cdot \text{Tr}[\Psi_1 + \Psi_2 + \dots]\} \\
& - \frac{2}{4^n} \text{Re}\{\text{Tr}[U_\epsilon(\Psi_1 + \Psi_2 + \dots)] \cdot \text{Tr}[\Psi_1 + \Psi_2 + \dots]^*\} \\
& - \frac{2}{4^n} \text{Re}\{\text{Tr}[U_\epsilon]^* \cdot \text{Tr}[U_\epsilon(\Psi_1 + \Psi_2 + \dots)]\} \\
& - \frac{1}{4^n} |\text{Tr}[U_\epsilon(\Psi_1 + \Psi_2 + \dots)]|^2, \tag{A.4}
\end{aligned}$$

and $\mathcal{O}(\tilde{\mathcal{H}}_N^m, m \geq 3)$ denotes other higher-order terms without containing U_ϵ . The first-order noise term, $-\text{Re}[\text{Tr}(\Psi_1)]/2^{n-1}$, in Eq. (A.3) actually vanishes for $\text{Tr}(\Psi_1) = -i \int_0^{t_f} \text{Tr}[\mathcal{H}_N(t')] dt'$ is a purely imaginary number, where the noise Hamiltonian $\mathcal{H}_N(t')$ is Hermitian [with $\beta_j(t)$ being real] and thus $\text{Tr}[\mathcal{H}_N(t')]$ is a real number. This result of no first-order noise contribution in \mathcal{I} is similar to that in Ref. [42]. This is also the reason why there is no first-order noise contribution in ensemble average $\langle \mathcal{I} \rangle$ of Eq. (2.15). Equations (2.12)-(2.14) can then be easily obtained from Eq. (A.3) with the identification of $\epsilon = \epsilon(U_\epsilon, \Psi_j)$.

We discuss below the property and the role of $\epsilon = \epsilon(U_\epsilon, \Psi_j)$ in Eq. (2.12) or in Eq. (A.3). The extra contribution $\epsilon = \epsilon(U_\epsilon, \Psi_j)$ to the gate infidelity, with the detailed form shown in Eq. (A.4), is related to the error shift matrix U_ϵ and all Dyson expansion terms Ψ_j . As noted earlier, if J_1 is small, then the matrix elements of U_ϵ are also small. Moreover, if the noise strength is not too strong such that $|\Psi_{j+1}| \ll |\Psi_j|$, then the extra contribution $\epsilon = \epsilon(U_\epsilon, \Psi_j)$ is also small. Therefore when running optimization for a low noise strength, for which the higher-order term $\mathcal{O}(\tilde{\mathcal{H}}_N^m, m \geq 3)$ becomes negligible (see Appendix B), the extra contribution ϵ can be omitted as J_1 is minimized to a small number. Consequently, one can focus on the optimization of only $J_1 + \langle J_2 \rangle$.

The advantage of introducing J_1 and ϵ in our method is to enable more degrees of freedom in control parameters for optimization. There are actually no J_1 and ϵ contributions in the gate infidelity expression of the robust control method of SUPCODE [30, 31] and the filter-transfer-function method [49, 50]. In these methods, J_1 , or, equivalently, the error shift matrix U_ϵ , is set exactly to 0 by imposing some constraints on the control parameters. In contrast, our method can tolerate some error of U_ϵ and thus have more degrees of freedom

in control parameters as long as J_1 and the extra contribution $\langle \epsilon \rangle$ in gate infidelity $\langle \mathcal{I} \rangle$ are made just smaller than $\langle J_2 \rangle$. This advantage of having more degrees of freedom for optimization plays an important role in finding better control pulses as the number of qubits, the number of controls, and the number of noise sources increase.





B. : Estimation of higher-order contributions

Here we estimate the contributions of higher-order terms $\mathcal{O}(\tilde{\mathcal{H}}_N^m, m \geq 3)$ and discuss when they can be neglected. We express the higher-order terms as $\mathcal{O}(\tilde{\mathcal{H}}_N^m, m \geq 3) = \sum_{p \geq 3} J_p$, where J_p denotes the p -th order noise term of the gate infidelity. Detailed forms of the first two lowest-order terms in $\mathcal{O}(\tilde{\mathcal{H}}_N^m, m \geq 3)$ are

$$J_3 = -\frac{1}{2^{n-1}} \text{Re}[\text{Tr}(\Psi_3)] - \frac{2}{4^n} \text{Re}\{\text{Tr}(\Psi_1)\text{Tr}(\Psi_2)^*\}, \quad (\text{B.1})$$

$$J_4 = -\frac{1}{2^{n-1}} \text{Re}[\text{Tr}(\Psi_4)] - \frac{1}{4^n} |\text{Tr}(\Psi_2)|^2 - \frac{2}{4^n} \text{Re}\{\text{Tr}(\Psi_1)\text{Tr}(\Psi_3)^*\}, \quad (\text{B.2})$$

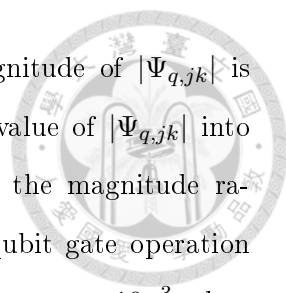
where

$$\Psi_q = (-i)^q \int_0^{t_f} dt_1 \int_0^{t_1} dt_2 \cdots \int_0^{t_{q-1}} dt_q \tilde{\mathcal{H}}_N(t_1) \tilde{\mathcal{H}}_N(t_2) \cdots \tilde{\mathcal{H}}_N(t_q) \quad (\text{B.3})$$

is the q -th order Dyson expansion term. To make an estimation of the magnitude of Ψ_q , we take the Z-noise model for the single-qubit gate operations in Sec. 2.3.1.1 as an example. Substituting the noise Hamiltonian $\tilde{\mathcal{H}}_N(t) = \beta_Z(t)R_Z(t)$ with $R_Z(t) = U_I^\dagger(t)[\omega_0 Z/2]U_I(t)$ in the interaction picture into Ψ_q , we obtain

$$\begin{aligned} \Psi_q &= (-i)^q \int_0^{t_f} \omega_0 dt_1 \int_0^{t_1} \omega_0 dt_2 \cdots \int_0^{t_{q-1}} \omega_0 dt_q \\ &\quad \times \{\beta_Z(t_1)\beta_Z(t_2) \cdots \beta_Z(t_q)\} \{\bar{R}_Z(t_1)\bar{R}_Z(t_2) \cdots \bar{R}_Z(t_q)\}. \end{aligned} \quad (\text{B.4})$$

where $\bar{R}_Z(t) = U_I^\dagger(t)[Z/2]U_I(t)$. Since $U_I(t)$ is unitary, its matrix elements $|U_{I,jk}(t)| \leq 1$ for all j and k . Consequently, $|\bar{R}_{Z,jk}(t)| < 1$ for all j and k , so $|\{\bar{R}_Z(t_1)\bar{R}_Z(t_2) \cdots \bar{R}_Z(t_q)\}_{jk}| < 1$ for all j and k . Taking the strength of $\beta_Z(t)$ to be about its standard deviation σ_{ZZ} , we estimate the noise strength contribution to be $|\{\beta_Z(t_1)\beta_Z(t_2) \cdots \beta_Z(t_q)\}| \approx (\sigma_{ZZ})^q$. The time integral contribution $\{\int_0^{t_f} \omega_0 dt_1 \int_0^{t_1} \omega_0 dt_2 \cdots \int_0^{t_{q-1}} \omega_0 dt_q\}$ can be estimated to be

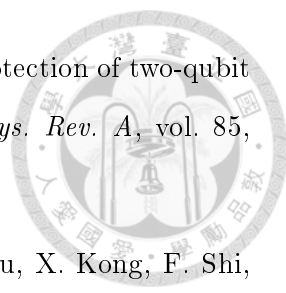


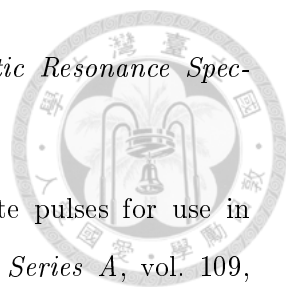
about $\sim (\omega_0 t_f)^q / q!$. By combining the above estimations, the magnitude of $|\Psi_{q,jk}|$ is of the order of $\sim (\omega_0 t_f \sigma_{ZZ})^q / q!$. Then substituting the estimated value of $|\Psi_{q,jk}|$ into J_2 in Eq. (2.14), J_3 in Eq. (B.1), and J_4 in Eq. (B.2), we obtain the magnitude ratio $J_3/J_2 \sim (\omega_0 t_f \sigma_{ZZ})/3$ and $J_4/J_2 \sim (\omega_0 t_f \sigma_{ZZ})^2/12$. The single-qubit gate operation time in Sec. 2.3.1.1 is $\omega_0 t_f = 20$. If we choose the noise fluctuation $\sigma_{ZZ} = 10^{-3}$, then the ratio $J_3/J_2 \sim (6 \times 10^{-3})$ and $J_4/J_2 \sim (3 \times 10^{-5})$, and thus the higher-order terms $\mathcal{O}(\tilde{\mathcal{H}}_N^m, m \geq 3)$ can be safely neglected. If, however, $\sigma_{ZZ} \sim 10^{-1}$, then $\omega_0 t_f \sigma_{ZZ} \sim 2$. In this case, $J_3/J_2 \sim 2/3$ and $J_4/J_2 \sim 1/3$, so the higher-order terms $\mathcal{O}(\tilde{\mathcal{H}}_N^m, m \geq 3)$ can not be neglected. Comparing our estimation with the results of the full-Hamiltonian simulation, one finds that the ensemble average of the gate infidelity $\langle \mathcal{I} \rangle$ of the IDG strategy scales as the second power of σ_{ZZ} (because $\langle J_2 \rangle$ dominates) for small σ_{ZZ} until $\sigma_{ZZ} \sim 10^{-1}$ in Figure 2.3(a) for low-frequency noise $\gamma_{ZZ} = 10^{-7} \omega_0$ and in Figure 2.4(a) for high-frequency noise $\gamma_{ZZ} = 10^{-1} \omega_0$. This is consistent with our estimation. In other words, if σ_{ZZ} is considerably smaller than 10^{-1} , $\mathcal{O}(\tilde{\mathcal{H}}_N^m, m \geq 3)$ can be ignored. Therefore, even in the case where the full-Hamiltonian simulation is not available, we can use this estimation method to determine the criterion for neglecting the higher-order terms $\mathcal{O}(\tilde{\mathcal{H}}_N^m, m \geq 3)$.

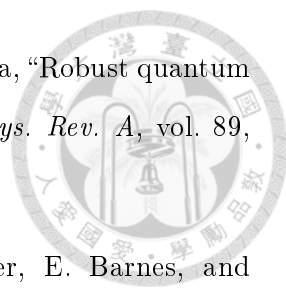


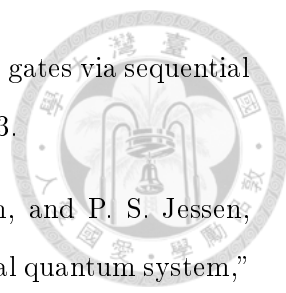
Bibliography

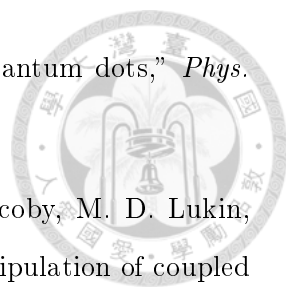
- [1] A. G. Fowler, M. Mariantoni, J. M. Martinis, and A. N. Cleland, "Surface codes: Towards practical large-scale quantum computation," *Phys. Rev. A*, vol. 86, p. 032324, Sep 2012.
- [2] K. Khodjasteh and L. Viola, "Dynamically error-corrected gates for universal quantum computation," *Phys. Rev. Lett.*, vol. 102, p. 080501, Feb 2009.
- [3] K. Khodjasteh and L. Viola, "Dynamical quantum error correction of unitary operations with bounded controls," *Phys. Rev. A*, vol. 80, p. 032314, Sep 2009.
- [4] K. Khodjasteh, D. A. Lidar, and L. Viola, "Arbitrarily accurate dynamical control in open quantum systems," *Phys. Rev. Lett.*, vol. 104, p. 090501, Mar 2010.
- [5] K. Khodjasteh, H. Bluhm, and L. Viola, "Automated synthesis of dynamically corrected quantum gates," *Phys. Rev. A*, vol. 86, p. 042329, Oct 2012.
- [6] J. R. West, D. A. Lidar, B. H. Fong, and M. F. Gyure, "High fidelity quantum gates via dynamical decoupling," *Phys. Rev. Lett.*, vol. 105, p. 230503, Dec 2010.
- [7] A. M. Souza, G. A. Álvarez, and D. Suter, "Experimental protection of quantum gates against decoherence and control errors," *Phys. Rev. A*, vol. 86, p. 050301, Nov 2012.
- [8] F. F. Fanchini, J. E. M. Hornos, and R. d. J. Napolitano, "Continuously decoupling a hadamard quantum gate from independent classes of errors," *Phys. Rev. A*, vol. 76, p. 032319, Sep 2007.
- [9] F. F. Fanchini, R. d. J. Napolitano, B. Çakmak, and A. O. Caldeira, "Protecting the $\sqrt{\text{swap}}$ operation from general and residual errors by continuous dynamical decoupling," *Phys. Rev. A*, vol. 91, p. 042325, Apr 2015.


- 
- [10] A. Z. Chaudhry and J. Gong, “Decoherence control: Universal protection of two-qubit states and two-qubit gates using continuous driving fields,” *Phys. Rev. A*, vol. 85, p. 012315, Jan 2012.
- [11] X. Xu, Z. Wang, C. Duan, P. Huang, P. Wang, Y. Wang, N. Xu, X. Kong, F. Shi, X. Rong, and J. Du, “Coherence-protected quantum gate by continuous dynamical decoupling in diamond,” *Phys. Rev. Lett.*, vol. 109, p. 070502, Aug 2012.
- [12] J. Clausen, G. Bensky, and G. Kurizki, “Bath-optimized minimal-energy protection of quantum operations from decoherence,” *Phys. Rev. Lett.*, vol. 104, p. 040401, Jan 2010.
- [13] J. Clausen, G. Bensky, and G. Kurizki, “Task-optimized control of open quantum systems,” *Phys. Rev. A*, vol. 85, p. 052105, May 2012.
- [14] M. Wenin and W. Pötz, “Minimization of environment-induced decoherence in quantum subsystems and application to solid-state-based quantum gates,” *Phys. Rev. B*, vol. 78, p. 165118, Oct 2008.
- [15] P. Rebentrost, I. Serban, T. Schulte-Herbrüggen, and F. K. Wilhelm, “Optimal control of a qubit coupled to a non-markovian environment,” *Phys. Rev. Lett.*, vol. 102, p. 090401, Mar 2009.
- [16] B. Hwang and H.-S. Goan, “Optimal control for non-markovian open quantum systems,” *Phys. Rev. A*, vol. 85, p. 032321, Mar 2012.
- [17] J.-S. Tai, K.-T. Lin, and H.-S. Goan, “Optimal control of quantum gates in an exactly solvable non-markovian open quantum bit system,” *Phys. Rev. A*, vol. 89, p. 062310, Jun 2014.
- [18] S.-Y. Huang and H.-S. Goan, “Optimal control for fast and high-fidelity quantum gates in coupled superconducting flux qubits,” *Phys. Rev. A*, vol. 90, p. 012318, Jul 2014.
- [19] Y. Chou, S.-Y. Huang, and H.-S. Goan, “Optimal control of fast and high-fidelity quantum gates with electron and nuclear spins of a nitrogen-vacancy center in diamond,” *Phys. Rev. A*, vol. 91, p. 052315, May 2015.
- [20] R. Tycko, “Broadband population inversion,” *Phys. Rev. Lett.*, vol. 51, pp. 775–777, Aug 1983.

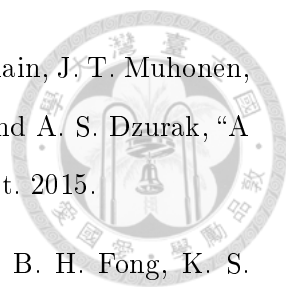
- 
- [21] M. H. Levitt, “Composite pulses,” *Progress in Nuclear Magnetic Resonance Spectroscopy*, vol. 18, no. 2, pp. 61 – 122, 1986.
- [22] S. Wimperis, “Broadband, narrowband, and passband composite pulses for use in advanced NMR experiments,” *Journal of Magnetic Resonance, Series A*, vol. 109, no. 2, pp. 221 – 231, 1994.
- [23] H. K. Cummins, G. Llewellyn, and J. A. Jones, “Tackling systematic errors in quantum logic gates with composite rotations,” *Phys. Rev. A*, vol. 67, p. 042308, Apr 2003.
- [24] K. R. Brown, A. W. Harrow, and I. L. Chuang, “Arbitrarily accurate composite pulse sequences,” *Phys. Rev. A*, vol. 70, p. 052318, Nov 2004.
- [25] L. M. K. Vandersypen and I. L. Chuang, “NMR techniques for quantum control and computation,” *Rev. Mod. Phys.*, vol. 76, pp. 1037–1069, Jan 2005.
- [26] T. Ichikawa, M. Bando, Y. Kondo, and M. Nakahara, “Designing robust unitary gates: Application to concatenated composite pulses,” *Phys. Rev. A*, vol. 84, p. 062311, Dec 2011.
- [27] M. Bando, T. Ichikawa, Y. Kondo, and M. Nakahara, “Concatenated composite pulses compensating simultaneous systematic errors,” *Journal of the Physical Society of Japan*, vol. 82, no. 1, p. 014004, 2013.
- [28] T. Ichikawa, U. Güngördü, M. Bando, Y. Kondo, and M. Nakahara, “Minimal and robust composite two-qubit gates with Ising-type interaction,” *Phys. Rev. A*, vol. 87, p. 022323, Feb 2013.
- [29] J. T. Merrill and K. R. Brown, “Progress in compensating pulse sequences for quantum computation,” in *Quantum Information and Computation for Chemistry*, pp. 241–294, John Wiley & Sons, Inc., 2014.
- [30] X. Wang, L. S. Bishop, J. P. Kestner, E. Barnes, K. Sun, and S. Das Sarma, “Composite pulses for robust universal control of singlet-triplet qubits,” *Nat. Commun.*, vol. 3, p. 997, Aug. 2012.
- [31] J. P. Kestner, X. Wang, L. S. Bishop, E. Barnes, and S. Das Sarma, “Noise-resistant control for a spin qubit array,” *Phys. Rev. Lett.*, vol. 110, p. 140502, Apr 2013.

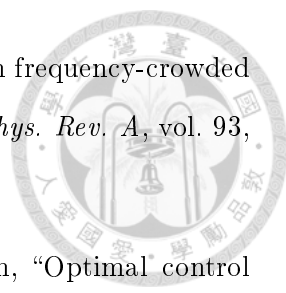
- 
- [32] X. Wang, L. S. Bishop, E. Barnes, J. P. Kestner, and S. Das Sarma, “Robust quantum gates for singlet-triplet spin qubits using composite pulses,” *Phys. Rev. A*, vol. 89, p. 022310, Feb 2014.
- [33] X. Wang, F. A. Calderon-Vargas, M. S. Rana, J. P. Kestner, E. Barnes, and S. Das Sarma, “Noise-compensating pulses for electrostatically controlled silicon spin qubits,” *Phys. Rev. B*, vol. 90, p. 155306, Oct 2014.
- [34] X. Rong, J. Geng, Z. Wang, Q. Zhang, C. Ju, F. Shi, C.-K. Duan, and J. Du, “Implementation of dynamically corrected gates on a single electron spin in diamond,” *Phys. Rev. Lett.*, vol. 112, p. 050503, Feb 2014.
- [35] X.-C. Yang and X. Wang, “Noise filtering of composite pulses for singlet-triplet qubits,” *Scientific Reports*, vol. 6, p. 28996, July 2016.
- [36] C. Chen, D. Dong, R. Long, I. R. Petersen, and H. A. Rabitz, “Sampling-based learning control of inhomogeneous quantum ensembles,” *Phys. Rev. A*, vol. 89, p. 023402, Feb 2014.
- [37] D. Dong, C. Chen, B. Qi, I. R. Petersen, and F. Nori, “Robust manipulation of superconducting qubits in the presence of fluctuations,” *Scientific Reports*, vol. 5, p. 7873, Jan. 2015.
- [38] D. Dong, C. Wu, C. Chen, B. Qi, I. R. Petersen, and F. Nori, “Learning robust pulses for generating universal quantum gates,” *Scientific Reports*, vol. 6, p. 36090, Oct. 2016.
- [39] J.-S. Li and N. Khaneja, “Control of inhomogeneous quantum ensembles,” *Phys. Rev. A*, vol. 73, p. 030302, Mar 2006.
- [40] J. H. Lee, E. Montano, I. H. Deutsch, and P. S. Jessen, “Robust site-resolvable quantum gates in an optical lattice via inhomogeneous control,” *Nat. Commun.*, vol. 4, p. 2027, June 2013.
- [41] E. Barnes, X. Wang, and S. Das Sarma, “Robust quantum control using smooth pulses and topological winding,” *Scientific Reports*, vol. 5, p. 12685, Aug. 2015.
- [42] D. Daems, A. Ruschhaupt, D. Sugny, and S. Guérin, “Robust quantum control by a single-shot shaped pulse,” *Phys. Rev. Lett.*, vol. 111, p. 050404, Jul 2013.

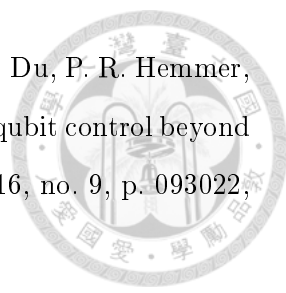
- 
- [43] R. L. Kosut, M. D. Grace, and C. Brif, “Robust control of quantum gates via sequential convex programming,” *Phys. Rev. A*, vol. 88, p. 052326, Nov 2013.
- [44] B. E. Anderson, H. Sosa-Martinez, C. A. Riofrío, I. H. Deutsch, and P. S. Jessen, “Accurate and robust unitary transformations of a high-dimensional quantum system,” *Phys. Rev. Lett.*, vol. 114, p. 240401, Jun 2015.
- [45] G. Gordon, G. Kurizki, and D. A. Lidar, “Optimal dynamical decoherence control of a qubit,” *Phys. Rev. Lett.*, vol. 101, p. 010403, Jul 2008.
- [46] A. Ruschhaupt, X. Chen, D. Alonso, and J. Muga, “Optimally robust shortcuts to population inversion in two-level quantum systems,” *New Journal of Physics*, vol. 14, no. 9, p. 093040, 2012.
- [47] X.-J. Lu, X. Chen, A. Ruschhaupt, D. Alonso, S. Guérin, and J. G. Muga, “Fast and robust population transfer in two-level quantum systems with dephasing noise and/or systematic frequency errors,” *Phys. Rev. A*, vol. 88, p. 033406, Sep 2013.
- [48] T. J. Green, J. Sastrawan, H. Uys, and M. J. Biercuk, “Arbitrary quantum control of qubits in the presence of universal noise,” *New Journal of Physics*, vol. 15, no. 9, p. 095004, 2013.
- [49] A. Soare, H. Ball, D. Hayes, J. Sastrawan, M. C. Jarratt, J. J. McLoughlin, X. Zhen, T. J. Green, and M. J. Biercuk, “Experimental noise filtering by quantum control,” *Nat. Phys.*, vol. 10, pp. 825–829, Nov. 2014.
- [50] H. Ball and M. J. Biercuk, “Walsh-synthesized noise filters for quantum logic,” *EPJ Quantum Technology*, vol. 2, p. 11, 2015.
- [51] G. A. Paz-Silva and L. Viola, “General transfer-function approach to noise filtering in open-loop quantum control,” *Phys. Rev. Lett.*, vol. 113, p. 250501, Dec 2014.
- [52] W. D. Oliver, “Quantum control: Engineering a revolution,” *Nat. Phys.*, vol. 10, pp. 794–795, Nov. 2014.
- [53] C. Kabytayev, T. J. Green, K. Khodjasteh, M. J. Biercuk, L. Viola, and K. R. Brown, “Robustness of composite pulses to time-dependent control noise,” *Phys. Rev. A*, vol. 90, p. 012316, Jul 2014.

- 
- [54] D. Loss and D. P. DiVincenzo, “Quantum computation with quantum dots,” *Phys. Rev. A*, vol. 57, pp. 120–126, Jan 1998.
- [55] J. R. Petta, A. C. Johnson, J. M. Taylor, E. A. Laird, A. Yacoby, M. D. Lukin, C. M. Marcus, M. P. Hanson, and A. C. Gossard, “Coherent manipulation of coupled electron spins in semiconductor quantum dots,” *Science*, vol. 309, p. 2180, Sept. 2005.
- [56] F. H. L. Koppens, C. Buizert, K. J. Tielrooij, I. T. Vink, K. C. Nowack, T. Meunier, L. P. Kouwenhoven, and L. M. K. Vandersypen, “Driven coherent oscillations of a single electron spin in a quantum dot,” *Nature*, vol. 442, pp. 766–771, Aug. 2006.
- [57] F. H. L. Koppens, K. C. Nowack, and L. M. K. Vandersypen, “Spin echo of a single electron spin in a quantum dot,” *Phys. Rev. Lett.*, vol. 100, p. 236802, Jun 2008.
- [58] D. J. Reilly, J. M. Taylor, J. R. Petta, C. M. Marcus, M. P. Hanson, and A. C. Gossard, “Suppressing spin qubit dephasing by nuclear state preparation,” *Science*, vol. 321, p. 817, Aug. 2008.
- [59] S. Foletti, H. Bluhm, D. Mahalu, V. Umansky, and A. Yacoby, “Universal quantum control of two-electron spin quantum bits using dynamic nuclear polarization,” *Nat. Phys.*, vol. 5, pp. 903–908, Dec. 2009.
- [60] H. Bluhm, S. Foletti, D. Mahalu, V. Umansky, and A. Yacoby, “Enhancing the coherence of a spin qubit by operating it as a feedback loop that controls its nuclear spin bath,” *Phys. Rev. Lett.*, vol. 105, p. 216803, Nov 2010.
- [61] C. Barthel, J. Medford, C. M. Marcus, M. P. Hanson, and A. C. Gossard, “Interlaced dynamical decoupling and coherent operation of a singlet-triplet qubit,” *Phys. Rev. Lett.*, vol. 105, p. 266808, Dec 2010.
- [62] H. Bluhm, S. Foletti, I. Neder, M. Rudner, D. Mahalu, V. Umansky, and A. Yacoby, “Dephasing time of GaAs electron-spin qubits coupled to a nuclear bath exceeding 200 μs ,” *Nat. Phys.*, vol. 7, pp. 109–113, Feb. 2011.
- [63] K. C. Nowack, M. Shafiei, M. Laforest, G. E. D. K. Prawiroatmodjo, L. R. Schreiber, C. Reichl, W. Wegscheider, and L. M. K. Vandersypen, “Single-shot correlations and two-qubit gate of solid-state spins,” *Science*, vol. 333, p. 1269, Sept. 2011.

- 
- [64] R. Brunner, Y.-S. Shin, T. Obata, M. Pioro-Ladrière, T. Kubo, K. Yoshida, T. Taniyama, Y. Tokura, and S. Tarucha, “Two-qubit gate of combined single-spin rotation and interdot spin exchange in a double quantum dot,” *Phys. Rev. Lett.*, vol. 107, p. 146801, Sep 2011.
- [65] M. D. Shulman, O. E. Dial, S. P. Harvey, H. Bluhm, V. Umansky, and A. Yacoby, “Demonstration of entanglement of electrostatically coupled singlet-triplet qubits,” *Science*, vol. 336, p. 202, Apr. 2012.
- [66] J. Medford, J. Beil, J. M. Taylor, S. D. Bartlett, A. C. Doherty, E. I. Rashba, D. P. DiVincenzo, H. Lu, A. C. Gossard, and C. M. Marcus, “Self-consistent measurement and state tomography of an exchange-only spin qubit,” *Nat. Nanotech.*, vol. 8, pp. 654–659, Sept. 2013.
- [67] J. M. Nichol, L. A. Orona, S. P. Harvey, S. Fallahi, G. C. Gardner, M. J. Manfra, and A. Yacoby, “High-fidelity entangling gate for double-quantum-dot spin qubits,” *npj Quantum Information*, vol. 3, no. 1, p. 3, 2017.
- [68] E. A. Chekhovich, M. N. Makhonin, A. I. Tartakovskii, A. Yacoby, H. Bluhm, K. C. Nowack, and L. M. K. Vandersypen, “Nuclear spin effects in semiconductor quantum dots,” *Nat. Mater.*, vol. 12, pp. 494–504, June 2013.
- [69] B. M. Maune, M. G. Borselli, B. Huang, T. D. Ladd, P. W. Deelman, K. S. Holabird, A. A. Kiselev, I. Alvarado-Rodriguez, R. S. Ross, A. E. Schmitz, M. Sokolich, C. A. Watson, M. F. Gyure, and A. T. Hunter, “Coherent singlet-triplet oscillations in a silicon-based double quantum dot,” *Nature*, vol. 481, pp. 344–347, Jan. 2012.
- [70] E. Kawakami, P. Scarlino, D. R. Ward, F. R. Braakman, D. E. Savage, M. G. Lagally, M. Friesen, S. N. Coppersmith, M. A. Eriksson, and L. M. K. Vandersypen, “Electrical control of a long-lived spin qubit in a Si/SiGe quantum dot,” *Nat. Nanotech.*, vol. 9, pp. 666–670, Sept. 2014.
- [71] M. Veldhorst, J. C. C. Hwang, C. H. Yang, A. W. Leenstra, B. de Ronde, J. P. Dehollain, J. T. Muhonen, F. E. Hudson, K. M. Itoh, A. Morello, and A. S. Dzurak, “An addressable quantum dot qubit with fault-tolerant control-fidelity,” *Nat. Nanotech.*, vol. 9, pp. 981–985, Dec. 2014.

- 
- [72] M. Veldhorst, C. H. Yang, J. C. C. Hwang, W. Huang, J. P. Dehollain, J. T. Muhonen, S. Simmons, A. Laucht, F. E. Hudson, K. M. Itoh, A. Morello, and A. S. Dzurak, “A two-qubit logic gate in silicon,” *Nature*, vol. 526, pp. 410–414, Oct. 2015.
- [73] K. Eng, T. D. Ladd, A. Smith, M. G. Borselli, A. A. Kiselev, B. H. Fong, K. S. Holabird, T. M. Hazard, B. Huang, P. W. Deelman, I. Milosavljevic, A. E. Schmitz, R. S. Ross, M. F. Gyure, and A. T. Hunter, “Isotopically enhanced triple-quantum-dot qubit,” *Science Advances*, vol. 1, no. 4, 2015.
- [74] K. Takeda, J. Kamioka, T. Otsuka, J. Yoneda, T. Nakajima, M. R. Delbecq, S. Amaha, G. Allison, T. Kodera, S. Oda, and S. Tarucha, “A fault-tolerant addressable spin qubit in a natural silicon quantum dot,” *Science Advances*, vol. 2, no. 8, 2016.
- [75] F. J. Dyson, “The radiation theories of tomonaga, schwinger, and feynman,” *Phys. Rev.*, vol. 75, pp. 486–502, Feb. 1949.
- [76] J. A. Nelder and R. Mead, “A simplex method for function minimization,” *The computer journal*, vol. 7, no. 4, pp. 308–313, 1965.
- [77] S. Finch and Y. Yt, *Ornstein-uhlenbeck process*. Citeseer, 2004.
- [78] A. V. Kuhlmann, J. Houel, A. Ludwig, L. Greuter, D. Reuter, A. D. Wieck, M. Poggio, and R. J. Warburton, “Charge noise and spin noise in a semiconductor quantum device,” *Nat. Phys.*, vol. 9, pp. 570–575, Sept. 2013.
- [79] Y. Li, N. Sinitsyn, D. L. Smith, D. Reuter, A. D. Wieck, D. R. Yakovlev, M. Bayer, and S. A. Crooker, “Intrinsic spin fluctuations reveal the dynamical response function of holes coupled to nuclear spin baths in (In, Ga)As quantum dots,” *Phys. Rev. Lett.*, vol. 108, p. 186603, May 2012.
- [80] R. A. Žak, B. Röthlisberger, S. Chesi, and D. Loss, “Quantum computing with electron spins in quantum dots,” *arXiv preprint arXiv:0906.4045*, 2009.
- [81] W. H. Lim, F. A. Zwanenburg, H. Huebl, M. Möttönen, K. W. Chan, A. Morello, and A. S. Dzurak, “Observation of the single-electron regime in a highly tunable silicon quantum dot,” *Appl. Phys. Lett.*, vol. 95, p. 242102, Dec. 2009.
- [82] T. Meunier, V. E. Calado, and L. M. K. Vandersypen, “Efficient controlled-phase gate for single-spin qubits in quantum dots,” *Phys. Rev. B*, vol. 83, p. 121403, Mar 2011.

- 
- [83] L. S. Theis, F. Motzoi, and F. K. Wilhelm, “Simultaneous gates in frequency-crowded multilevel systems using fast, robust, analytic control shapes,” *Phys. Rev. A*, vol. 93, p. 012324, Jan 2016.
- [84] F. Motzoi, J. M. Gambetta, S. T. Merkel, and F. K. Wilhelm, “Optimal control methods for rapidly time-varying hamiltonians,” *Phys. Rev. A*, vol. 84, p. 022307, Aug 2011.
- [85] D. J. Egger and F. K. Wilhelm, “Adaptive hybrid optimal quantum control for imprecisely characterized systems,” *Phys. Rev. Lett.*, vol. 112, p. 240503, Jun 2014.
- [86] J. Kelly, R. Barends, B. Campbell, Y. Chen, Z. Chen, B. Chiaro, A. Dunsworth, A. G. Fowler, I.-C. Hoi, E. Jeffrey, A. Megrant, J. Mutus, C. Neill, P. J. J. O’Malley, C. Quintana, P. Roushan, D. Sank, A. Vainsencher, J. Wenner, T. C. White, A. N. Cleland, and J. M. Martinis, “Optimal quantum control using randomized benchmarking,” *Phys. Rev. Lett.*, vol. 112, p. 240504, Jun 2014.
- [87] C. Ferrie and O. Moussa, “Robust and efficient in situ quantum control,” *Phys. Rev. A*, vol. 91, p. 052306, May 2015.
- [88] E. Magesan, J. M. Gambetta, and J. Emerson, “Scalable and robust randomized benchmarking of quantum processes,” *Phys. Rev. Lett.*, vol. 106, p. 180504, May 2011.
- [89] A. D. Córcoles, J. M. Gambetta, J. M. Chow, J. A. Smolin, M. Ware, J. Strand, B. L. T. Plourde, and M. Steffen, “Process verification of two-qubit quantum gates by randomized benchmarking,” *Phys. Rev. A*, vol. 87, p. 030301, Mar 2013.
- [90] S. Machnes, D. J. Tannor, F. K. Wilhelm, and E. Assémat, “Gradient optimization of analytic controls: the route to high accuracy quantum optimal control,” *arXiv preprint arXiv:1507.04261*, 2015.
- [91] Z. Chen, J. Kelly, C. Quintana, R. Barends, B. Campbell, Y. Chen, B. Chiaro, A. Dunsworth, A. G. Fowler, E. Lucero, E. Jeffrey, A. Megrant, J. Mutus, M. Neeley, C. Neill, P. J. J. O’Malley, P. Roushan, D. Sank, A. Vainsencher, J. Wenner, T. C. White, A. N. Korotkov, and J. M. Martinis, “Measuring and suppressing quantum state leakage in a superconducting qubit,” *Phys. Rev. Lett.*, vol. 116, p. 020501, Jan 2016.

- 
- [92] J. Scheuer, X. Kong, R. S. Said, J. Chen, A. Kurz, L. Marseglia, J. Du, P. R. Hemmer, S. Montangero, T. Calarco, B. Naydenov, and F. Jelezko, “Precise qubit control beyond the rotating wave approximation,” *New Journal of Physics*, vol. 16, no. 9, p. 093022, 2014.
- [93] F. Dolde, V. Bergholm, Y. Wang, I. Jakobi, B. Naydenov, S. Pezzagna, J. Meijer, F. Jelezko, P. Neumann, T. Schulte-Herbrüggen, J. Biamonte, and J. Wrachtrup, “High-fidelity spin entanglement using optimal control,” *Nat. Commun.*, vol. 5, p. 3371, Feb. 2014.
- [94] X. Rong, J. Geng, F. Shi, Y. Liu, K. Xu, W. Ma, F. Kong, Z. Jiang, Y. Wu, and J. Du, “Experimental fault-tolerant universal quantum gates with solid-state spins under ambient conditions,” vol. 6, p. 8748, Nov. 2015.